



**Aircraft and Rotorcraft Pilot Couplings – Tools and Techniques for
Alleviation and Detection**

ACPO-GA-2010-266073

**Deliverable No. D3.6
Pilot Modelling for Aero-Servo-Elastic A/RPC**

Contractual delivery date:
[12/2012]

Actual delivery date:
[02/2013]

Partner responsible for the Deliverable: TsAGI

Author(s):
Larisa Zaichik, Pavel Desyatnik, Yury Yashin (TsAGI)
Pierangelo Masarati, Giuseppe Quaranta, Vincenzo Muscarello (POLIMI)
Achim Ionita, Radu Stefan, Andreea-Irina Afloare (STRAERO)

Dissemination level		
PU	Public	X
PP	Restricted to other programme participants (including the Commission Services)	
RE	Restricted to a group specified by the consortium (including the Commission Services)	
CO	Confidential, only for members of the consortium (including the Commission Services)	

Document Information Table

Grant agreement no.	ACPO-GA-2010-266073
Project full title	ARISTOTEL – Aircraft and Rotorcraft Pilot Couplings – Tools and Techniques for Alleviation and Detection
Deliverable number	D3.6
Deliverable title	Pilot Modelling for Aero-Servo-Elastic A/RPC
Nature	R/P/D/O ¹ (R)
Dissemination level	PU/PP/RE/CO ² (PU)
Version	1.0
Work package number	WP3
Work package leader	STRAERO
Partner responsible for Deliverable	TsAGI
Reviewer(s)	Achim Ionita

The research leading to these results has received funding from the European Community's Seventh Framework Programme (FP7/2007-2013) under grant agreement n° 266073.

The author is solely responsible for its content, it does not represent the opinion of the European Community and the Community is not responsible for any use that might be made of data appearing therein.

¹ R=Report, P=Prototype, D=Demonstrator, O=Other

² PU=Public, PP=Restricted to other programme participants (including the Commission Services), RE=Restricted to a group specified by the consortium (including the Commission Services), CO=Confidential, only for members of the consortium (including the Commission Services)

Revision Table

Version	Date	Modified Page/Section	Author	Comments
1.0	29.11.2012		L.Zaichik, P.Desyatnik, Y.Yashin (TsAGI)	
1.1	7.02.2013		G.Quaranta, V.Muscarello, P.Masarati (POLIMI)	
1.2	8.02.2013		A.Ionita,R.Stefan, A.Afloare, (STRAERO)	
1.3	12.02.2013		L.Zaichik (TsAGI)	

Executive Summary

Task 3.2 deals with pilot modelling for aero-servo-elastic A/RPC. This report is to evaluate existing pilot models with respect to their suitability for application within A/RPC studies and to modify them or to develop new ones. Different approaches to pilot modelling are considered: with the help of transfer functions identified in the course of biodynamic experiments (Task 4.1), and multi-body approach requiring identification of biomechanical model of a pilot. The report gives detailed description of the pilot modelling techniques and their future application for aero-servo-elastic A/RPC analysis.

Table of Contents

Document Information Table	2
Revision Table.....	3
Executive Summary	3
1. Introduction.....	5
2. Rotorcraft Pilot Modelling by Transfer Function Approach.....	6
2.1. Biodynamical Pilot Modelling	6
2.1.1. Collective lever transfer functions.....	7
2.1.2. Lateral cyclic transfer functions.....	13
2.2. Active and Structural Pilot Model Analysis	22
2.2.1. Analysis of IAR 330 PUMA linearized configurations	22
2.2.2. Analysis of pilot models for prediction of unfavourable RPC	24
3. Aircraft Pilot Modelling by Transfer Function Approach	34
3.1. Database for the Model Development	35
3.2. Pilot Modelling to Take Into Account Inceptor Feel System Characteristics.....	44
4. Pilot Modelling by Multi-Body and Finite-Element Approach.....	50
4.1. Multibody Formulation	51
4.2. Multibody Model	51
4.3. Application: Vertical Maneuver	54
4.4. Equivalent Feedthrough	57
4.5. Direct Simulation	60
4.6. Collective Control Biodynamic Feedthrough	61
4.7. Collective Control Neuromuscular Admittance	62
4.8. BDFT and Neuromuscular Admittance Under Load	63
4.9. Use of Neuromuscular Admittance and BDFT.....	64
5. Results and Conclusion.....	65
6. Deviations.....	66
7. References	67
8. List of Abbreviations	71

1. Introduction

The report is devoted to pilot modeling performed within Task 3.2 (WP3), and is an important stage to develop criteria to predict aero-servo-elastic A/RPC. Pilot models are widely used to predict fixed- or rotary-wing aircraft handling qualities at early stages of the vehicle development, which makes control system development more effective and less time and cost-consuming. According to the thorough analysis of the present pilot models made in [1], there are many pilot model applicable only to specific research subjects. In this report the attention is paid to models used to describe pilot behavior under high-frequency accelerations, mainly in the 2-8 Hz region, caused by the aircraft aero-servo-elastic characteristics.

The biodynamic pilot-aircraft interaction caused by high-frequency accelerations manifests itself in involuntary body and limb displacements, which, in turn, can intensify the high-frequency oscillations and lead to worsening of handling qualities pilot ratings. The frequency range of the accelerations (oscillations) and their intensities depend on many factors: type of a vehicle (aircraft or rotocraft), control system, structural dynamics, manipulator type and its feel system characteristics. To predict the worst combination of the factors we need to know the biodynamic pilot models.

The pilot models developed in the report and suitable for the biodynamic interaction analysis can be divided into two main groups requiring different pilot modeling approaches:

- “Transfer functions” approach, as a traditional and convenient analytical method to predict pilot-aircraft stability and handling qualities
- “Multi-Body” approach requiring identification of the properties of biomechanical models of aircraft pilots.

The two modeling approaches present interdependences; as long as a multibody model is validated using experimental data, it can be used as a numerical source of data for transfer functions in configurations similar to experimental ones without the need to resort to further experiments. Furthermore, multibody models can be used to thoroughly explore parameter variability with respect to pilot's size, muscular activation, and various other parameters.

This work presents also an analysis of active pilot model and structural pilot model using the linearized aero-servo-elastic rotorcraft model developed by POLIMI. The pilot model evaluation has been made for different flight condition and mission tasks.

The modeling activities were shared by ARISTOTEL partners in accordance with the groups.

Being a key step in approaching the final goal of the project, pilot modeling is inseparably connected with other WP3 Tasks and other ARISTOTEL Work Packages. It sources from Task 4.1 (biodynamic tests) and meets both short-term and long-term perspectives of industrial requirements reported in [2,3]. The results give inputs to further analysis and prediction of aero-servo-elastic instabilities (Tasks 3.3, 3.4), development of prediction criteria, their validation (Tasks 4.2, 4.4) and design guidelines (Tasks 5.1, 5.2). Along with ARISTOTEL goals, the results of pilot modelling made a noticeable contribution to pilot model theory and will be published within ARISTOTEL Dissemination activity (WP6).

2. Rotorcraft Pilot Modelling by Transfer Function Approach

2.1. Biodynamical Pilot Modelling

Several Bio-dynamic Feed Through (BDFT) tests have been conducted in HELIFLIGHT full motion flight simulator at University of Liverpool (UoL) to identify helicopter pilots' biodynamic response while subject to vertical and lateral accelerations.

During these tests the flight simulator was used as a “shaker” for humans; the motion induced in the control inceptors by the oscillations imposed to the cockpit was measured, along with the motion induced in the limbs. Additional details on the experimental setup are described in [4]. The excitations consisted of coloured noise signals, band-pass filtered between 1 and 10 Hz, with zero mean and 0.004 g rms (99.96% amplitude within 0.01 g). Excitation has been applied in the vertical and lateral direction. During these tests, no specific flight task was required. The occupant was required to hold the control inceptors without compensating the stick vibration. There was a moderate requirement to keep the inceptor in the vicinity of the reference condition defined for that specific experiment, to avoid excessive drift. The results used to infer the transfer functions here are all referred to a condition of 50% stroke for the collective lever and centred position for the cyclic control.

Multiple subjects have been tested, based on availability, amongst the investigators. Among the subjects professional test pilots have been considered too.

To identify the BDFT the following signals have been considered:

- Acceleration measured on the motion base of the flight simulator as input;
- Acceleration measured on the pilot hand holding the stick, using the MTX sensors described in [4];
- Measurement of stick position recorded by the flight simulator.

During every test the pilot biodynamics has been considered as a Single Input Single Output (SISO) system, i.e vertical acceleration input and collective stick output or lateral acceleration input and lateral cyclic output. No attempt has been made to consider Single Input Multiple Output models, since no significant cross correlation was shown during the tests.

All measured data have been band-pass filtered using an optimal Butterworth filter with a pass band of [0.5 – 12] Hz in order to isolate the frequency band of interest of this work.

After the filtering phase, the coherence C_{xy} between the input u and the output y signals has been evaluated, (see [5])

$$C_{uy} = \frac{|G_{uy}|^2}{G_{uu} G_{yy}}$$

where G_{uy} is the cross-spectral density between u and y , and G_{uu} and G_{yy} the autospectral density of u and y respectively. The coherence function estimates the extent to which $y(t)$ may be predicted from $u(t)$ by an optimum linear least square and so is useful to check the linearity of the measured transfer function.

When the coherence level was considered satisfactory, the Blackman-Tukey algorithm was used to estimate the frequency response at the different frequencies [6]. Then, the a fitting of this frequency response points was made using a rational polynomial model of the class

$$y(s) = \frac{A(s)}{B(s)} u(s) + e(s)$$

where A and B are polynomials with an appropriate degree chosen by the user and e represents the measurement noise.

2.1.1. Collective lever transfer functions.

The goal in this case was to characterize the relationship between the vertical acceleration of the cockpit and the rotation of the collective bar. Figure 2.1 shows a pilot instrumented with MTX accelerometers on the limbs during a collective lever test.



Figure 2.1 Instrumented pilot in the HELIFLIGHT simulator for collective lever BDFT tests

<i>Human Subject</i>	<i>N°Tests Performed</i>	<i>Input Type</i>	<i>Input Amplitude</i>	<i>Reference Position</i>
#1 – M. Mataboni	2	Random	0.1g	50 %
#2 – G. Quaranta	4	Random	0.1g	50 %
#3 – A. Berryman	6	Random	0.1g	50 %
#4 – V. Muscarello	2	Random	0.1g	50 %
#5 – M. Molica	2	Random	0.1g	50 %
#6 – M. Mayer	2	Random	0.1g	50 %
#7 – S. Cheyne	1	Random	0.1g	50 %

Table 2.1 Collective lever test performed. The professional pilots are highlighted using bold fonts.

In general, for all these test a good coherence level has been found between the vertical left pilot hand acceleration and the vertical cockpit acceleration, while the coherence with the collective lever rotations has not been considered acceptable (too low). For this reason, only the frequency response between the accelerations have been computed.

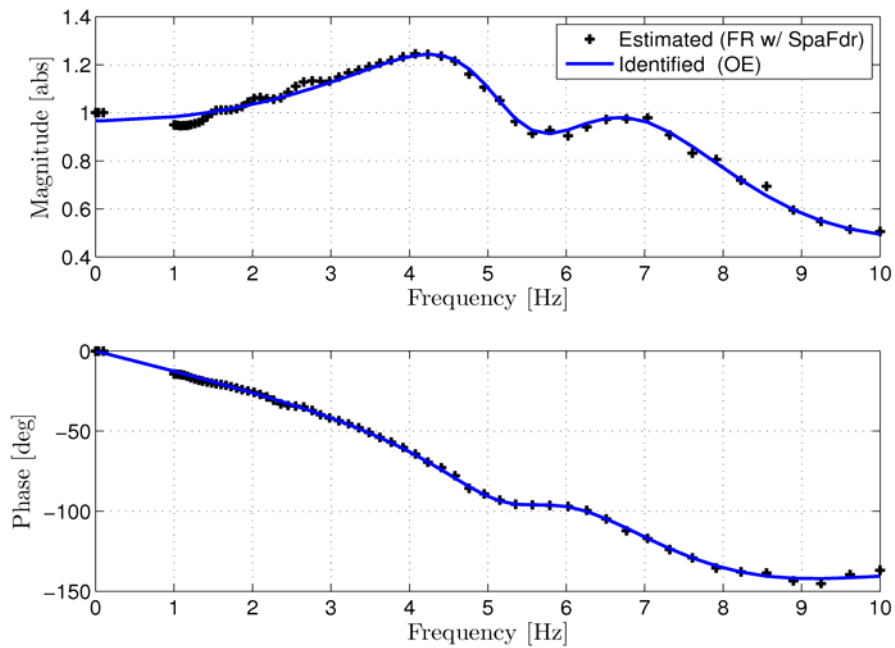


Figure 1.2 Collective lever test subject #2 test #2. Estimated frequency response (dots) and identified transfer function

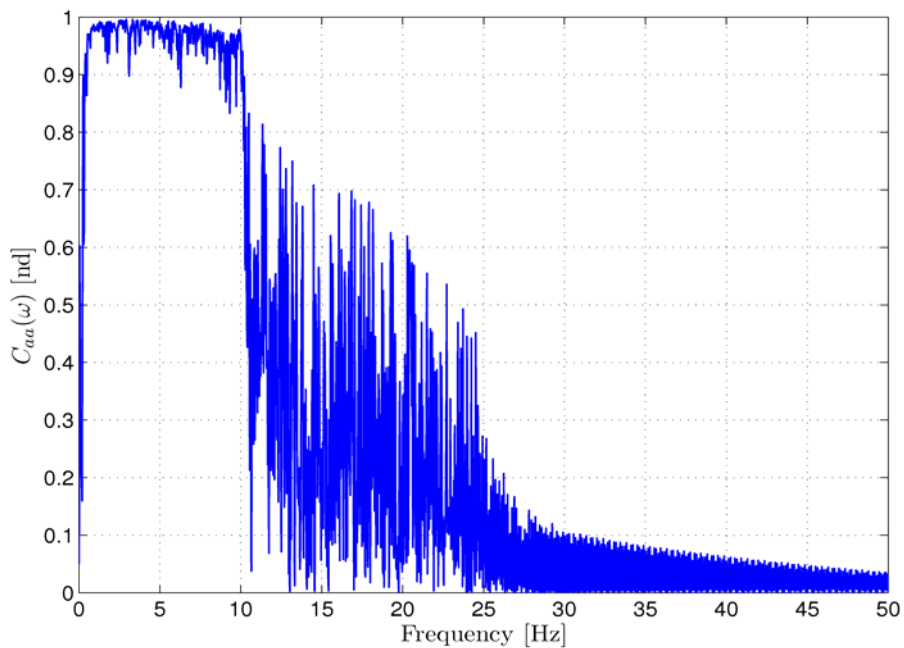


Figure 2.2 Collective lever test subject #2 test #2 coherence

Figure 2.2 shows that up to 10 Hz the coherence level is quite high. The estimated transfer function is shown in Figure 1 together with the fitted rational polynomial transfer function obtained by using a 6th order denominator and a 5th order numerator. The resulting poles are shown in Table 2.2.

Frequency	Damping
5.1177 [Hz]	21.162 [%]
6.6860 [Hz]	28.076 [%]
12.362 [Hz]	52.638 [%]

Table 2.2 Subject #2 test #2 list of poles frequency and damping

Other examples are shown in the following figures.

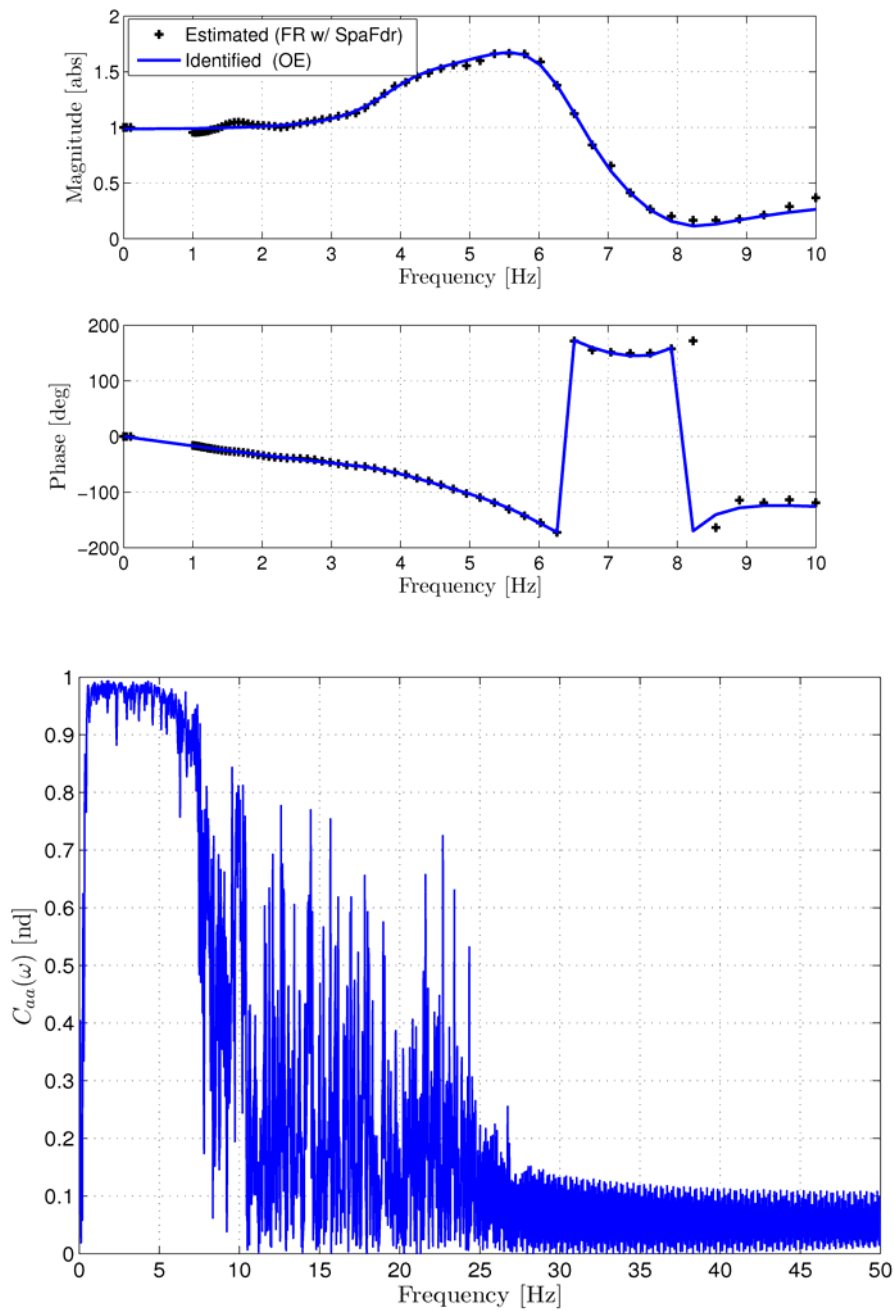


Figure 2.3 Collective lever test subject #3 test #4. Estimated frequency response (dots) and identified transfer function; coherence

Frequency*	Damping
3.9754 [Hz]	21.973 [%]
6.1662 [Hz]	15.562 [%]

Table 2.3 Subject #3 test #4 list of complex poles frequency and damping

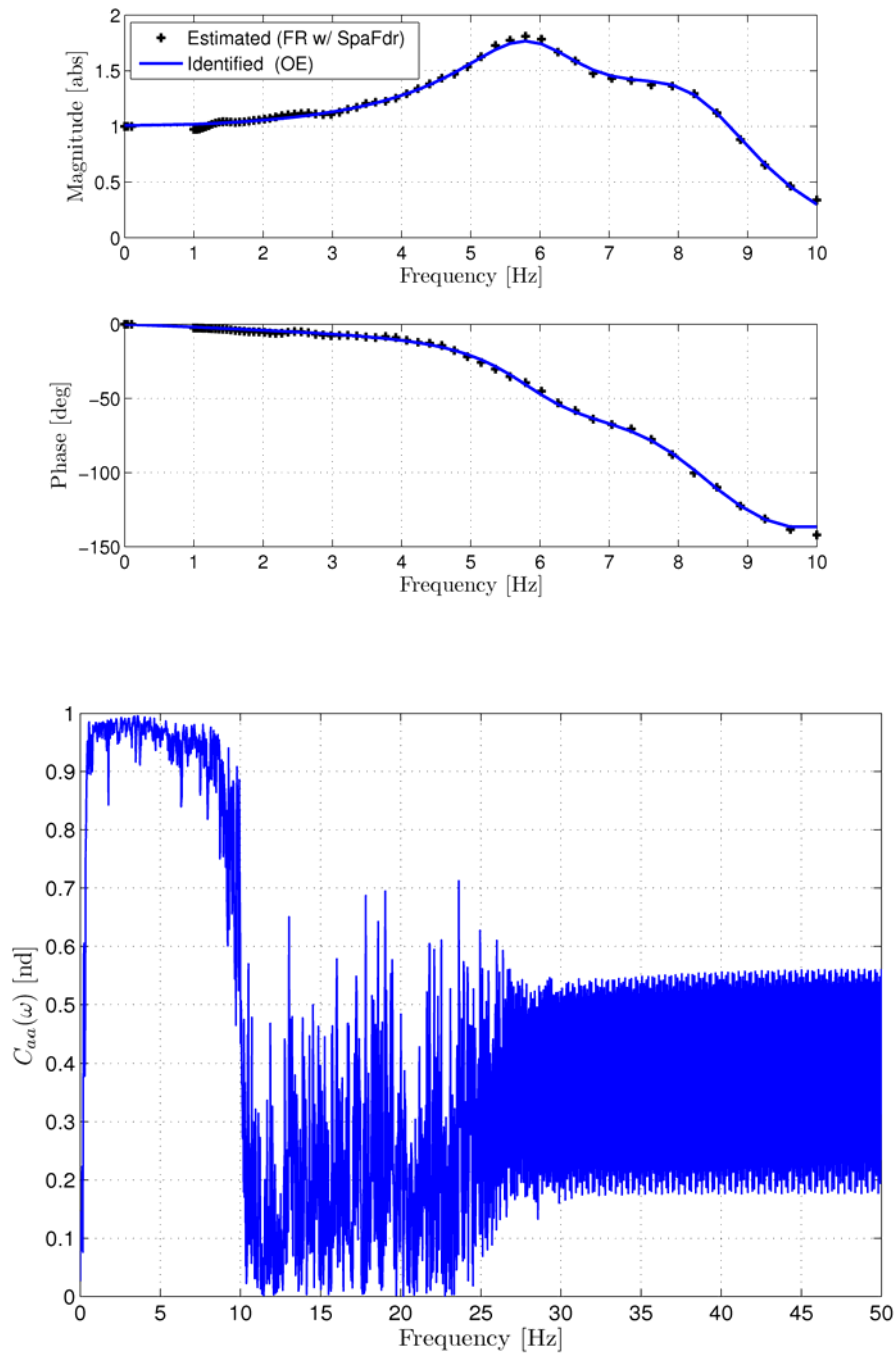


Figure 2.4 Collective lever test subject #6 test #2. Estimated frequency response (dots) and identified transfer function; coherence

Frequency*	Damping
5.8962 [Hz]	17.850 [%]
8.3867 [Hz]	14.280 [%]

Table 2.4 Subject #6 test #2 list of complex poles frequency and damping

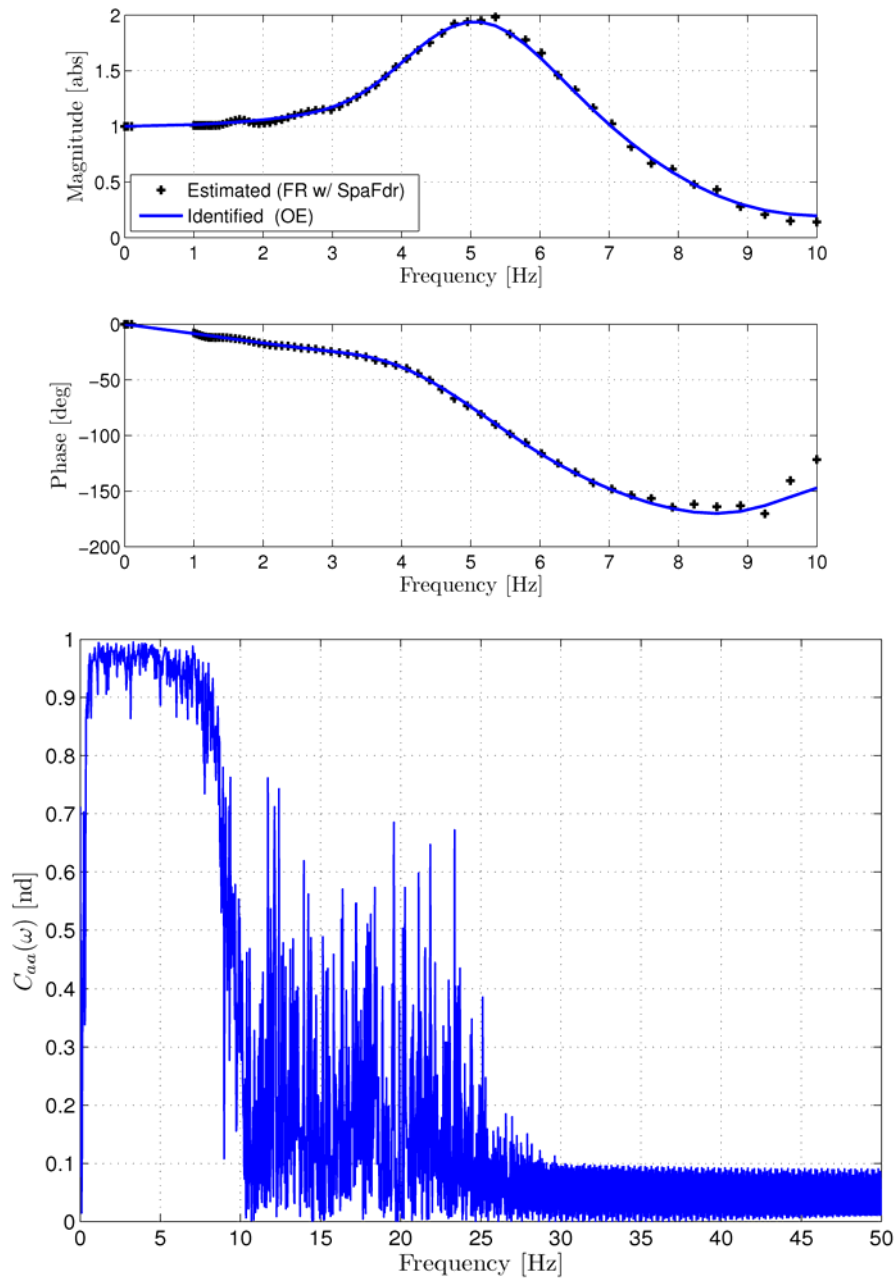


Figure 2.5 Collective lever test subject #7 test #1. Estimated frequency response (dots) and identified transfer function; coherence

Frequency	Damping
3.8330 [Hz]	36.020 [%]
5.3080 [Hz]	31.044 [%]
8.7075 [Hz]	31.552 [%]

Table 2.5 Subject #7 test #1 list of complex poles frequency and damping

Generally, it is possible to say that

- There are significantly damped biodynamic poles in the range between 3 and 10 Hz.
- Transfer functions are well approximated with fifth or sixth order polynomials.
- Pilot biodynamic responses are characterized by high level of variability. Transfer functions usually change significantly between different test pilots but also between different tests for the same pilot.
- The Identification procedures led to good correlation between predicted and measured outputs (over 70 % correlation).
- It does not seem to be possible to identify clear trends to separate the behavior of professional pilots from ‘novice’ pilots. At the same time there is not a clear relation with pilots’ biometric measures.

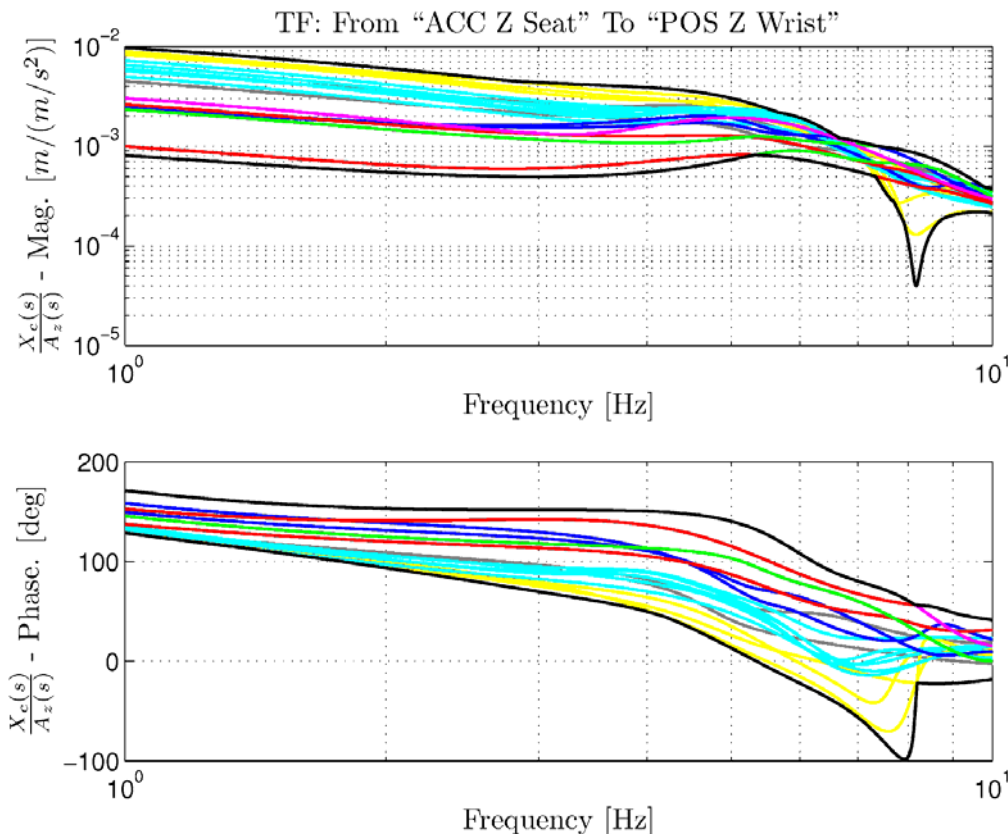


Figure 2.6 Collection of all identified transfer function frequency response for the collective lever

By collecting all identified transfer functions together it is possible to define a set of boundaries in the frequency domain in terms of max and min amplitude and max and min

phase at each frequency where the pilot transfer functions fall. This is shown in Figure 2.6 where all the identified transfer functions are shown together.

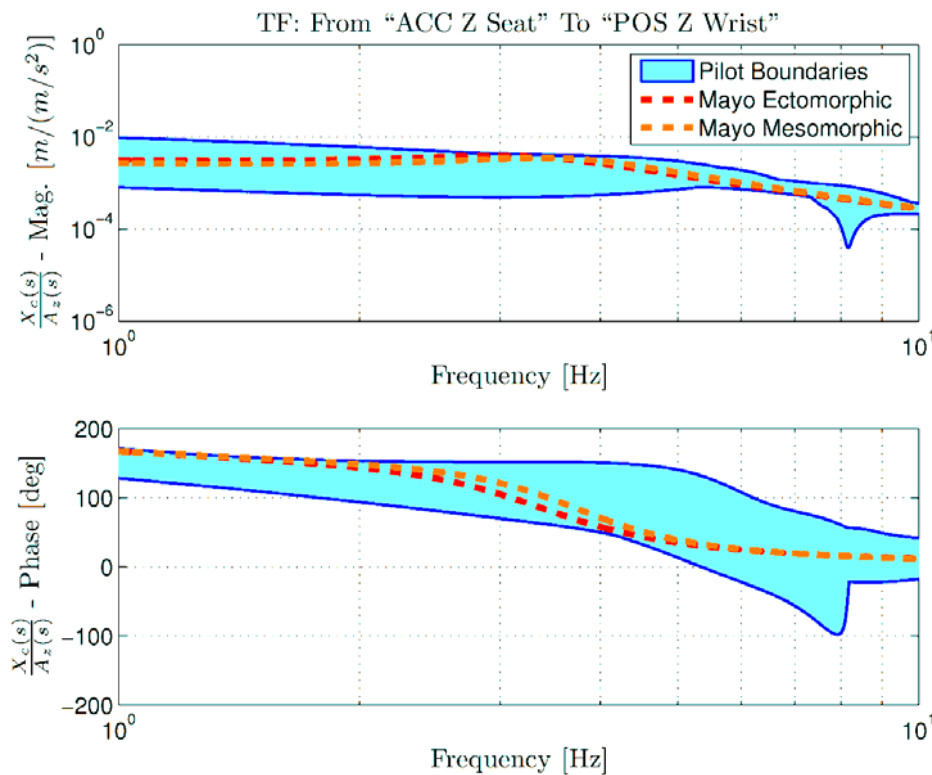


Figure 2.7 Comparison of identified pilot's BDFT boundaries with Mayo's transfer function

Those boundaries are compared with Mayo’s biodynamic transfer function [7] in Figure 2.7. Looking at the comparison it is possible to say that Mayo’s transfer functions are included in the identified boundaries but they are characterized by lower frequency poles than those of the transfer functions identified here.

2.1.2. Lateral cyclic transfer functions.

Pilot’s lateral cyclic transfer functions have been identified in order to characterize the relationship between the lateral acceleration of the pilot seat and the rotation of the lateral stick. The test matrix is reported in Table 2.6.

Human Being	N° Test Performed	Input Type	Input Amplitude	Reference Position
#1 – M. Mattaboni	1	Random	0.1g	0 %
#2 – G. Quaranta	1	Random	0.1g	0 %
#3 – A. Berryman	3	Random	0.1g	0 %
#4 – V. Muscarello	2	Random	0.1g	0 %
#5 – M. Molica	2	Random	0.1g	0 %
#6 – M. Mayer	2	Random	0.1g	0 %
#7 – S. Cheyne	2	Random	0.1g	0 %

Table 2.6 Lateral Cyclic stick test performed. The professional pilots are highlighted using bold fonts.

A good coherence level has been found between the lateral acceleration of the pilot seat, measured at the flight simulator motion base, and the lateral acceleration of the pilot wrist, measured by the MTX sensor. Furthermore, a good level of coherence has been found between the lateral acceleration of the motion base and the lateral stick rotation measured by flight simulator encoders. As a consequence, for each test, two transfer functions have been identified using two different output signals, while preserving the same input (acceleration at the pilot seat).

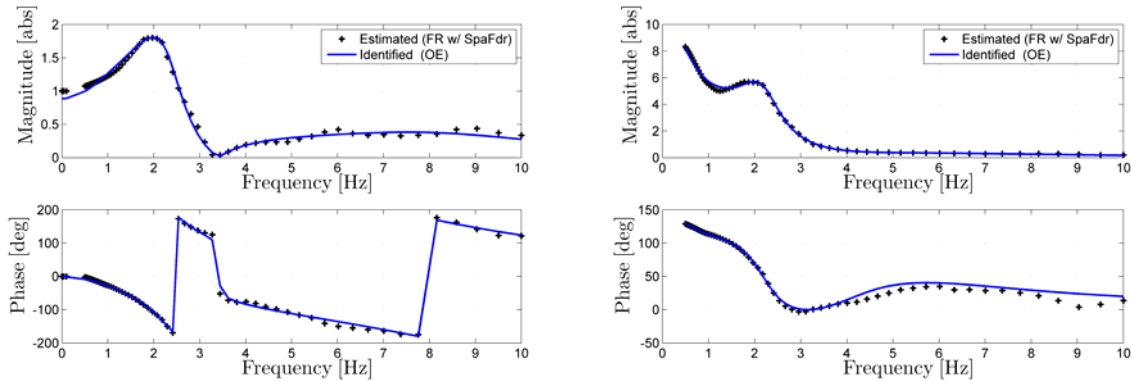


Figure 2.8 Lateral cyclic stick test subject #1, test #1. Estimated frequency response (dots) and identified transfer function. TF between the pilot seat acceleration and the pilot’s hand acceleration (left); TF between the pilot seat acceleration and the lateral cyclic rotation (right).

The pilot’s lateral dynamics has been identified using a rational polynomial transfer function of 6th order denominator and 4th order numerator using the pilot’s seat acceleration as input and the pilot’s wrist acceleration as output. At the same time, the transfer function between the pilot’s acceleration and the lateral cyclic stick rotation has been identified with a 5th order polynomial for the denominator and a 3rd order polynomial for the numerator.

Both TFs show a dominant pole at about 2.3 Hz. The coherence levels are shown in the figure below.

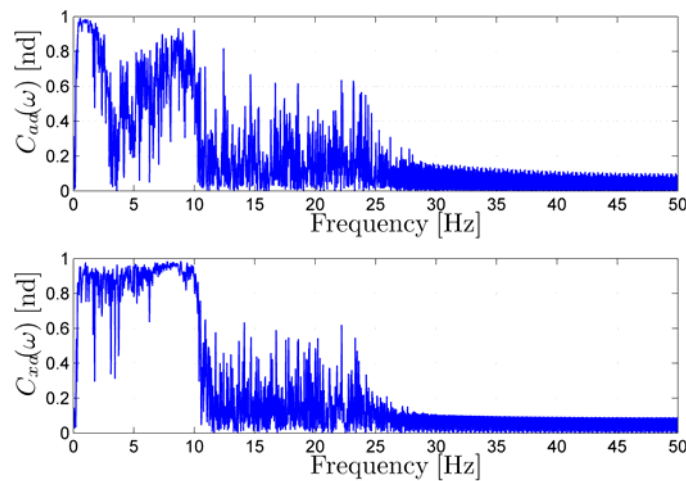


Figure 2.9 Lateral cyclic stick test subject #1, test #1. Coherence between the pilot seat acceleration and the pilot’s hand acceleration (top); coherence between the pilot seat acceleration and the lateral cyclic rotation (bottom).

Figure 2.9 shows that up to 10 Hz, the coherence is quite high when considering the lateral cyclic rotation as output measure (bottom). Some discrepancies are shown in the top figure when considering the lateral acceleration of the pilot wrist as output. However, the comparison between the identified transfer functions shows similar results in the frequency range of 1-10 Hz both in terms of magnitude and phase.

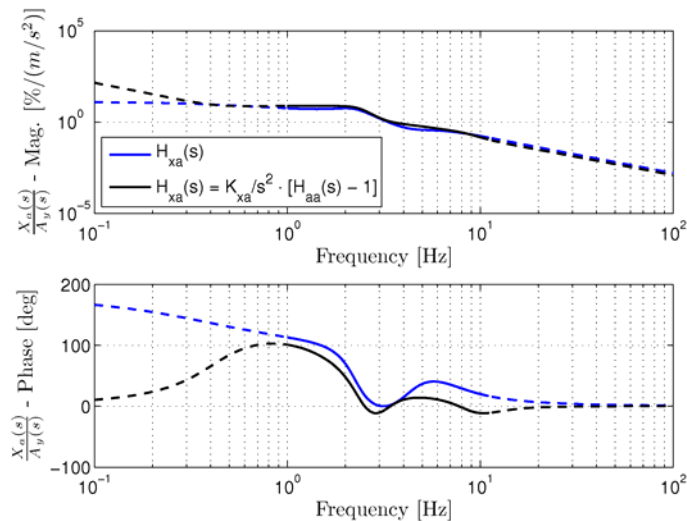


Figure 2.10 Lateral cyclic stick test subject #1, test #1. TF comparison.

The transfer functions have been compared considering the lateral rotation of the cyclic stick as output. The TF between the acceleration of the pilot seat and the acceleration of the pilot wrist has been post-processed in order to obtain the rotation of the stick, through the introduction of a double integrator and the control gearing ratio K_{xa} .

Other examples are shown in the following figures.

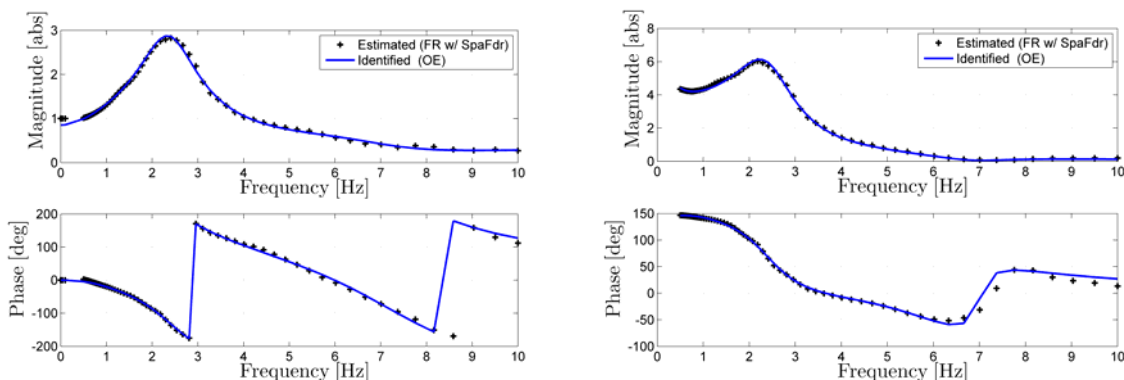


Figure 2.11 Lateral cyclic stick test subject #3, test #3. Estimated frequency response (dots) and identified transfer function. TF between the pilot seat acceleration and the pilot's hand acceleration (left); TF between the pilot seat acceleration and the lateral cyclic rotation (right).

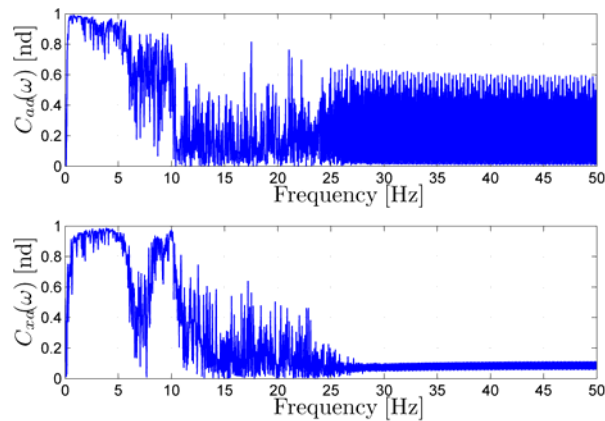


Figure 2.12 Lateral cyclic stick test subject #3, test #3. Coherence between the pilot seat acceleration and the pilot's hand acceleration (top); coherence between the pilot seat acceleration and the lateral cyclic rotation (bottom).

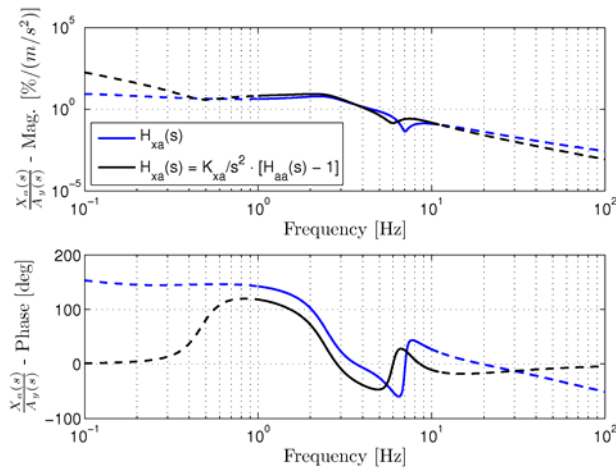


Figure 2.13 Lateral cyclic stick test subject #3, test #3. TF comparison.

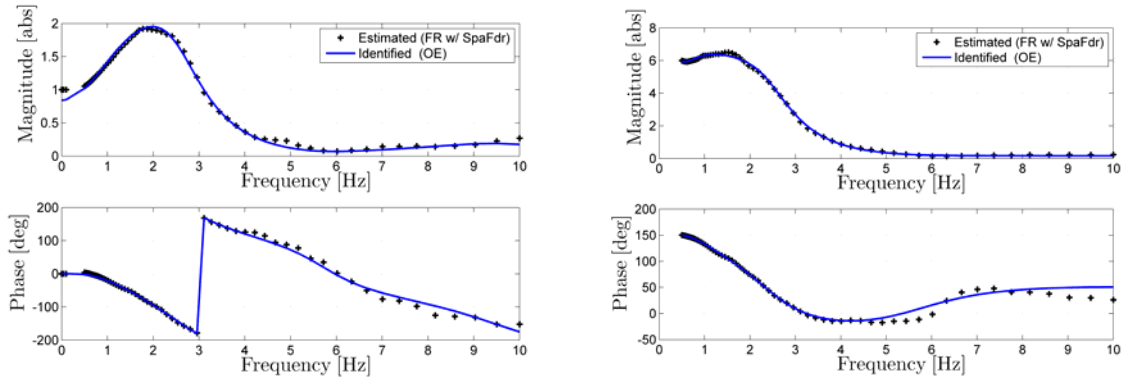


Figure 2.14 Lateral cyclic stick test subject #5, test #1. Estimated frequency response (dots) and identified transfer function. TF between the pilot seat acceleration and the pilot's hand acceleration (left); TF between the pilot seat acceleration and the lateral cyclic rotation (right).

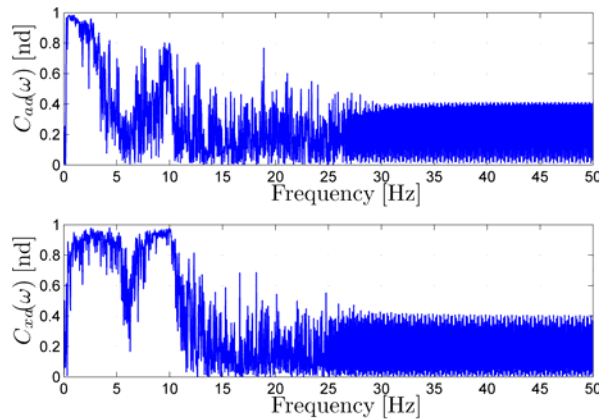


Figure 2.15 Lateral cyclic stick test subject #5, test #1. Coherence between the pilot seat acceleration and the pilot's hand acceleration (top); coherence between the pilot seat acceleration and the lateral cyclic rotation (bottom).

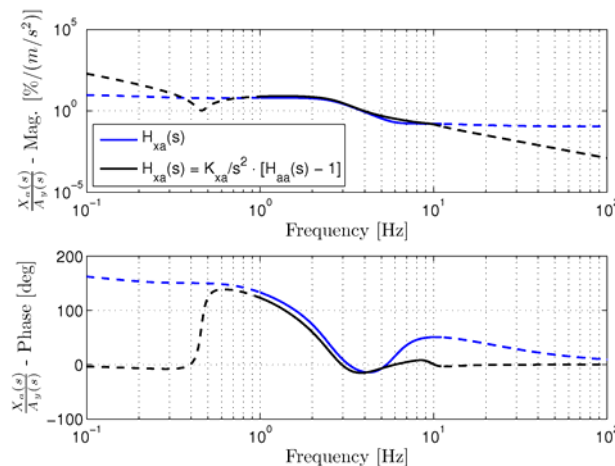


Figure 2.16 Lateral cyclic stick test subject #5, test #1. TF comparison.

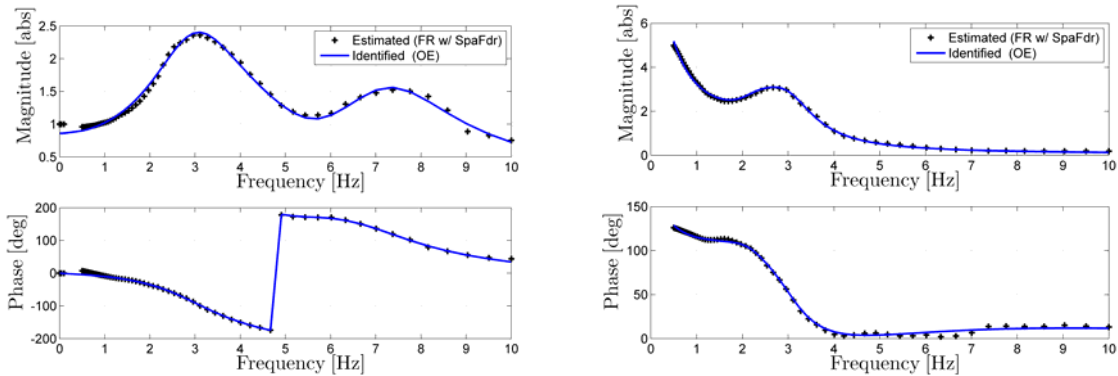


Figure 2.17 Lateral cyclic stick test subject #7, test #2. Estimated frequency response (dots) and identified transfer function. TF between the pilot seat acceleration and the pilot's hand acceleration (left); TF between the pilot seat acceleration and the lateral cyclic rotation (right).

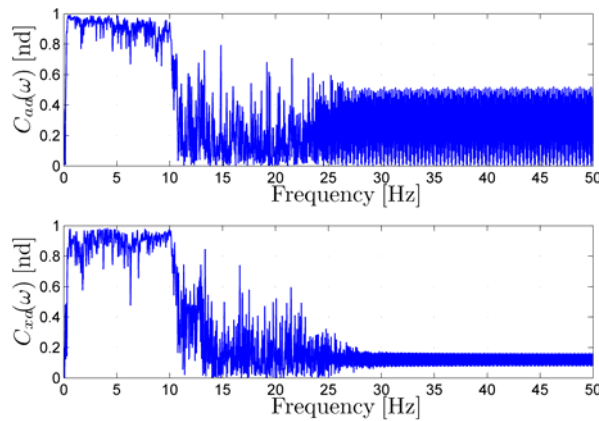


Figure 2.18 Lateral cyclic stick test subject #7, test #2. Coherence between the pilot seat acceleration and the pilot's hand acceleration (top); coherence between the pilot seat acceleration and the lateral cyclic rotation (bottom).

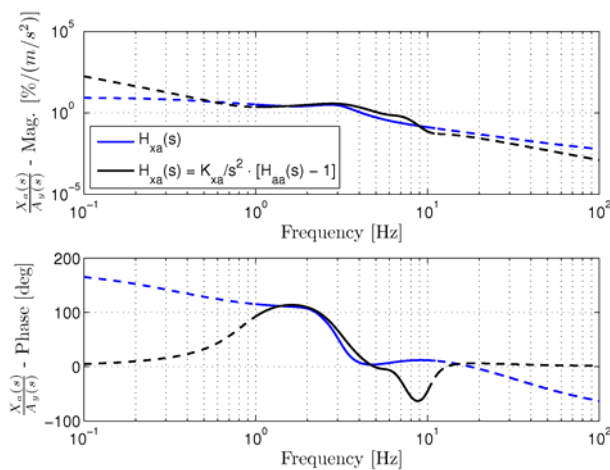


Figure 2.19 Lateral cyclic stick test subject #7, test #2. TF comparison.

Generally, it is possible to state that:

- Transfer functions depend significantly on the stiffness, damping and the mass of the control inceptors; By performing several measures on the cyclic stick of the flight simulator, it has been deduced that the stick equivalent linear stiffness is $k = 175$ N/m, the equivalent mass is $m = 0.31612$ kg and the equivalent damping is $c = 9.0$ N s/m.
- In general there is one clear pair of dominant poles between 2-3 Hz;
- Dominant poles are less damped than in the case of vertical transfer functions.

By collecting all the identified transfer functions together it is possible to define a set of boundaries in the frequency domain in terms of maximum and min amplitude/phase at each frequency where the pilot transfer functions fall. This is shown in Figure 2.20, considering the TF between the lateral acceleration at the pilot seat and the lateral position at the pilot's wrist (by means of double integration of the pilot's wrist acceleration) and in Figure 2.21, considering the TF between the lateral acceleration at the pilot seat and the lateral rotation of the control stick.

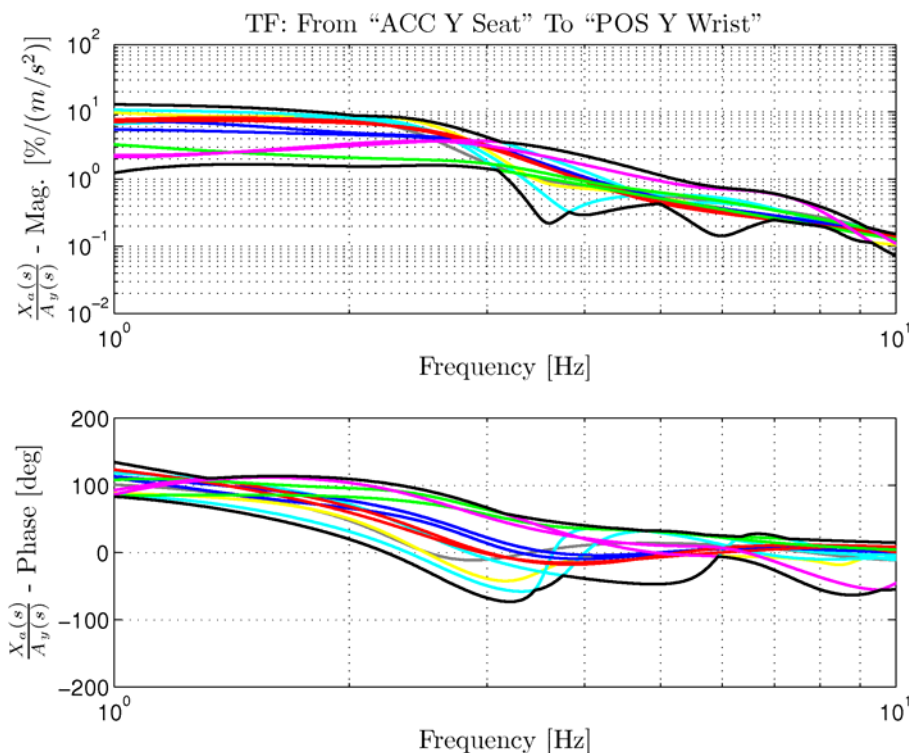


Figure 2.20 Collection of all identified transfer function frequency response for the lateral cyclic stick (Acc Y Seat → Pos Y Wrist)

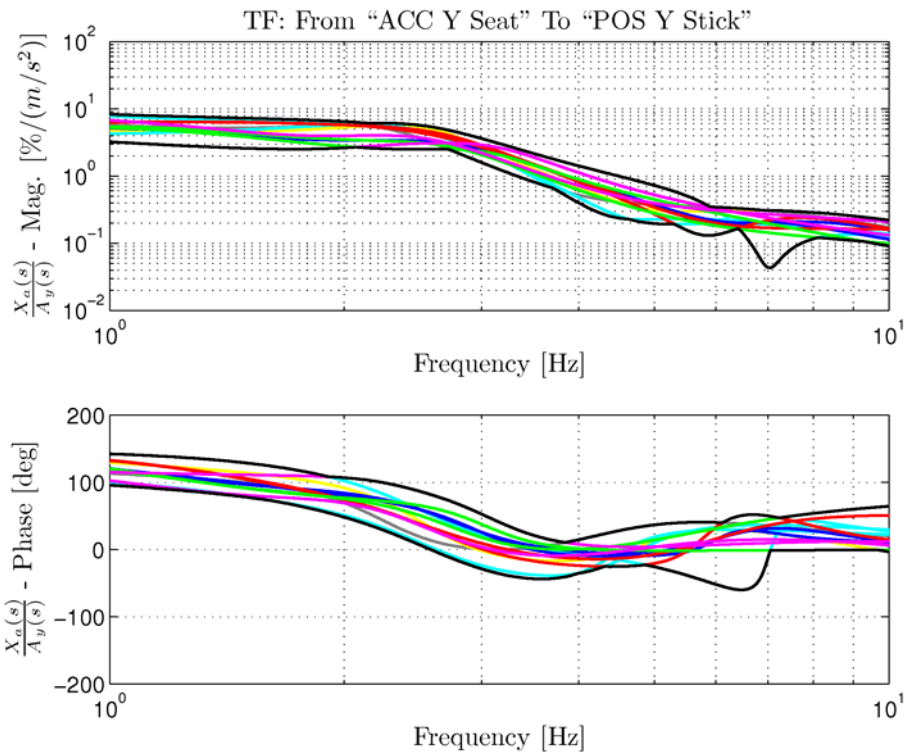


Figure 2.21 Collection of all identified transfer function frequency response for the lateral cyclic stick (Acc Y Seat → Pos Y Stick)

TF boundaries have been compared with the lateral/stick pilot transfer function identified by Parham et al.[PAR] in Figure 2.22 and Figure 2.23.

$$H_{Par}^*(s) = \frac{9.4487e+03 \cdot s - 2.8526e+05}{s^3 + 1.2641e+03 \cdot s^2 + 9.7102e+03 \cdot s + 3.8554e+05}$$

A fitting of Parham’s TF is reported above in [in/g]. Figures have been generated by considering the control gearing ratio of HELIFLIGHT and the input measure in [m/s²]. The transfer function identified from data presented by Parham is almost inside the identified boundaries and has dominant pole (at 2.7 Hz) close to the dominant pole of the transfer functions identified at UoL.

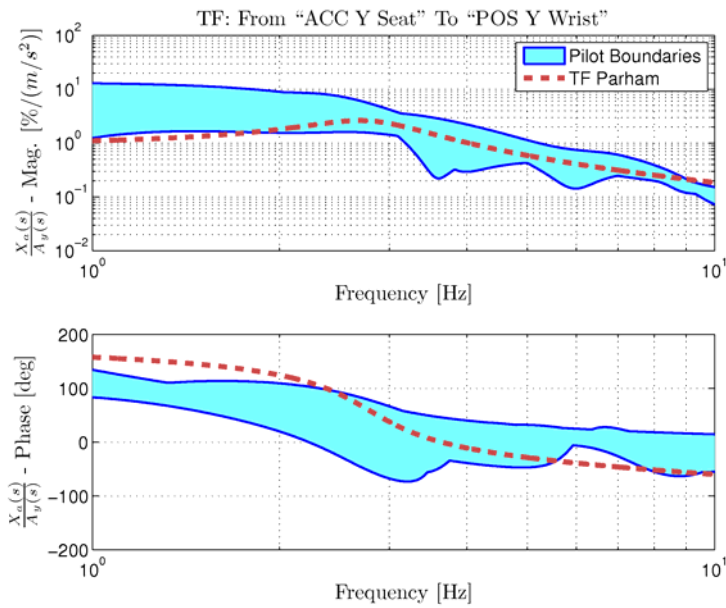


Figure 2.22 Comparison of identified pilot's BDFT boundaries with Parham's transfer function (Acc Y Seat → Pos Y Wrist)

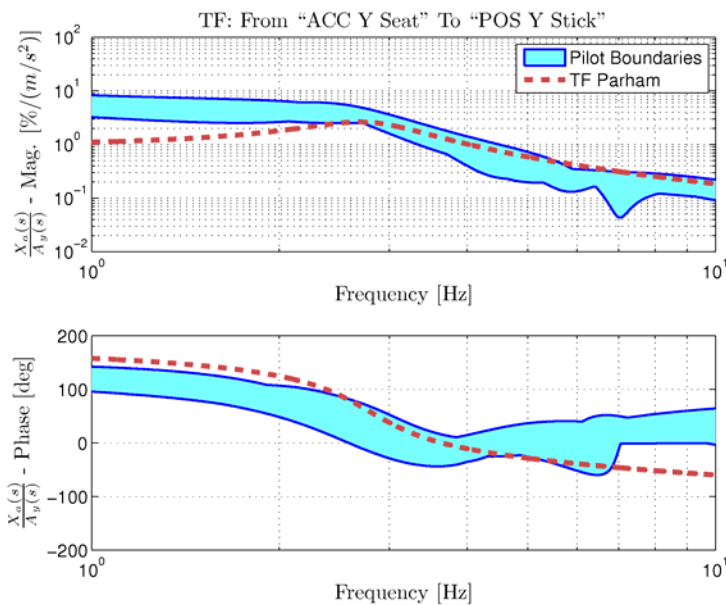


Figure 2.23 Comparison of identified pilot's BDFT boundaries with Parham's transfer function (Acc Y Seat → Pos Y Stick)

2.2. Active and Structural Pilot Model Analysis

The flying qualities prediction techniques based on piloting models have been proposed over the past six decades. The analytical criteria for the specification of handling qualities have two forms: the first are the open-loop criteria such as limits on measured responses or on modes and the second are the closed-loop criteria assuming a pilot feedback structure which are dependent on the accuracy and adequacy of the pilot model forms. These models have been developed extensively to describe, understand and predict pilot behaviour in many classes of vehicles including aircraft and rotorcraft. The pilot model can be characterised through four basic categories of mathematical models: isomorphic, algorithmic, behaviour-based and qualitative [1, 34, 35].

The isomorphic models describe those which explicitly construct the dynamics of the human sensors and control effectors systems. Here two representative examples are so-called crossover and structural models of the human pilot (McRuer, Hess) followed by other examples such biophysical models (von Passen) and biodynamical models (Jex).

The advantage of the crossover model is that it is very simple; also it makes certainly well enough for engineering applications. The disadvantage is that it is only valid around crossover frequency and only valid for compensatory tracking task.

The structural pilot model gives a more realistic representation of the signal processing structure in the pilot. Its advantage is that for single axis compensatory tracking, the model correlates well with test data. The disadvantage is that like with crossover model, it is valid for compensatory tracking task and only more over variable for predicting pilot ratings is dependent on the unit of pilot output.

The two major modelling techniques: the crossover model and structural model have been proposed to describe MIMO conditions. In order to apply the crossover or structural models some assumptions are needed regarding to limit numbers of the transfer functions associated with the sequentially loop closures. Predominantly, pilot models have been originally developed with SISO tasks.

2.2.1. Analysis of IAR 330 PUMA linearized configurations

This work uses the aero-servo-elastic (ASE) models built by POLIMI through MASST simulation tool [36]. Their dynamics include 6 rigid body modes, 8 structural modes of fuselage, 14 aero-elastic modes for main rotor with additional axial dynamic inflow state. The rotorcraft dynamics is completed by 4 servo-actuators on main controls and 4 controllers' dynamics to improve stability performances. The control for rotorcraft model consist of main rotor collective pitch, longitudinal cyclic pitch, lateral cyclic pitch and tail rotor collective pitch. Additional controls are considered the external forces on CG location along their axes. Both hover and 80 kts speed forward flight condition at sea level have been considered.

For the PUMA model, the complete linearization has carried on the developed rigid and elastic models, where the number of states depends on SCAS (ON/OFF) contribution.

The first step was to obtain a reduced order model, especially designed to include the servo-elastic contribution of rotor and fuselage dynamics through a simulation model of realistic complexity. The need for low order models is motivated by computational reasons for high complex vehicle where the model is described by a large number of first order differential equations. The effect of helicopter dynamic of constraining degree of freedom can be modelled in different ways.

The first is to set to zero or to some prescribed value, the portions of model corresponding to the constrained degree of freedom. This is the simplest technique, but it tends to be inaccurate, especially for extreme couplings between longitudinal and lateral modes like rotorcraft with articulated rotors [37].

Another possibility is to use the model reduction techniques, like Balanced Stochastic Truncation or algorithms based on singular Hankel value decompositions, which are implemented in the Robust Toolbox of Matlab.

Analysing the A matrix of the state space models for simulator we observe that appear a large domain on frequency scale. This makes it a challenge to develop a rigid body reduced model.

A widely used technique is the quasi-static reduction of the constrained degree of freedom. This is acceptable for us because it is a clear frequency separation between the dynamics to be left free and the dynamics to be constrained [38,39] (Figure 2.25). The objective of the reduced-order realization is that the states of reduced model approximate the behaviour of the states of ASE model and the outputs of the reduced order model match the output response of the initial system.

Consider the system in linearized form and partition the state vector into partition x_1 to be retained and a partition x_2 to be removed:

$$\begin{Bmatrix} \dot{x}_1 \\ \dot{x}_2 \end{Bmatrix} = \begin{bmatrix} A_{11} & A_{12} \\ A_{21} & A_{22} \end{bmatrix} \begin{Bmatrix} x_1 \\ x_2 \end{Bmatrix} + \begin{bmatrix} B_1 \\ B_2 \end{bmatrix} u \quad (2.1)$$

If it can be assumed that the states x_2 are infinitely fast, so that one can write $\dot{x}_2 = 0$, then the lower partition of Eq.(2.1) can be solved for x_2 and solution substituted back into upper partition. This results in the reduced order model:

$$\dot{x}_1 = \tilde{A}x_1 + \tilde{B}u \quad (2.2)$$

with

$$\tilde{A} = A_{11} - A_{12}A_{22}^{-1}A_{21} \quad (2.3)$$

$$\tilde{B} = B_1 - A_{12}A_{22}^{-1}B_2 \quad (2.4)$$

The measure of “goodness” of reduced order model may be some error criteria in the frequency and/or time domain and is highly dependent on the purpose for reduced order model and particular application.

For this work together with full ASE model (74 states) only one reduced order model was selected: low order model M42(10 Hz – 42 states). From results displayed in Figure 2.25 appear a distinct separation between the frequency at 10 Hz and the rest. We propose that the candidate low order M42 model for pilot vehicle coupling analysis.

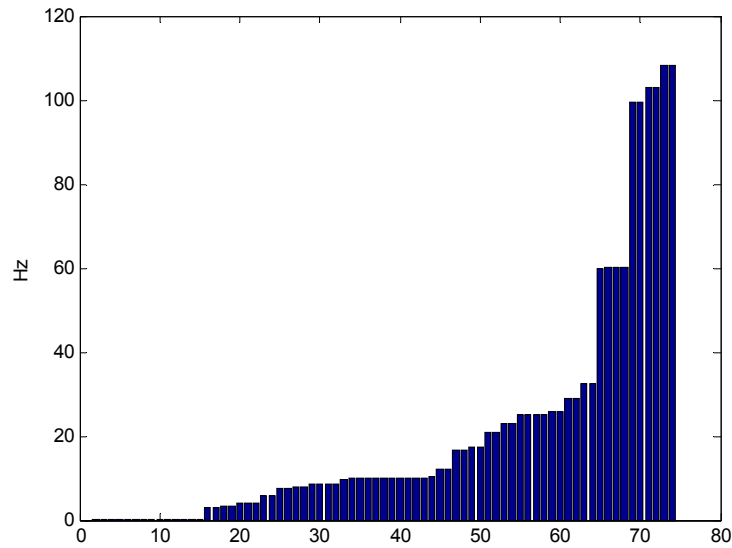


Figure 2.25 Frequency map for ASE model at sea level and V=80 kts

2.2.2. Analysis of pilot models for prediction of unfavourable RPC

2.2.2.1 Active pilot models

The application of the crossover model in area of manual control proposed by MacRuer [40,41,42,43] on IAR330 PUMA make the subject of this part applied to active pilot model. It states that human operator adjusts their control activity to drive the pilot-vehicle dynamics towards the following transfer function:

$$Y_p(s)Y_c(s) = \omega_c \frac{e^{-\tau_e s}}{s} \quad (2.5)$$

where $Y_p(s)$, $Y_c(s)$, ω_c and τ_e represent the pilot transfer function, vehicle transfer function, crossover frequency and effective time delay respectively. The controlled element $Y_c(s)$ is specified in terms of rotorcraft mathematical model.

One objective is to define an appropriate pilot strategy, $Y_p(s)$.

In applying the primary rule of thumb it is suitable to have an established value for the desired crossover frequency.

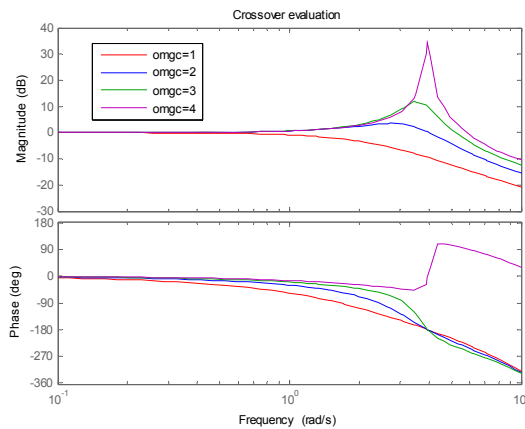


Figure 2.26 Closed-loop characteristics of $Y_p(s)Y_c(s)$ system with $\tau_e = 0.4s$ [44]

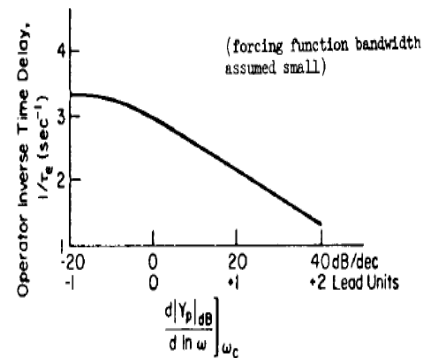


Fig.2.27 Variation of Crossover Model Dynamic Stimulus-Response

Latency with Degree of Pilot Lead Equalization [40]

The Figure 2.26 shows the amplitude portions of the Bode diagram for the closed loop pilot-vehicle system [44] for the specific task when the $Y_p(s)Y_c(s)$ of equation (2.5) is used $\tau_e = 0.4$ sec and $\omega_c = 1-4$ rad/sec. Observe that with $\omega_c = 2$ rad/sec the system is slightly underdamped but for frequency below $\omega_c = 2$ rad/sec. However, closed loop response to control attitude change by example would be comparatively sluggish. In this case the common crossover frequency ω_c for the open-loop pilot vehicle was chosen to be 2 rad/sec for longitudinal channel and 2.5 rad/sec for the lateral one. The value of the crossover frequency is intended to be a measure of desired performance levels and should be related to the nature of the task. It also ensures that the closed loop pilot-vehicle system is stable for all cases.

In addition, the crossover model also calls for an effective time delay which normally depends on controlled model transfer function [45,46]. Based on the sketch from Figure 2.27 we can estimate τ_e in respect with slope of $Y_p(s)$ versus ω_c at crossover frequency. Further simplified models of the vehicle can be applied to approximate different variety of tasks $Y_c(s)$, to obtain together $Y_p(s)$ transfer function a behaviour in respect with (2.5).

The simplified models for rotorcraft dynamics has be obtained from POLIMI IAR330 PUMA rigid body SCASOFF with additional stability augmentation.

The transfer functions for different tasks that pitch up, roll step, side step or vertical manoeuvre have the form:

$$TF(s) = K \frac{(s + a_1)(s + a_2)}{(s^2 + b_1s + b_2)(s^2 + b_3s + b_4)} \quad (2.6)$$

or

$$TF(s) = \frac{K}{s(s + a)} \quad (2.7)$$

The transfer function for active pilot model can be estimated as [15]:

$$Y_p(s) = Y_c(s)^{-1} \frac{\omega_c}{s} e^{-\tau_e s} \quad (2.8)$$

The transfer functions of active pilot-vehicle open loop model for different tasks are presented in Figures 2.28 a and 2.28b considering ASE and low order M42 models.

Figure 2.29 (band width-phase delay criterion [48]) and Figure 2.30 show influence of the effective time delay τ_e when term $e^{-\tau_e s}$ is approximated with a rational transfer function using a first and second order Pade terms.

2.2.2.2. Structural pilot model

The human pilot model so-called “structural pilot model” developed by R. Hess (derived from a theory introduced by Smith) is capable of capturing the prominent features of human pilot dynamics characteristics for a large class of aerial vehicles and tasks [49,50,51,52,53]. Figure 2.31 presents the structural pilot model which consists from two parts: the central nervous system and the neuromuscular system. In analysis to follow the individual blocks are presented as follow:

$$Y_{P_n} = \frac{\omega_n^2}{s^2 + 2\xi\omega_n s + \omega_n^2}; \quad Y_f = \frac{K_1 s}{s + 1/T_1}; \quad Y = \frac{K_2}{(\xi + 1/T_2)^{-1}}; \quad (2.9)$$

where $Y_c(s)$ and $Y_p(s)$ are transfer function of rotorcraft and pilot.

The following procedure is adopted to select the appropriate values of different parameters used in above transfer function and to evaluate the measure of the workload and the handling qualities sensitivity function (HQSF)[54]:

- a specified vehicle and flight tasks to be simulated are established,
- the mathematical model for the rotorcraft is obtained,
- a crossover frequency ω_c is selected as a measure of the specified performance level characterizing the task,

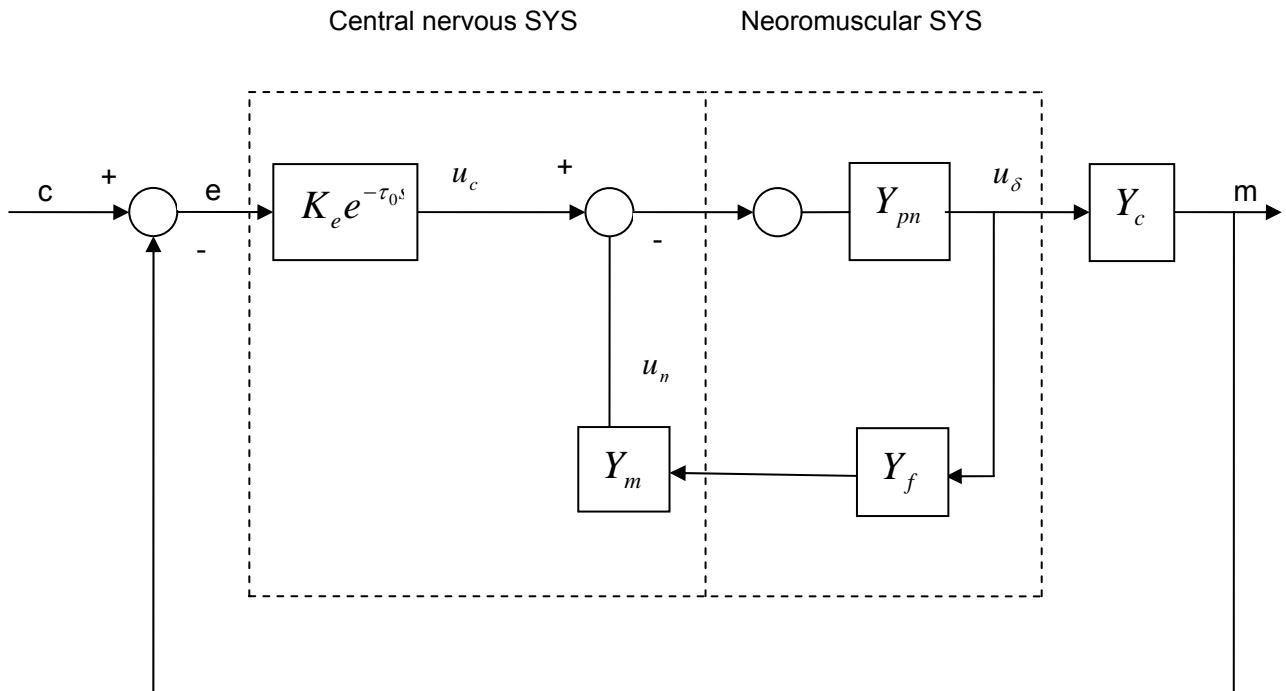


Figure 2.31. Structural Pilot Model

- the parameter 'k' in the structural model is selected based on the vehicle transfer function and the specified crossover frequency. The value of 'k' will depend upon whether gain (k=1), lead (k=2), or lag (k=0) compensation is required,
- the nominal parameter values for structural pilot model are selected from table 1 depending on 'k' value,
- the value of parameter T_2 is chosen to ensure 1/s like open – loop pilot vehicle characteristics around ω_c ,
- the relation

$$K_e = \frac{1}{|Y_p(j\omega_c)|} \cdot \frac{1}{|Y_c(j\omega_c)|} \quad (2.10)$$

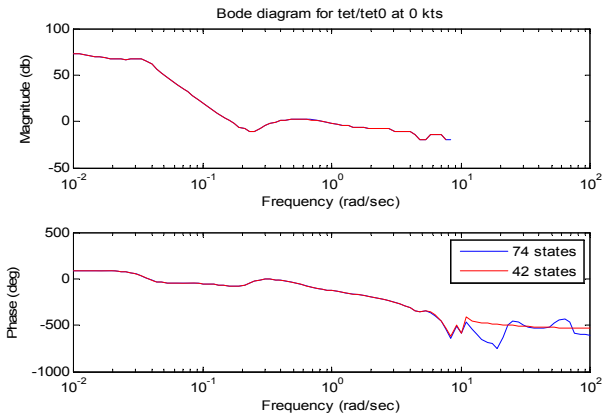
is calculated to ensure that the desired ω_c is obtained.

Table 2.8

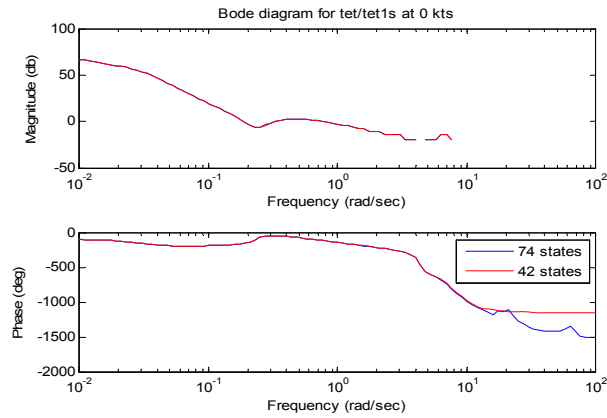
k	K_1	K_2	$T_1(\text{sec})$	$\tau_0(\text{sec})$	ζ_n	$\omega_n(\text{rad/s})$
0	1.0	2.0	5.0	0.15	0.707	10.0
1	1.0	2.0	5.0	0.15	0.707	10.0
2	1.0	10.0	2.0	0.15	0.707	10.0

The pilot vehicle system will be simulated using disturbance or/and command signals for u_m . The measure of pilot workload is computed as root mean square value (rms) of u_m/K_e for the study of flight speed effect on the band width phase delay criterion. The handling qualities sensitivity function (HQSF) will be estimated at the crossover frequency ω_c for the magnitudes of the transfer function u_m/c .

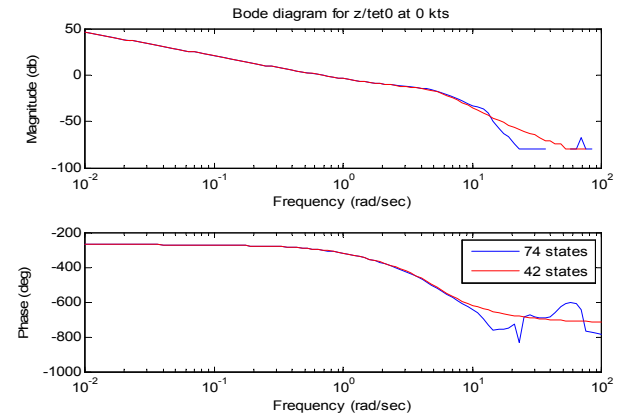
$$\frac{\theta}{\theta_0}, \tau=0.344$$



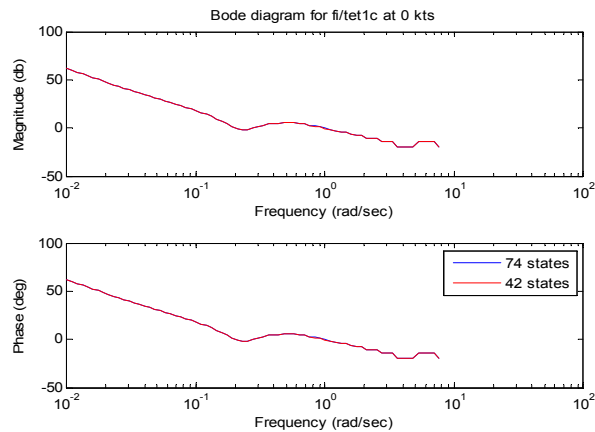
$$\frac{\theta}{\theta_{1s}}, \tau=0.303$$



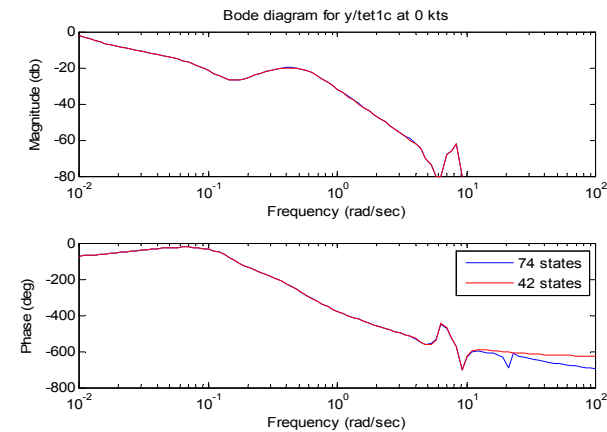
$$\frac{z}{\theta_0}, \tau=0.307$$



$$\frac{\phi}{\theta_{1c}}, \tau=0.322$$



$$\frac{y}{\theta_{1c}}, \tau=0.363$$



$$\frac{p}{\theta_{1c}}, \tau=0.333$$

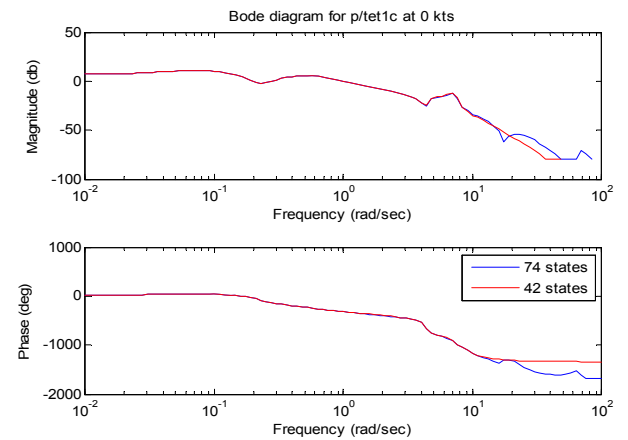
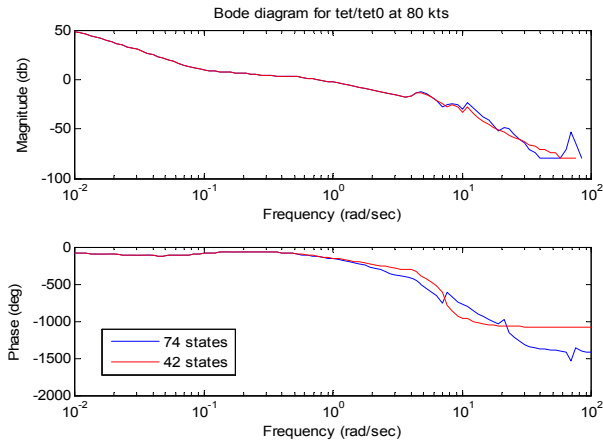
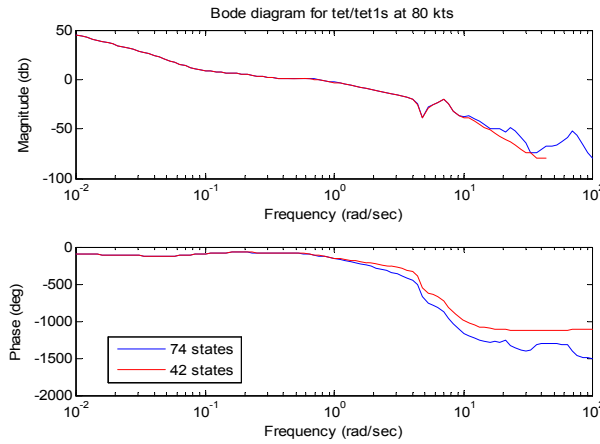


Figure 2.28a. Open-loop pilot-vehicle transfer function at hover

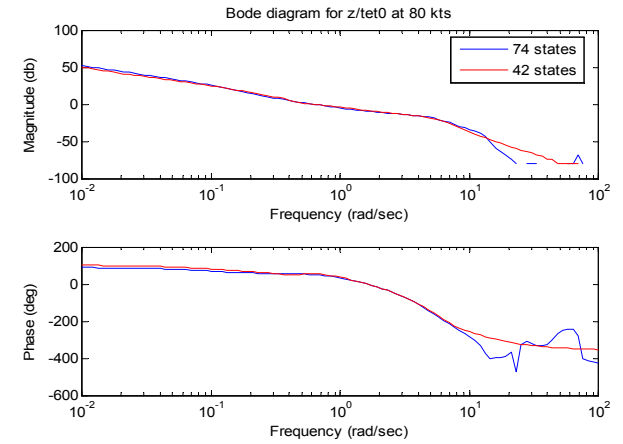
$$\frac{\theta}{\theta_0}, \tau=0.363$$



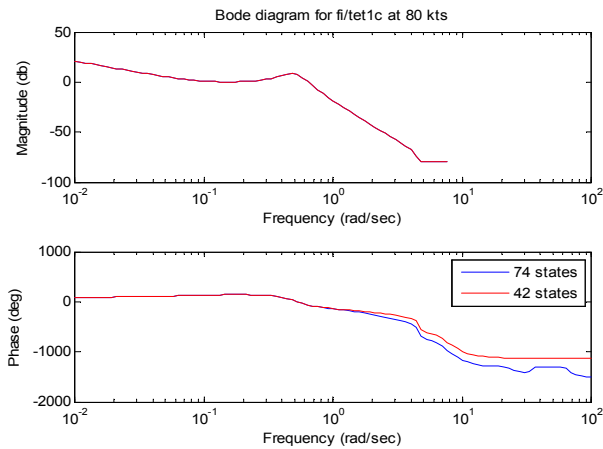
$$\frac{\theta}{\theta_{1s}}, \tau=0.384$$



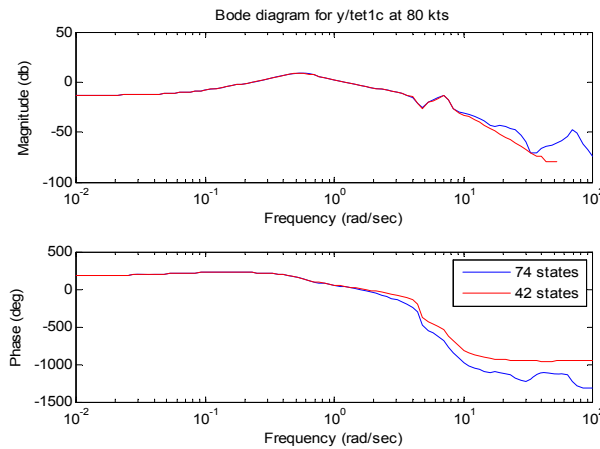
$$\frac{z}{\theta_0}, \tau=0.303$$



$$\frac{\varphi}{\theta_{1c}}, \tau=0.357$$



$$\frac{y}{\theta_{1c}}, \tau=0.285$$



$$\frac{p}{\theta_{1c}}, \tau=0.327$$

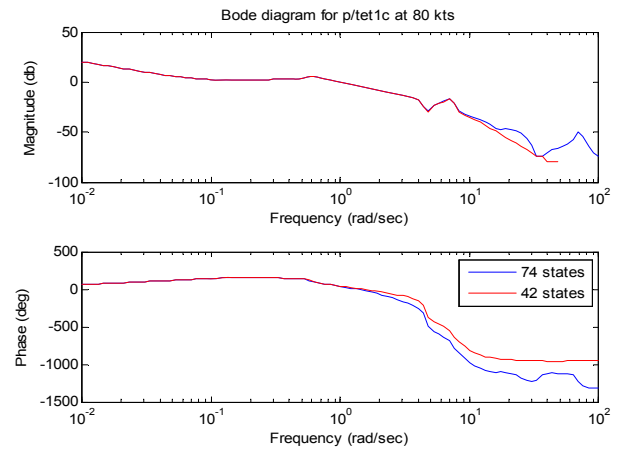
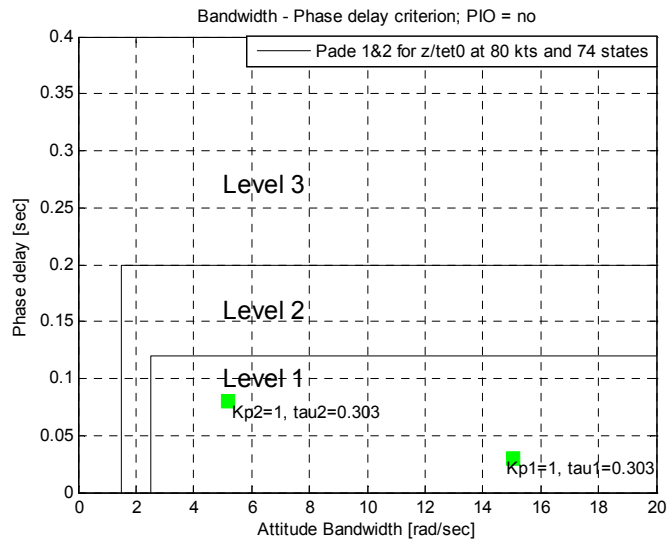


Figure 2.28b.

Open-loop pilot-vehicle transfer function at 80 kts

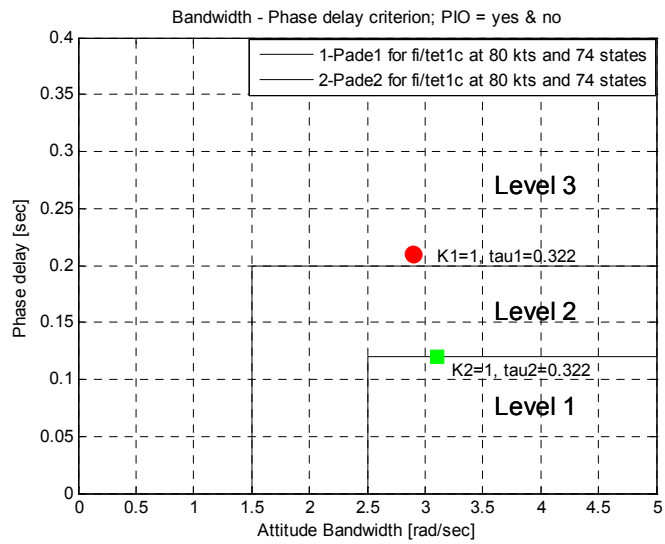
Wbpdriterion
at 0 kts

$$\frac{z}{\theta_0}, \tau=0.307$$



Wbpdriterion
at 80 kts

$$\frac{\varphi}{\theta_{1c}}, \tau=0.357$$



$$\frac{z}{\theta_0}, \tau=0.303$$

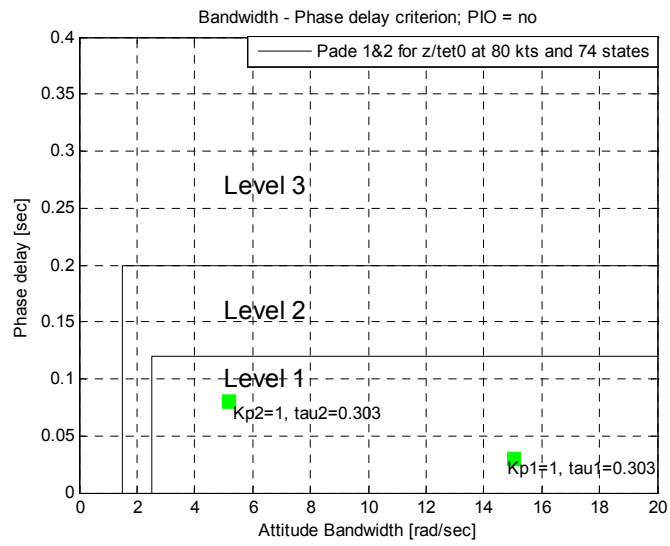
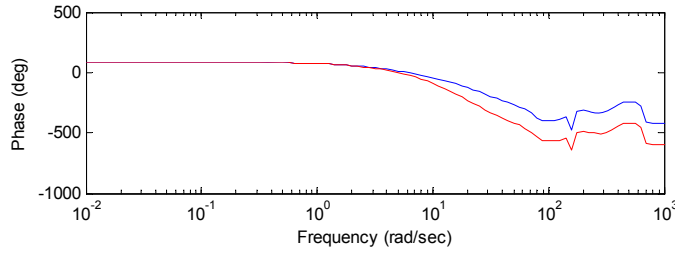
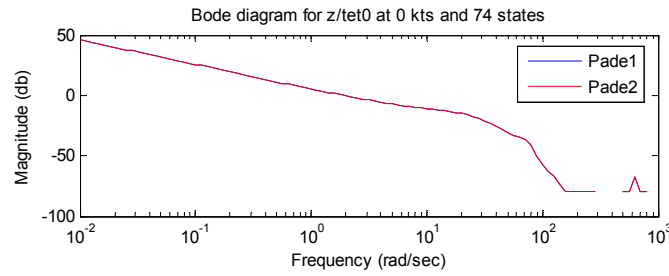


Figure 2.29. Effective delay approximation

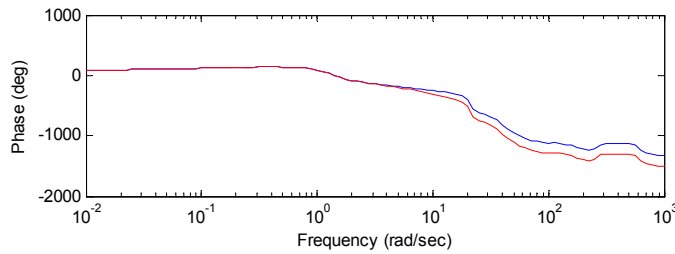
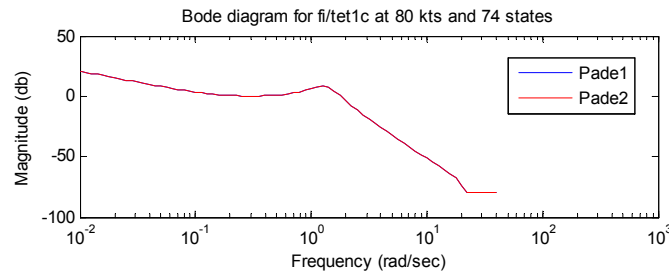
Bode diagram at 0 kts

$$\frac{z}{\theta_0}, \tau=0.307$$



Bode diagram at 80 kts

$$\frac{\varphi}{\theta_{1c}}, \tau=0.357$$



$$\frac{z}{\theta_0}, \tau=0.303$$

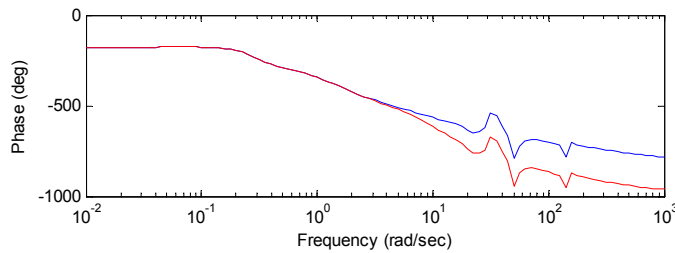
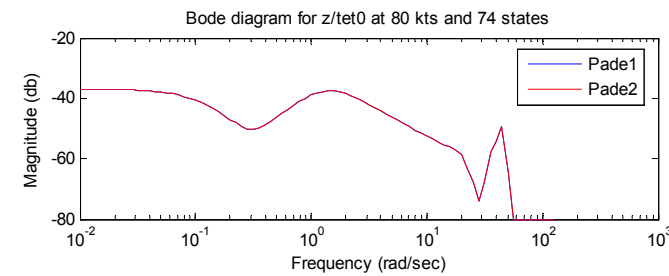


Figure 2.30. Open-loop pilot-vehicle transfer function with Pade approximation

Similar that in 2.2.2.1 part the common crossover frequency ω_c for the open-loop pilot vehicle was chosen to be 2 rad/sec for longitudinal channel and 2.5 rad/sec for the lateral one. It is found that in order to achieve crossover model characteristics in the crossover region for longitudinal and lateral-directional cases a lead compensation $k=2$ is chosen.

The value of T_2 and K_e as function of task and configuration are summarized in table 2.9. With the vehicle – pilot model set-up as described above the root mean square value of the signal in the proprioceptive feedback pathway of pilot model, u_m will be used as a measure of pilot workload.

Table 2.9

0 kts	Longitudinal			Lateral-Directional		
	$\frac{\theta}{\theta_0}$	$\frac{\theta}{\theta_{1s}}$	$\frac{z}{\theta_0}$	$\frac{\varphi}{\theta_{1c}}$	$\frac{y}{\theta_{1c}}$	$\frac{p}{\theta_{1c}}$
T_2	0.6893	0.6893	0.5233	0.9862	0.1774	0.9862
K_e	14.94	2.8308	0.2403	1.5437	4.3744	0.6173
80 kts	Longitudinal			Lateral-Directional		
	$\frac{\theta}{\theta_0}$	$\frac{\theta}{\theta_{1s}}$	$\frac{z}{\theta_0}$	$\frac{\varphi}{\theta_{1c}}$	$\frac{y}{\theta_{1c}}$	$\frac{p}{\theta_{1c}}$
T_2	0.4144	0.4144	0.8014	0.9491	0.3570	0.9491
K_e	9.4453	2.7742	0.2819	1.7210	1.7328	0.6785

3. Aircraft Pilot Modelling by Transfer Function Approach

Figure 3.1 shows block-diagram of the operational activity of a pilot, who performs deliberate control actions in presence of different feedback: visual and motion (acceleration) control feedbacks. According to the categories given in [55,56], accelerations are known to affect piloting beneficially in some cases and negatively in some others: on the one hand, accelerations are the information factor, that is they give the information of aircraft motion which helps a pilot to control an aircraft; on the other hand, accelerations are the physiological (biodynamical) factor as they cause body displacement which may be assessed negatively by the pilot.

The high-frequency oscillations due to structural elasticity refer to the biodynamic factor, since they lead to involuntary body and limb-manipulator system displacements, which interfere with pilot voluntary control activity and, finally, worsen handling quality ratings.

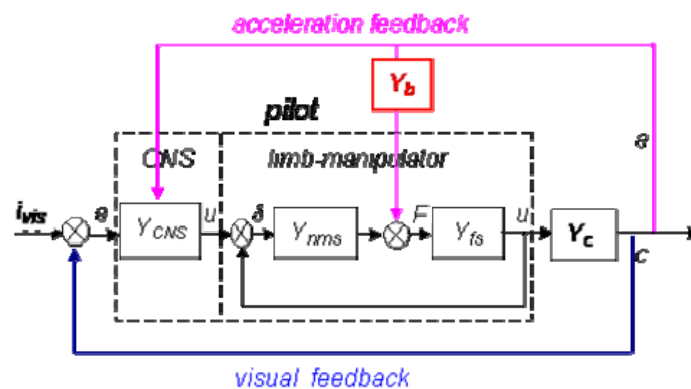


Figure 3.1. Block-diagram of the pilot model with visual and motion feedbacks.

When a pilot controls an elastic aircraft, he, on the one hand, performs a piloting task, and, on the other hand, he is exposed to the disturbing high-frequency oscillations due to structural elasticity. In other words, pilot control activity consists of two components: deliberate and involuntary, created by so-called “active” and “biodynamical” pilots. The two “pilots” are differently motivated since their inputs are different: for “active” pilot, the input is a visual signal; for “biodynamical” pilot, the input is the high-frequency oscillations. The characteristics frequency ranges of the pilot models are also different: the “active pilot” is limited in the region 1.0-1.5 Hz; the “biodynamical” pilot is above 1.5 Hz. These facts allow us to isolate the “biodynamical” pilot model from the integrated model of pilot activity (Figure 3.2), and consider it separately.

TsAGI’s task in ARISTOTEL is to estimate of the effects of manipulator type and feel system characteristics on handling qualities of aero-elastic aircraft. Existing APC criteria do not practically take into account aircraft manipulator feel system characteristics and control sensitivity, although their effects can be considerable. In Russia, early investigations revealed that APC tendencies of flexible transport aircraft can be attributed to the same trigger: a resonant peak of the pilot’s neuromuscular system frequency response at 2-3Hz [57]. However, these are still not considered in the design analysis. Taking into account the reasoning above, the effect of these characteristics is determined by their effect on “active” and “biodynamic” pilots. The integral response of the two pilots forms a pilot rating of aero-elastic aircraft handling qualities.

To determine the effect of manipulator type and feel system characteristics, special “biodynamic” experiments were conducted [58, 59], which made the basis for “active” and “biodynamical” pilot modelling.

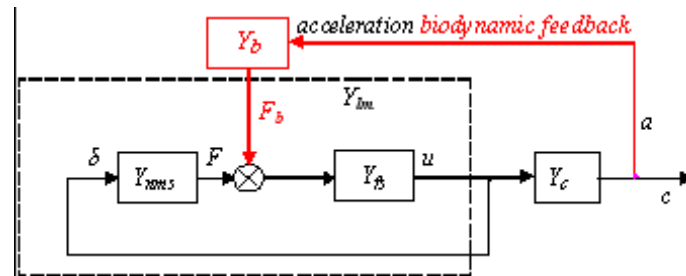


Figure 3.2. Block-diagrams of the “biodynamical” pilot model.

3.1. Database for the Model Development

The database for the pilot modeling development were experimental describing functions determined from “biodynamical” experiments. Experiments were conducted in flight simulators at TsAGI (PSPK-102) and NLR (GRACE). Description of the experimental facilities, as well as experimental procedure of the experiments is presented in detail in [59]. The procedure was constructed in a way to receive describing functions of both “active” and “biodynamical” pilots for different manipulator type (wheel, side stick, center stick) and feel system characteristics (force gradient F_{δ_s} , damping $F_{\dot{\delta}}$, friction F_{fr} , breakout force F_{br}).

Two NLR pilots, one TsAGI pilot and two human-operators participated in experiments. As a whole, more than 650 runs were performed with the subjects.

Experiments were conducted in two series: (1) with pilot in the loop to receive active pilot describing functions, and (2) without pilot in the loop to receive biodynamical pilot describing functions. In the first series of experiments the pilots performed roll compensatory tracking task; in the second series, the human pilots were exposed to lateral accelerations produced by flight simulator motion system.

All the inceptors were loaded by the electrical loading system, which allows flexible changing of feel system characteristics. The manipulator forces were modeled in accordance with the following equation:

$$m\ddot{\delta} + F_{\dot{\delta}}\dot{\delta} + F_{\delta}\delta = F_{br} \operatorname{sgn}\delta + F_{fr} \operatorname{sgn}\dot{\delta} + F_p,$$

where: m is inceptor mass, $F_{\dot{\delta}}$ is damping, F_{δ} is force gradient, F_{br} is breakout force, F_{fr} is friction, F_p is pilot force.

In experiments, the describing functions of the active and biodynamical pilot models were determined. The describing functions were found through cross and auto spectral density, which were calculated using Fast Fourier Transform:

$$\text{For the active pilot: } \begin{Bmatrix} \delta_s \\ e \end{Bmatrix} = \frac{S_{\delta_s-\varphi}(j\omega)}{S_{e-\varphi}(j\omega)}$$

$$\text{For the biodynamical pilot: } \left\{ \frac{\delta_s}{a} \right\} = \frac{S_{a-\delta_s}(j\omega)}{S_{a-a}(j\omega)}$$

where δ_s is stick displacement; e is a visual tracking error signal; a is accelerations produced by motion platform.

Results from biodynamical tests are presented in [60, 61]. Here, we give more thorough analysis of the data, useful for pilot modeling. The experimental describing functions are presented in Figures 3.3 – 3.5 for the active pilot model, and in Figures 3.6 – 3.8 for the biodynamical pilot model.

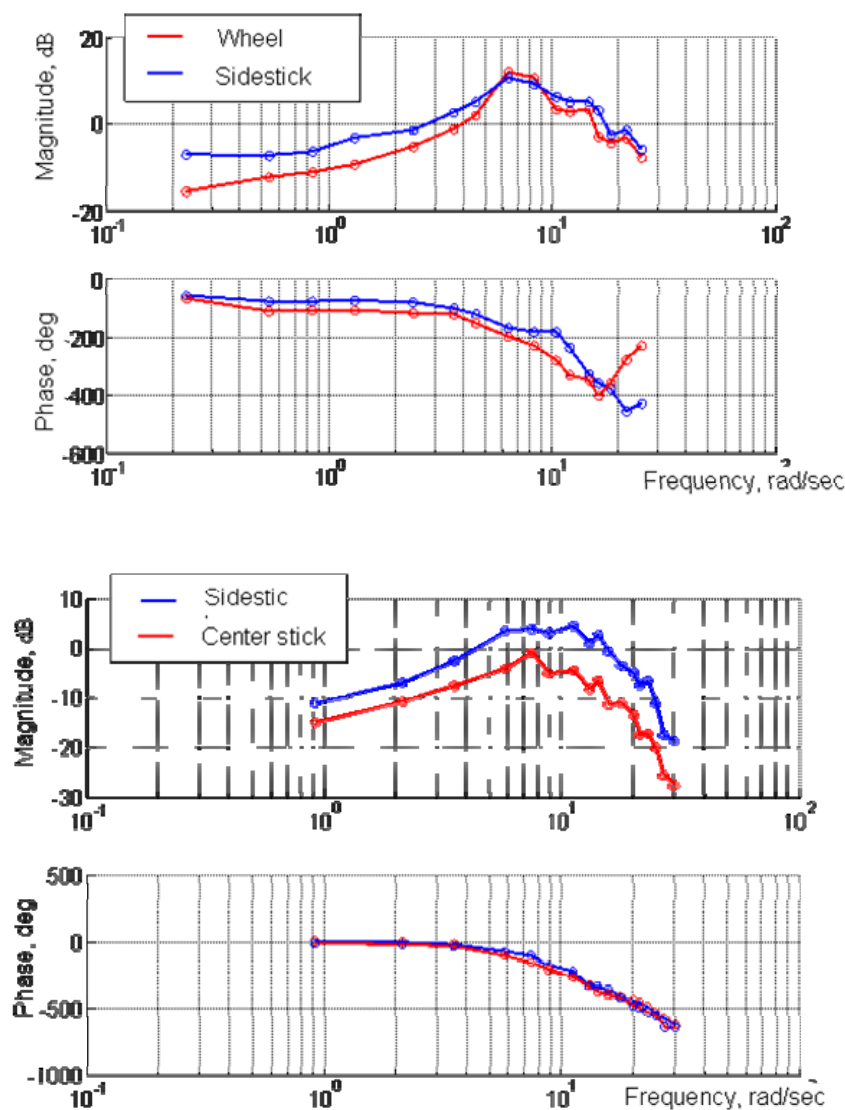


Figure 3.3. Active pilot. Effect of inceptor type. TsAGI data (upper) and NLR data (lower).

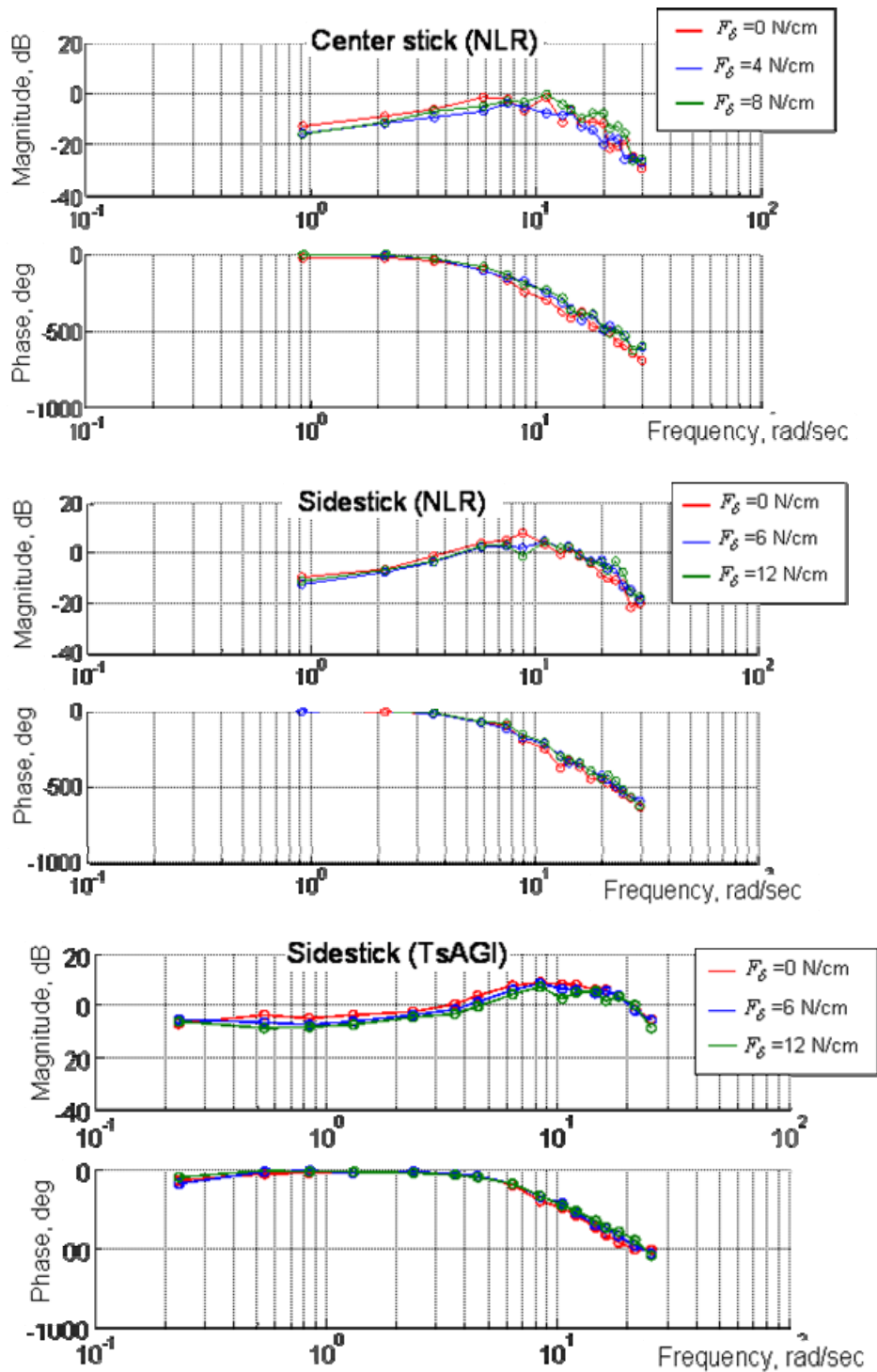


Figure 3.4. Active pilot. Effect of force gradient for center stick (upper) and sidestick (middle), NLR data, and sidestick (lower), TsAGI data.

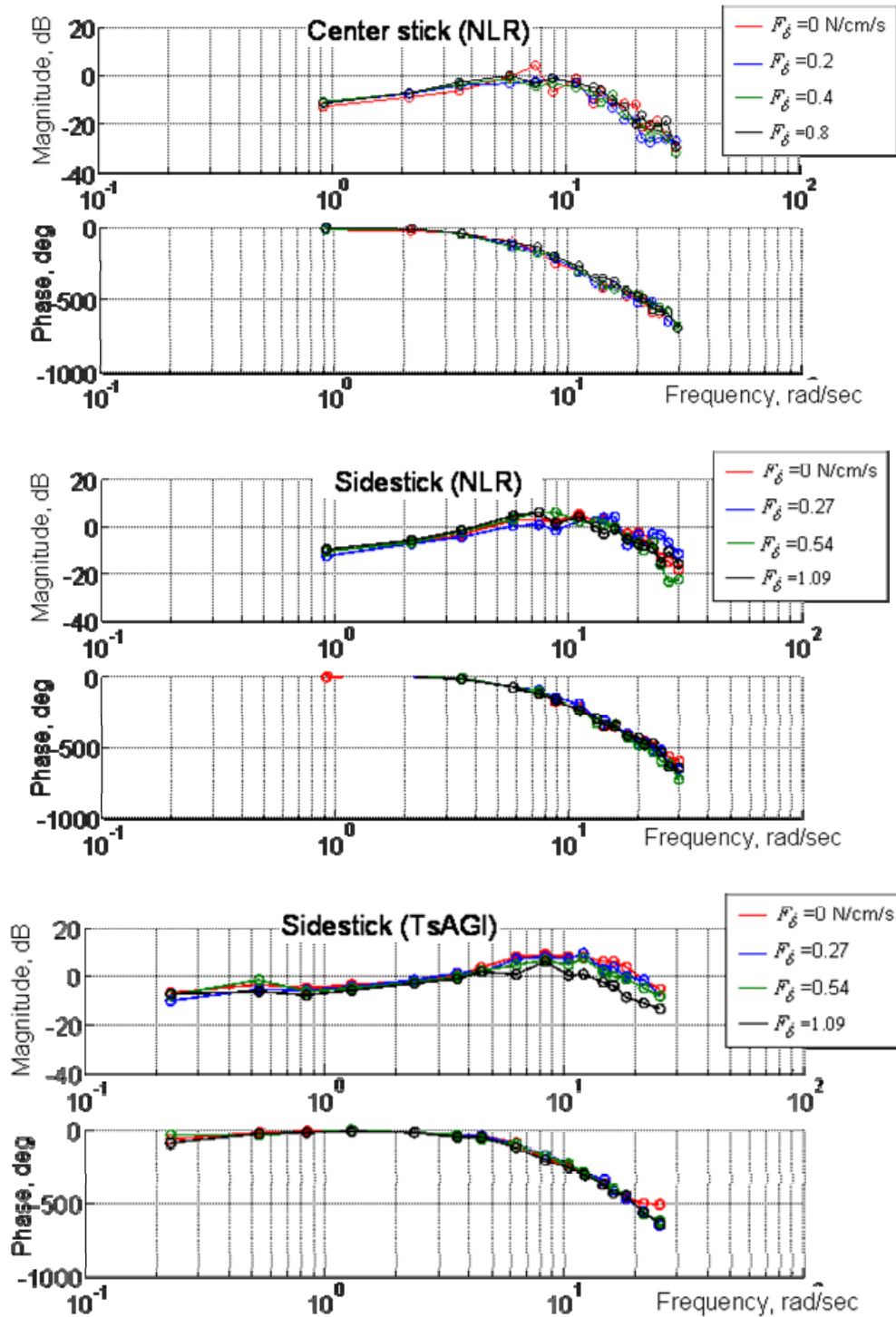


Figure 3.5. Active pilot. Effect of damping for center stick (upper), sidestick (middle) NLR data, and sidestick (lower), TsAGI data.

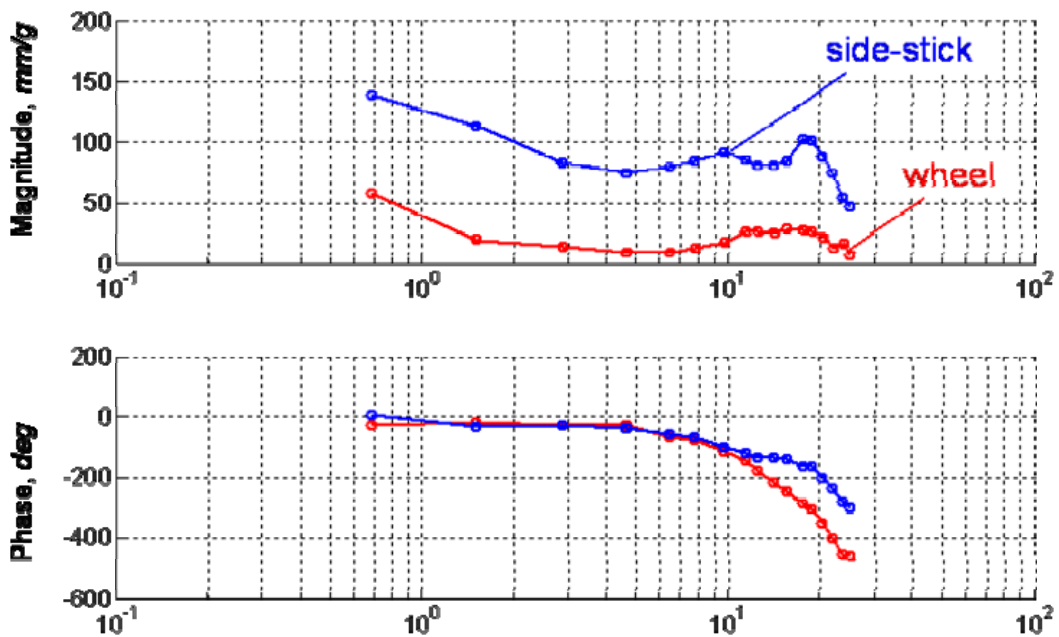


Figure 3.6. Biodynamical pilot. Effect of inceptor type. TsAGI data.

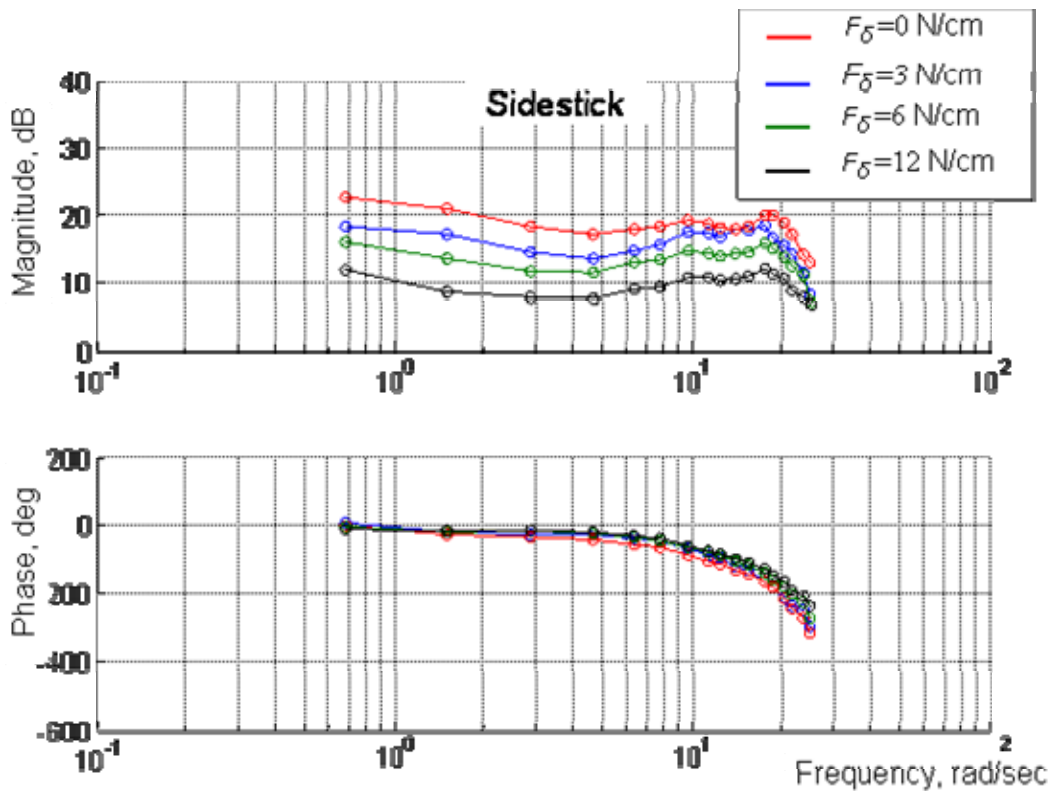


Figure 3.7. Biodynamical pilot. Effect of sidestick force gradient. TsAGI data.

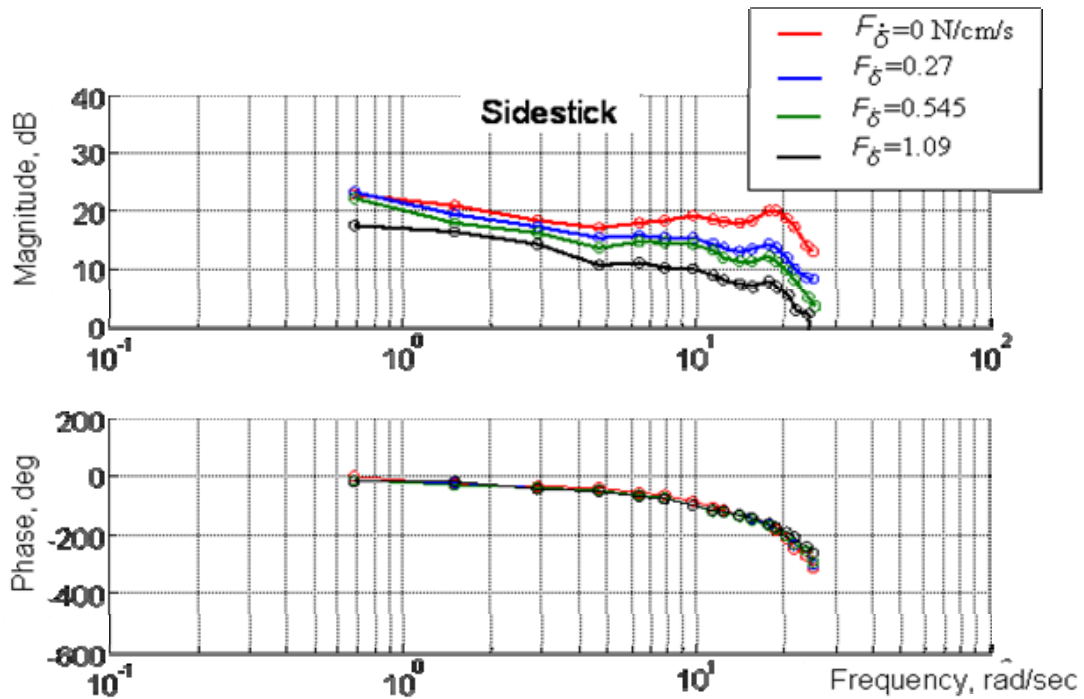


Figure 3.8. Biodynamical pilot. Effect of sidestick damping. TsAGI data.

Before we start analysis of the experimental data, a few general observations should be made:

1. Effect of inceptor feel system characteristics on pilot describing functions do not practically depends on pilots' inertial characteristics (size and weight), at least for the sidestick and wheel control. For the sidestick, it can be attributed to the arm resting on the armrest; for the wheel it is attributed to the fact the wheel displacements created by one hand are compensated for by that created by the other hand. This fact allows us to average the data received for all pilots, and make general conclusions. Nevertheless, for a central stick the effect of pilots' inertial characteristics may be more evident due to the lack of the armrest in this case.
2. Effect of feel system characteristics on, accordingly, active and biodynamic pilot models can be analyzed for the frequency ranges typical of the models. For active pilot model it is frequencies below 1.5 Hz; for biodynamical pilot model it is frequencies above 1.5 Hz.
3. As it was stated in previous ARISTOTEL Deliverables and some publications (see, for example, [61]), within a limited range of friction and breakout forces variation, the effect of breakout force on biodynamic interaction (BDI) is somewhat similar to the effect of force gradient, and the effect of friction is similar to the effect of damping. Thus, we will pay here the greater attention to the effect of force gradient and damping.

The effects of inceptor type and feel system characteristics are considered separately for active pilot and for biodynamic pilot.

Active pilot data.

- 1) The inceptor type affects the describing function gain at the low frequencies. Figure 3.3 presents data received for the wheel, central and side sticks for the close-to-optimum values of their feel system characteristics (wheel: $F_{\delta_s}=2$ N/cm, $F_{\dot{\delta}}=0.27$ N/cm/s, $F_{b_r}=0$, $F_{f_r}=0$; side stick: $F_{\delta_s}=6$ N/cm, $F_{\dot{\delta}}=0.27$ N/cm/s, $F_{b_r}=0$, $F_{f_r}=0$; central stick: $F_{\delta_s}=8$ N/cm, $F_{\dot{\delta}}=0$, $F_{b_r}=0$, $F_{f_r}=0$). The data were received on TsAGI's PSPK-102 flight simulator (wheel and sidestick) and NLR GRACE flight simulator (center stick and sidestick). Compared to traditional inceptors (wheel and central stick) a sidestick has 2.5 – 3 times less displacements, higher velocity capabilities, lower time delay. In other words, the limb-manipulator system with a sidestick has higher dynamic properties.

This conclusion is supported by experiments. Figure 3.9 presents data received earlier in [57]. It is seen that for a sidestick the pilot delay τ decreases compared to the traditional wheel and center stick. As a result, the overall pilot response time decreases, and pilot gain increases. The data were received for the pitch axis, but, in kind, they can be applied to the roll control axis as well. Thus, it is natural that the active pilot describing function for a sidestick has greater gain than that for the wheel and center stick.

- 2) If inceptor force gradient is within the range typical of practice (for a sidestick it is within 3-6 N/cm), its variation does not affect active pilot describing function (Figure 3.4). The effect of gradient is not noticeable outside the optimum range as well, though some tendencies can be detected. As forces gradient is smaller than optimum or zero, the inceptor deflections become more extensive, and the describing function gain increases at the low frequencies. As the force gradient increases over the optimum, the gain slightly decreases due to the reduced capabilities of neuromuscular system to adapt to increased inceptor forces.

Usually, the force gradient is selected from point-of-view of the rigid-body aircraft handling qualities; its optimum values vary in the rather narrow range. As force gradient deflects from the optimum values, the pilot ratings deteriorate: due to (low-frequency) PIO tendency for values smaller than optimum; due to too large inceptor forces for gradient values greater than optimum. The pilot ratings deterioration can be estimated in accordance with the function presented in Figure 3.10 [62].

It should be mentioned also that the subjective pilot ratings appeared to be more “sensitive” to force gradient variation than the pilot describing function.

The data received at TsAGI and NLR for sidestick are comparable in terms of the effect of feel system characteristics, but different in terms of gain. This difference is natural, since the experiments were conducted in different simulators, different visual inputs (their spectrum were different) and different aircraft command gradients (gains) were used. These factors may affect the active pilot gain, i.e. amplitude of frequency response.

- 3) Figure 3.5 shows that the inceptor damping does not affect active pilot describing function at the low frequencies for the rather wide range of the parameter variation (from 0 up to very large damping, which is unusual for practice). The point is that at the frequencies typical of active control, the introduction of additional damping does not lead to any noticeable increase of inceptor forces felt by a pilot, and, thus, does not affect handling qualities pilot ratings.

To confirm the statement, Figures 3.11, 3.12 shows the data received for the wheel in the course of one of TsAGI study. Figure 3.11 shows pilot ratings received for the two test pilots for different values of the damping coefficient; the values varied from $\zeta=0.3$ up to 1.2. It is seen that despite of the fact the damping varied in a large range, the pilot ratings do not noticeably changed. Figure 3.12 shows the percentage of forces due to damping referred to the total wheel forces estimations as a function of force gradient and damping coefficient. It is seen, in particular, that the greater is force gradient, the smaller is the contribution of damping forces.

At high frequencies above 1.5-2 Hz, there is a certain drop in describing function amplitude, which increases with damping. But such describing function distortions are the matter of biodynamical pilot component rather than active pilot.

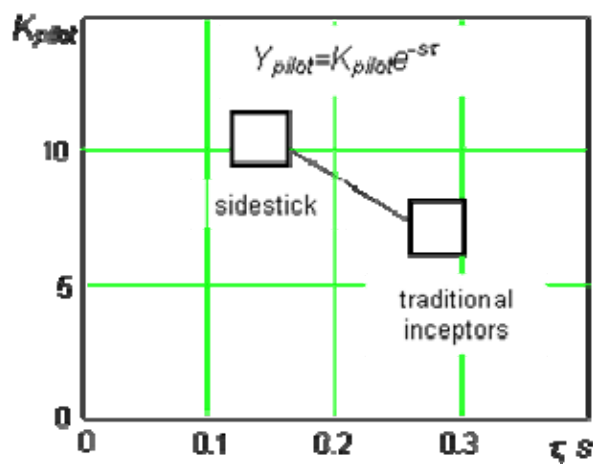


Figure 3.9. Dynamic properties of an active pilot in pitch with different inceptors.

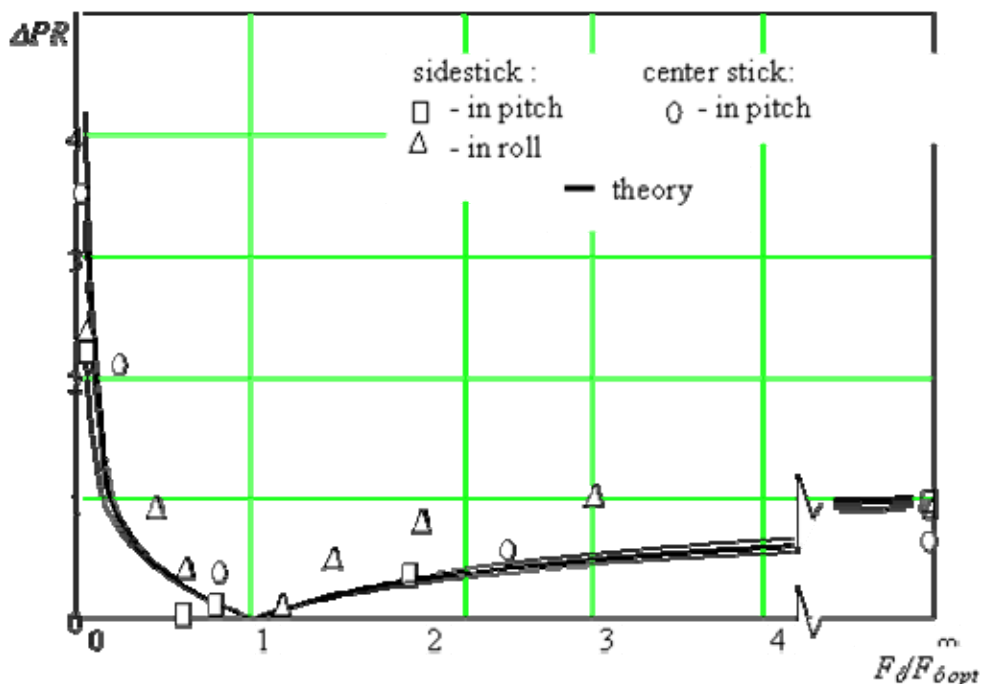


Figure 3.10. Pilot ratings of the rigid-body aircraft vs inceptor force gradient.

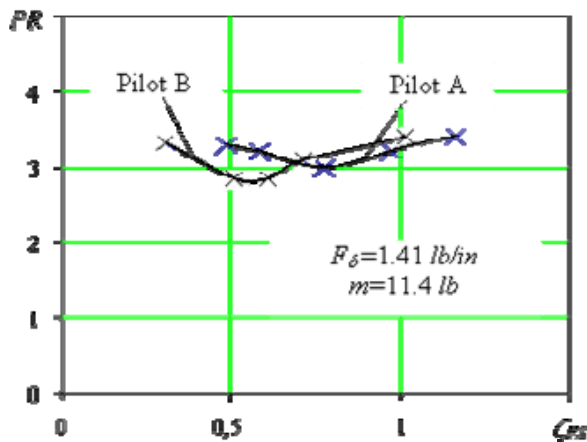


Figure 3.11. Pilot ratings as a function of wheel damping ratio.

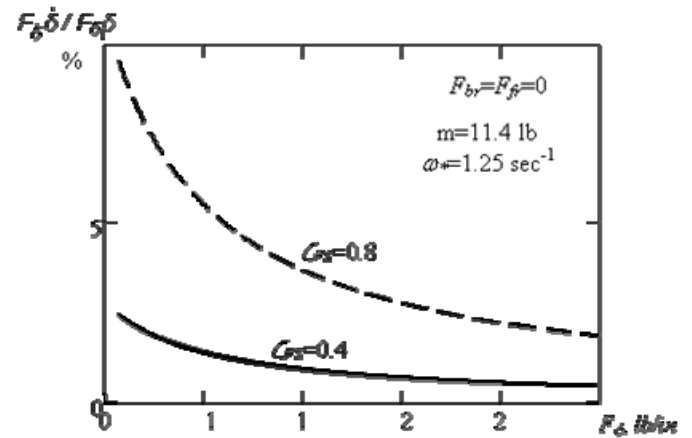


Figure 3.12. The contribution of the damping force to the total wheel force.

Biodynamical pilot data.

- 1) The type of inceptor affects biodynamical interaction (BDI) intensity in a considerable extent. Figure 3.6 shows that, in degree, BDI tendency with a wheel 3 times less than with a sidestick. In kind, the effect of feel system characteristics on BDI is similar for the wheel and sidestick. Therefore, the further analysis of the feel system effect will be conducted based on sidestick results.
- 2) As it is seen from Figure 3.7, if the force gradient is within its optimum range, its variation does not noticeably reduce BDI tendency within the whole range of frequencies. To make the reduction of BDI tendency more effective, we need to increase the force gradient more than twice as much. But this can lead to handling quality ratings worsening (see Figure 3.10).
- 3) As inceptor damping increase, the BDI tendency decreases noticeably, at high frequencies in particular: as F_{δ} increases from 0.25 to 1.0 N/cm/s, the high-frequency oscillations tendency becomes 4 times less (Figure 3.8). It should be mentioned that within the values considered in experiments, the effect of damping on pilot ratings is practically negligible (see Figures 3.11, 3.12).

Thus, the analysis conducted allows us to make a few conclusions useful for pilot modeling:

1. Inceptor feel system characteristics do not practically affect describing function of the active pilot, though can worsen considerably pilot ratings of aircraft handling qualities.
2. Biodynamical interaction (biodynamical pilot describing function) depends on the type of inceptor. Among the traditional wheel and a sidestick, the BDI is less pronounced for the wheel.
3. Inceptor damping is the most effective method to suppress high-frequency oscillations, since, first, its variation in a wide range does not worsen pilot HQ ratings, and, second, it decreases the high-frequency inceptor oscillations in a considerable extent.

3.2. Pilot Modelling to Take Into Account Inceptor Feel System Characteristics

The analysis performed in the previous Chapter allows identification of the pilot model transfer functions. In accordance with the assumed splitting of the pilot activity, transfer functions are identified for the “active” and “biodynamical” pilot models.

The modern mathematical software, such as Matlab and others, allows identification of a system transfer function on the basis of its frequency response. The transfer function received in such a way is the function, which numerator and denominator are high-order polynomials. But in this case, any other feel system configuration is described by new polynomials with new set of coefficients, and no adjusting rules can be determined for these coefficients as a function of feel system characteristics. Thus, the transfer functions identified by polynomials can not be applied for further study of the effect of feel system characteristics and for the development of HQ criteria. The adjustment rules can be determined if the structure of the transfer function is known and given as a set of elementary functions (aperiodic, oscillatory, etc.). The main goal of the present Chapter is to determine the structure of transfer functions for the active and biodynamical pilot models, and to determine the rules of their parameters adjustment as a function of feel system characteristics.

Active pilot modelling.

The describing functions of active pilot model (visual tracking) presented in Figures 3.3 – 3.5 show that there are two resonant peaks in amplitude characteristics at the frequencies above 1 Hz. This is characteristic of the function of no less than the fourth order. The comparison of the experimental describing functions and that calculated in accordance with the identified transfer functions, which is conducted later on, shows that the best coincidence of the describing functions is achieved for the transfer function of the following structure:

$$Y_{ap}(s) = K \cdot e^{-s\tau} \cdot (T_L s + 1) \cdot \left[\frac{1}{T_1^2 s^2 + 2T_1 \zeta_1 s + 1} \right] \cdot \left[\frac{1}{T_2^2 s^2 + 2T_2 \zeta_2 s + 1} \right] \quad (3.1)$$

The active pilot model (3.1) differs from the generally used model by the two additional oscillatory units, which describe the limb-manipulator system dynamics.

The analysis conducted above shows that the feel system characteristics do not practically affect active pilot describing function. Thus, from point of view of the best coincidence of the experimental and calculation data, we can propose the following values for the parameters of function (3.1) regardless of feel system characteristics and the type of inceptor:

$$\tau=0.2s; T_L=0.4s; T_1=0.12s; \zeta_1=0.3s; T_2=0.05s; \zeta_2=0.3s.$$

It should be mentioned that the identified values of τ and T_L are typical of that generally used to describe pilot control behavior.

The values of gain coefficient K in function (3.1) depends on the type of inceptor and aircraft control sensitivity.

Figure 3.13 confirms the validity of the identified transfer functions by their comparison with the experimental describing functions of the active pilot model for different inceptor types.

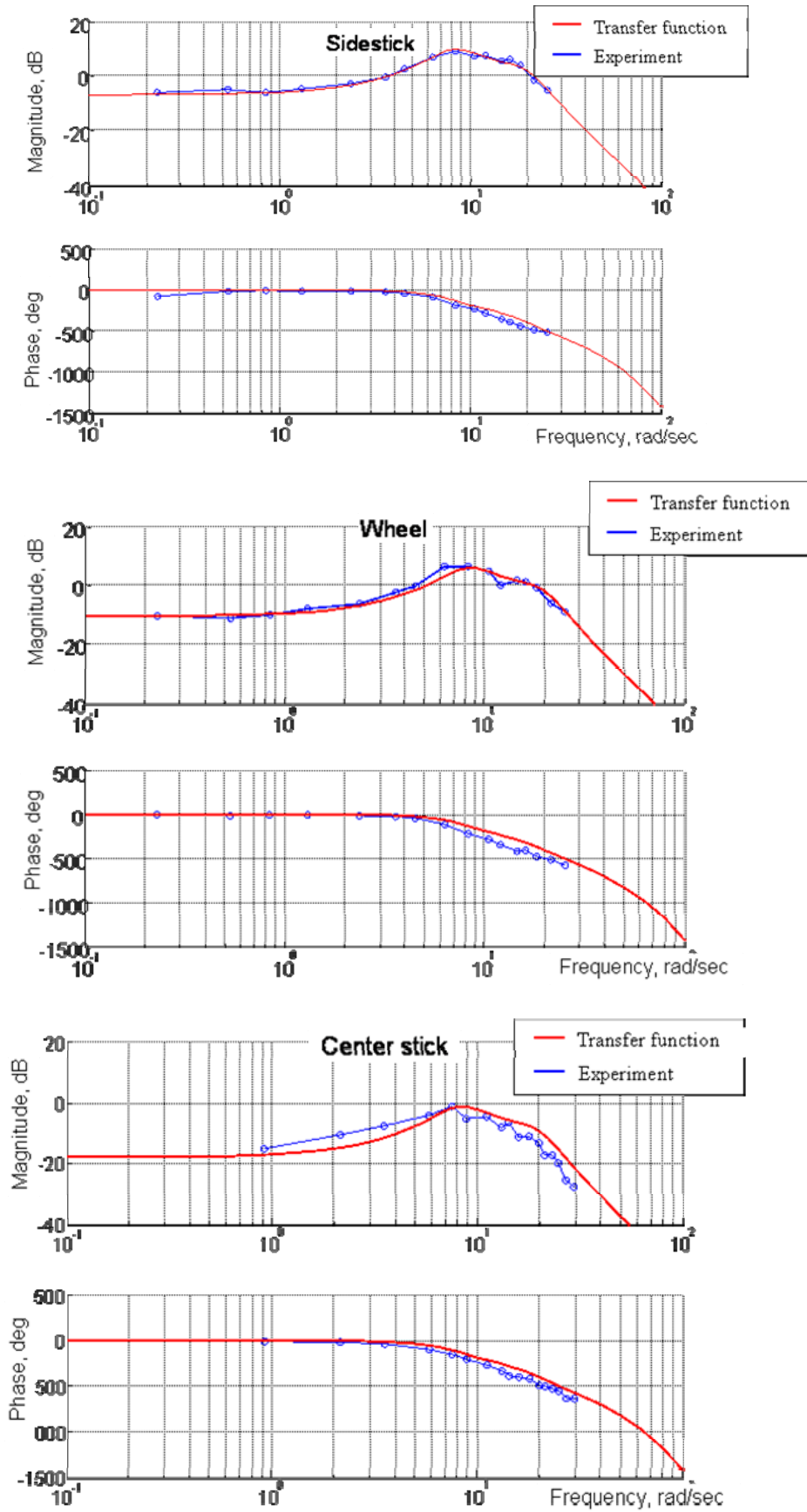


Figure 3.13. Active pilot. Comparison of the experimental describing function with that calculated in accordance with the identified transfer functions.

Biodynamical pilot modelling.

As for the active pilot, the structure of the transfer function for the biodynamical pilot model is selected from the point of view of the best coincidence of the calculated and experimental data.

The following transfer function structure provides the best agreement between the calculated and experimental describing functions:

$$Y_{bp}(s) = K \cdot \left(\frac{Ts + 1}{T_I s + 1} \right) \cdot \left[\frac{1}{T_1^2 s^2 + 2T_1 \zeta_1 s + 1} \right] \cdot \left[\frac{1}{T_2^2 s^2 + 2T_2 \zeta_2 s + 1} \right] \quad (3.2)$$

For the “zero” set of feel system characteristics, the values of the parameters in function (3.2) are as follows:

- for the sidestick: $K=180\text{mm/g}$, $T=0.4\text{s}$; $T_1=1.0\text{s}$; $T_1=0.1\text{s}$, $\zeta_1=0.45$; $T_2=0.05\text{s}$; $\zeta_2=0.1$;
- for the wheel: $K=50\text{mm/g}$, $T=0.4\text{s}$; $T_1=3.0\text{s}$; $T_1=0.08\text{s}$, $\zeta_1=0.2$; $T_2=0.05\text{s}$; $\zeta_2=0.1$.

If the feel system characteristics are non-zero, the parameters of function (3.2) change in accordance of the functions shown in Figure 3.14 for the force gradient and in Figure 3.15 for the damping.

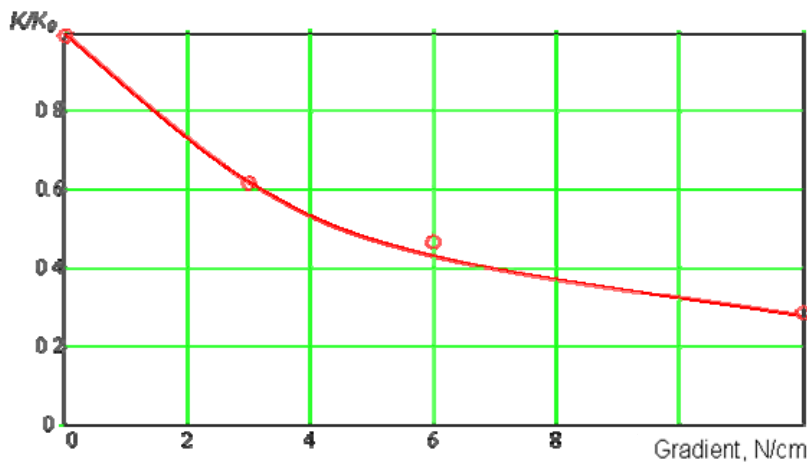


Figure 3.14. Biodynamical pilot. Transfer function parameter adjusting for the effect of inceptor force gradient.

The increase of force gradient, i.e. limb-manipulator system stiffness, leads to biodynamic interaction reduction, which is expressed by gain K (Figure 3.14, K_0 is the value for “zero” gradient). The values of other parameters in (3.2) can be left unchanged, since their effect is negligible.

The inceptor damping leads to more complicated interdependence of the parameters of function (3.2), which is caused, seemingly, by more complex biomechanical interaction in the body-limb-manipulator system. To simplify the process of adjustment, two parameters were selected, which changes are more noticeable. They are: parameter T_I and the damping ratio of the second oscillatory unit ζ_2 . Their adjustment functions are shown in Figure 3.15 (in the Figure the parameters are shown referred to their value for “zero” damping).

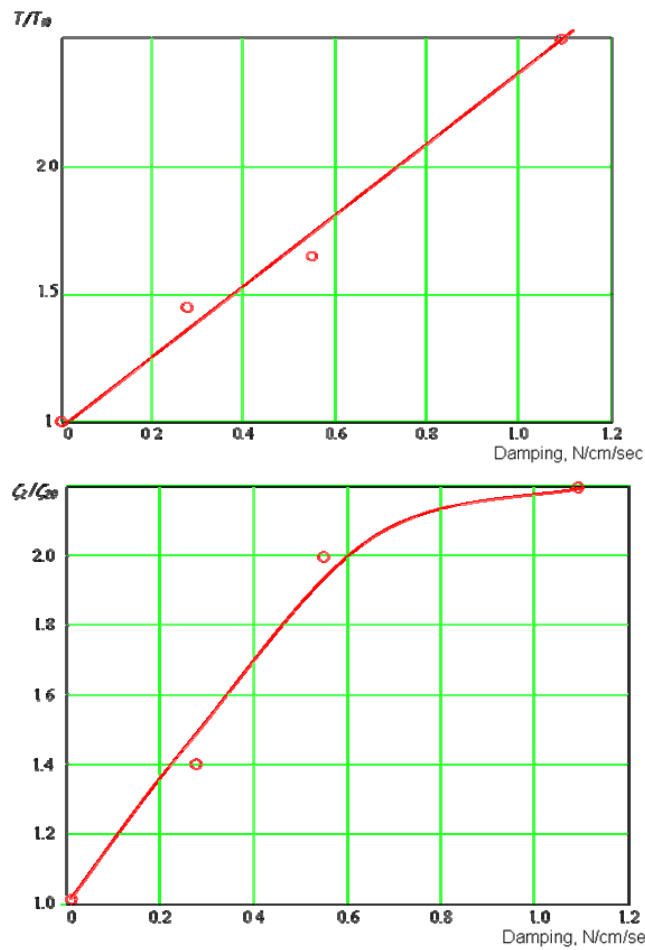


Figure 3.15. Biodynamical pilot. Transfer function parameter adjusting for the effect of inceptor damping.

Figures 3.16 – 3.18 confirm the validity of the identified transfer functions by their comparison with the experimental describing functions of the biodynamical pilot models.

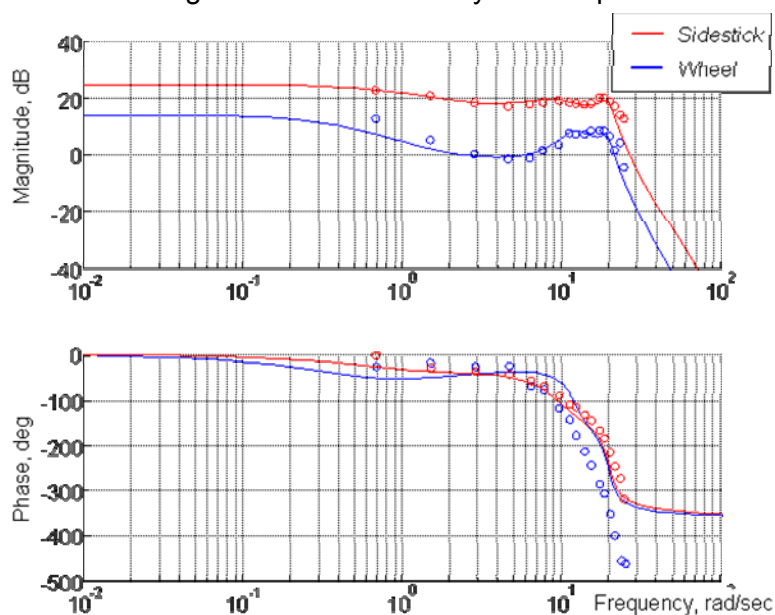


Figure 3.16. Biodynamical pilot. Comparison of the experimental describing function with that calculated in accordance with the transfer functions. Different inceptors.

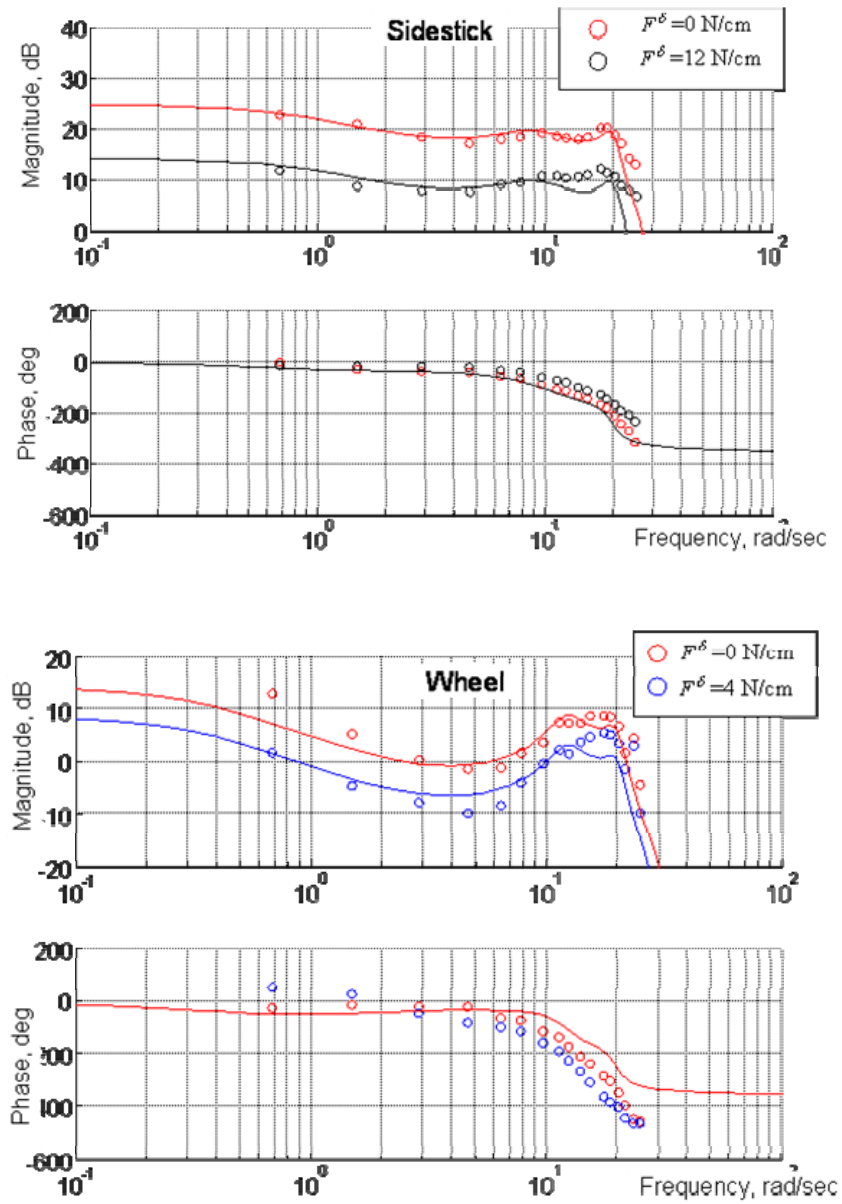


Figure 3.17. Biodynamical pilot. Comparison of the experimental describing function with that calculated in accordance with the transfer functions.
Sidestick, wheel, - effect of force gradient.

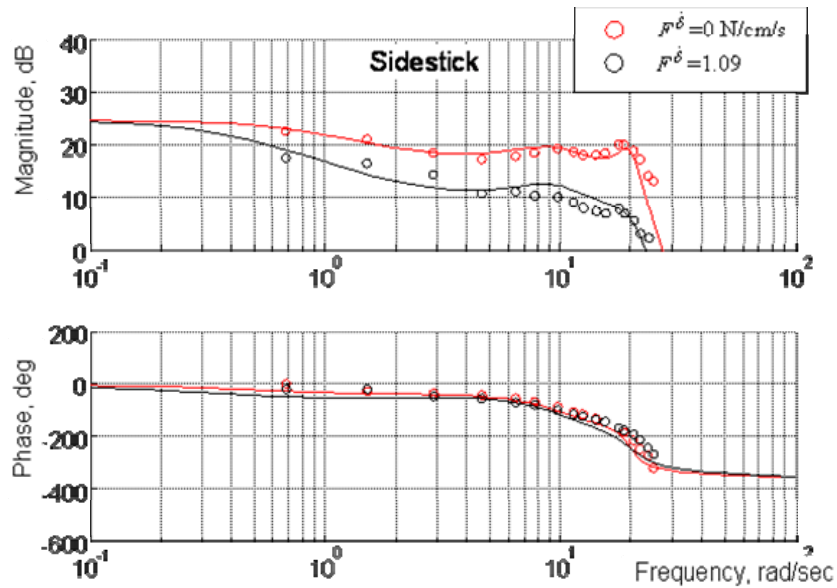


Figure 3.18. Biodynamical pilot. Comparison of the experimental describing function with that calculated in accordance with the transfer functions. Sidestick, effect of damping.

The following notion should be made, important for future study. The parameter adjustment was made for the force gradient equal zero. But in serial aircraft there are no control inceptors with “zero” force gradient. Usually, it is selected close to optimum. Thus, to achieve a result close to practice, we are going (in our next Test Campaign) to conduct additional series of biodynamical experiments to determine the effect of inceptor damping for the optimum value of force gradient; the adjustment of the parameters for this set of feel system characteristics will be presented in the next ARISTOTEL Deliverables.

4. Pilot Modelling by Multi-Body and Finite-Element Approach

The study of biodynamic feedthrough in relation with fixed-wing aircraft dates back to the late 1960s; in [8, 9] a detailed and accurate study of the neuromuscular implications in the pilot-vehicle interaction was presented. In [10] a sophisticated although linear model of the torso and of the hand was used to analyze feedthrough of a semisupine pilot, in view of the design of advanced man-machine interfaces for high-performance aircraft (a sidestick with elbow rest support). In [11,12] the problem of aircraft roll ratcheting, an “unwanted and inadvertent high frequency oscillation in the roll axis encountered in high performance fighter aircraft during rapid roll maneuvers,” was analyzed using a model of the hip, the torso and the arm of the pilot, connected by linear springs and dampers, whose characteristics were obtained by fitting the experimental frequency response of actual pilots. These, as well as other models proposed in the literature, are essentially linear, with equivalent stiffness and damping properties obtained by fitting experimental data. In [11] it is reported that good correlation with experimental data could only be obtained using an unrealistic value for the mass of the arm.

Biodynamic feedthrough experiments related to the collective control lever have been conducted in [7,14,15]. They highlighted significant variability associated to the size of the human subject (Mayo, in [7], divides the subjects in ‘ectomorphic’ and ‘mesomorphic’), and to posture (in [7] a generic dependence of BDFT magnitude on control inceptor reference position was proposed; in [PM9], the characteristic poles of the BDFT transfer function varied significantly in frequency and damping with the reference position of the control).

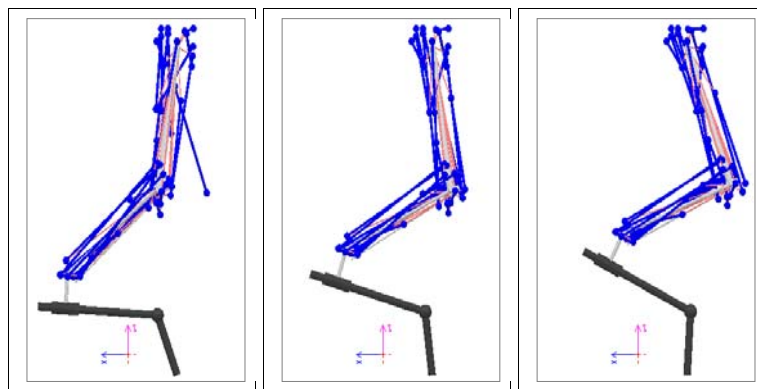


Figure 4.1: multibody model of the pilot's left arm at 10%, 50% and 90% collective

Detailed multibody models of the pilot's arms (Fig. 4.1) have been used to estimate the muscular activation and to produce biodynamic feedthrough functions from first-principles biomechanical models [16,18]. Functions have been estimated for a broad set of parameters, including the geometry and layout of the cockpit, the reference position of the control inceptors and an approximation of “grip tightening” obtained by acting on the quasi-steady approximation of the reflexive muscular activation in order to mimic the task dependence of biodynamic feedthrough discussed in [13].

The rather “deterministic” approach followed in this work must not be intended as a direct means to estimate the feedthrough of a specific individual performing a specific task, but rather as means to determine an envelope of functions that is used to find the limits of possible feedthrough functions. The detailed multibody model has also been directly

incorporated in the aeroelastic multibody model of the helicopter used to study aeroelastic RPCs.

4.1. Multibody Formulation

A general approach is needed to determine the muscular activation required to perform the specific tasks associated to piloting helicopters. The latter include moving control inceptors of arbitrary layout, subjected to various types of restraint actions, including friction and mechanical or emulated force feedback, respectively specific of conventional collective and cyclic pitch control inceptors (Fig. 4.2).

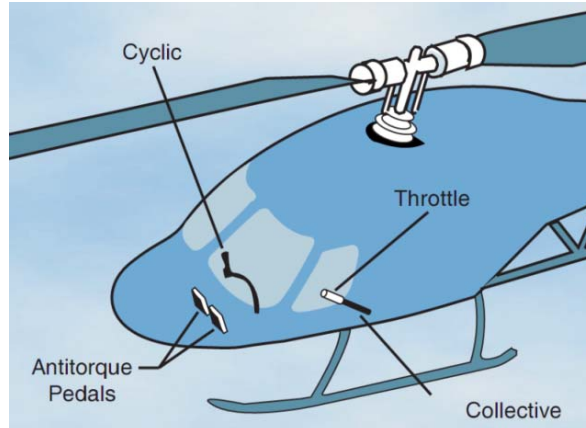


Figure 4.2. Helicopter control inceptors (adapted from [63])

This work mainly focuses on the modeling of the pilot's left arm, involved in the actuation of a conventional collective control inceptor. A multibody model of the arm is developed. This model is used to perform a cascaded analysis consisting in:

1. an inverse kinematics analysis, to determine the configuration of the arm for tasks prescribed to the hand;
2. an inverse dynamics analysis, to determine the joint torques required to perform those tasks;
3. an optimization, to determine the activation pattern required to produce the required torques for each configuration;
4. a singular value decomposition to determine activation modes that, in the given configuration, do not alter the joint torques produced by the muscles (Torque-Less Activation Modes, TLAM);
5. a steady-state linearization of the problem to compute the equivalent impedance properties of the system.

The last point is performed not only considering the optimal activation pattern, to obtain a reference impedance value, but also after adding TLAM patterns, to estimate the variability of the impedance caused by non-optimal muscular activation.

The first two steps of the procedure have been implemented using the general-purpose multibody solver MBDyn (<http://www.mbdyn.org/>), a tool developed and freely distributed by POLIMI, while the remaining ones have been dealt with by developing a dedicated solver using Matlab.

4.2. Multibody Model

A multibody model of the left arm has been implemented (Figure 4.3). The model consists of rigid bodies connected by ideal kinematic constraints, under the assumption that the compliance of the limbs and of the articulations can be neglected at this stage, since relatively low loads and slow motions are considered. To limit the complexity of the model,

the arm is grounded at the shoulder, although the need to consider the compliance of the torso will be assessed in future work. The humerus, the radius, the ulna and the hand are modeled as rigid bodies, which account for $6 - 4 = 24$ degrees of freedom. The hand has not been detailed since the focus of the work is on tasks that require to firmly grasp an inceptor. The properties of the bodies for a person of 70 kg body mass and 170 cm height, computed according to data and regression analyses from [20,21], are reported in Table 4.1.

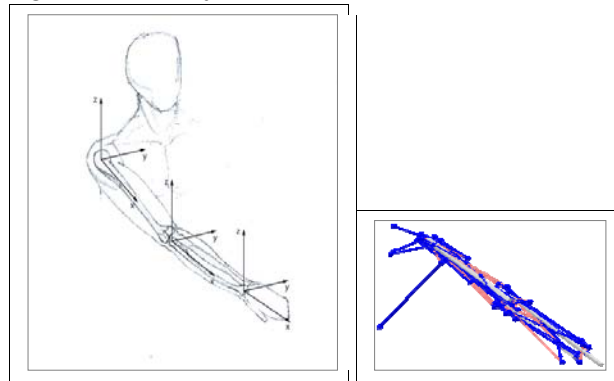


Figure 4.3: Multibody model of the arm.

Body mass	70 kg				
Height	170 cm				
	length	mass	Jxx	Jyy	Jzz
	mm	kg	kg·mm ²	kg·mm ²	kg·mm ²
Humerus	297	2.02	2555.2	14411.2	16228.9
Radius	261	0.61	388.2	2662.0	2717.0
Ulna	261	0.59	582.2	3994.0	4076.0
Hand	68	0.43	195.4	724.0	724.0

Table 4.1: Geometry and inertia properties of the arm's bodies.

The articulation of the shoulder complex is modeled as a spherical hinge that prescribes the coincidence of the center of the proximal condyle of the humerus and the center of the glenoidal fossa, removing 3 degrees of freedom. A revolute hinge approximates the humeroulnar joint, allowing the ulna to rotate with respect to the humerus about its y-axis, centered in the trochlea, removing 5 degrees of freedom. The humeroradial joint is approximated by a spherical joint that prescribes the center of the capitulum to be in a point slightly outside the physical proximal end of the radius, thus removing 3 degrees of freedom. The proximal and distal radioulnar joints are approximated by a single inline joint between a point P and the mechanical x-axis of the ulna. The point P is offset from the radius axis in the local y direction in such a way that the two bones are parallel in rest position, i.e. the configuration in which the arm is full extended, pointing anteriorly, with the palm facing upward. The inline joint removes 2 degrees of freedom. A universal hinge models the carpal complex, thus allowing the flexion and the radio-ulnar deviation of the wrist, removing 4 more degrees of freedom. As a consequence, the resulting model has 7 degrees of freedom and thus would be underdetermined even in case all 6 degrees of freedom of the hand are prescribed.

Inverse kinematics and inverse dynamics are described in detail in [16,18]; they are not reported here for the sake of conciseness as they are not essential for the understanding of

the results of the present analysis. At the end of these phases, the motion of the limbs is estimated in such a manner that the limbs follow the path prescribed to the control inceptors, and the torques needed for each joint to perform those trajectories are estimated.

At such point, the muscular activation level of each muscle must be estimated in such a manner that the muscles yield the required torque by satisfying the 'total activation' paradigm.

Table 4.2: arm muscles' properties: reference length, l_0 ; max isometric force, f_0 ; coordinates of insertion points 1 & 2.

	l_0	f_0	x_1	y_1	z_1	x_2	y_2	z_2
Muscles connecting humerus to the rest of the body								
1 Coracobrachialis	197	242.5	20	30	35	174	21	0
2 Deltoid — anterior fascicles	179	1142.6	35	25	35	136	-12	10
3 Deltoid — middle fascicles	159	1142.6	35	-22	20	136	-24	18
4 Deltoid — posterior fascicles	148	259.9	-35	10	0	136	-24	18
5 Latissimus dorsi	380	1059.2	-65	110	-290	75	25	9
6 Pectoralis major	147	1270.3	45	110	10	36	0	25
7 Supraspinatus	108	487.8	-36	80	35	-32	2	-13
8 Infraspinatus	111	1210.8	-32	80	-40	-26	0	-20
Muscles connecting radius to the rest of the body								
9 Biceps brachii caput longus	388	624.3	0	-15	10	34	16	0
10 Biceps brachii caput brevis	324	435.6	20	30	25	3	16	0
Muscles connecting ulna to the rest of the body								
11 Triceps brachii caput longus	290	798.5	-35	20	-20	-15	0	-22
Muscles connecting humerus to ulna								
12 Anconeus	55	350.0	300	-5	-12	-14	7	-11
13 Triceps brachii caput laterale/mediale	211	1248.6	112	0	-28	-27	0	-6
14 Brachialis	140	987.3	196	-8	16	17	15	5
Muscles connecting humerus to radius								
15 Brachioradialis	306	261.3	246	-7	0	238	-18	13
16 Pronator teres	148	566.2	270	33	-7	55	-18	12
Muscles connecting humerus to hand								
17 Flexor carpi ulnaris	317	128.9	265	27	-5	5	30	23
18 Extensor carpi ulnaris	290	93.2	269	-27	-5	5	30	-18
19 Extensor digitorum	387	100.7	269	-20	-20	8	0	-16
20 Flexor digitorum superficialis	380	226.6	275	27	-10	7	18	26
21 Flexor carpi radialis	307	74.0	275	27	-7	3	-20	32
22 Extensor carpi radialis	305	405.4	245	-20	0	5	-23	-11
Muscles connecting ulna to radius								
23 Pronator quadratus	33	75.5	200	7	14	236	27	23
24 Supinator	61	476.0	13	17	-8	28	13	-24
Muscle connecting ulna to hand								
25 Abductor pollicis longus	202	59.5	115	-21	-5	3	-18	23

The force exerted by muscles is essentially tensile and depends on muscle length, elongation rate and activation level. The simplification of Hill's muscle force model proposed in [22] has been used in this work. Approximate forms of the dependence of the force on the muscle peak isometric force, elongation and elongation rate are developed as functions of three parameters: the peak isometric force, the reference length, and the reference velocity. Additionally, in most applications a fixed value of reference velocity can be used, or an appropriate value can be estimated as a function of the reference length. The tensile force exerted by the muscle is expressed as $f_m = f_0(f_1(x)f_2(v)a + f_3(x))$ as a function of the non-dimensional elongation, x , the non-dimensional elongation rate, v , and the activation level, a , which is subjected to the constraint $0 \leq a \leq 1$. Non-dimensional contributions to the muscle force are showed in Figure 4.4.

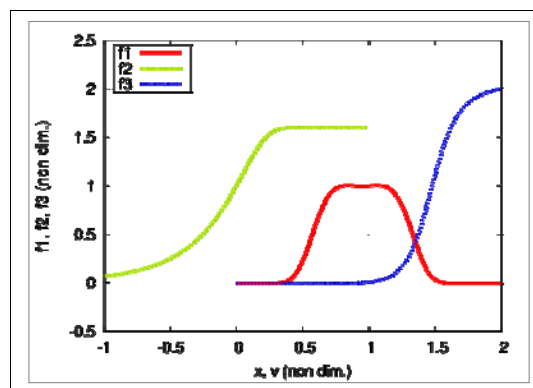


Figure 4.4. Non-dimensional contributions to simplified Hill's model proposed in [22].

The muscles considered in the model are listed in Table 4.2 along with their essential properties: the reference length and peak isometric force from [23], the pennation angle (the angle between the muscle's fibres and the tendon, essentially disregarded in the present model), from [23,24,25], and the locations of the connection points, adapted from [22] and various sources herein.

Muscular activation that provides the desired joint torque is computed by minimizing a functional consisting of the Norm-2 of the activation, subjected to the (linear) constraint that equates the joint torques generated by the muscles to the torques required by the prescribed motion, and to the inequalities $0 \leq a \leq 1$ for all muscles.

4.3. Application: Vertical Maneuver

This section presents relevant results obtained in the analysis of the actuation of the collective control inceptor of a helicopter. The 'Aeronautical Design Standard — Performance Specification for Handling Qualities Requirements for Military Rotorcraft' (ADS-33, [26]) defines a vertical maneuver consisting in transitioning from hover in ground proximity to hover 25 ft above, and quickly returning to the initial position. The maneuver resembles the unmask/remask of scout/attack helicopters.

A similar maneuver, with focus placed on unmasking by transitioning 75 ft (22.86 m) along the heave axis, was simulated during the experimental campaign performed at the University of Liverpool in July 2011 to investigate pilot-in-the-loop aeroelastic rotorcraft-pilot couplings [27]. The control inceptor configuration is mutated from the HELIFLIGHT flight simulator pod (see [15,28]), which is sketched in Figure 4.5 along with the multibody model of the pilot's left arm holding the collective control inceptor.

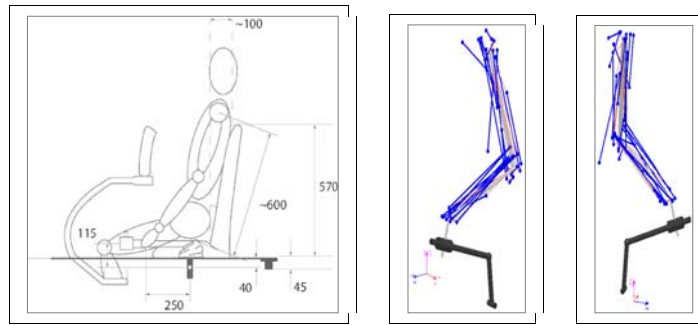


Figure 4.5. Sketch of the multibody model of the pilot's left arm holding the collective control inceptor (approximate measures are in mm).

Figure 4.6 contains a sketch of the experimental setup and the plot of the vertical displacement of the helicopter as a consequence of the rotation of the collective control inceptor. At $t = 18$ s the collective lever is moved downwards; as a consequence, a gentle descent starts. At $t = 25$ s the collective lever is suddenly moved upwards to stop the descent, and a compensatory maneuver occurs until $t = 30$ s in order to achieve an altitude of about 0 m, as requested by ADS-33. The measures reported in Figure 4.6 and used throughout this work were collected during the tests presented in [27].

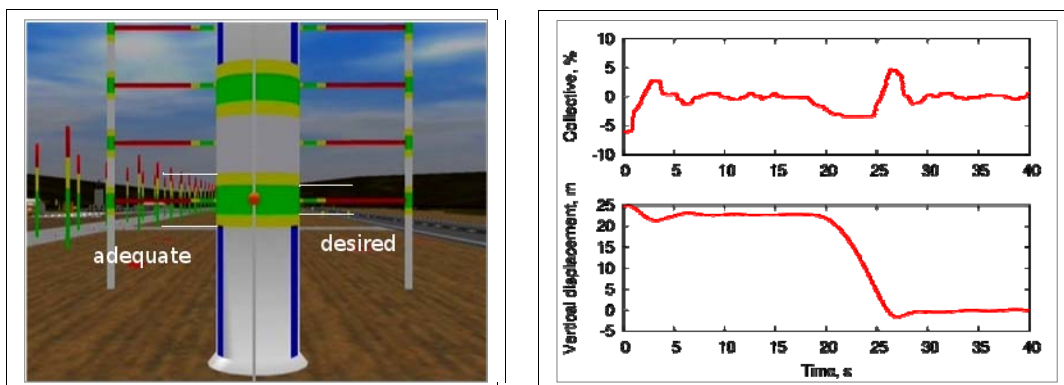


Figure 4.6. Helicopter vertical maneuver; left: flight simulator visual setup; right: Collective control rotation and helicopter vertical displacement.

The joint torques estimated for the maneuver of Figure 4.6 are shown in Figure 4.7, while some of the related muscular activations are shown in Figure 4.8. A steady torque level is required in most joints for the duration of the analysis to carry the arm's own weight. Some of the torques, essentially those associated to shoulder and elbow, change slightly during the push-down and subsequent pull-up of the collective control inceptor. The activations change accordingly and remain relatively limited, i.e. well below 1, as one would expect.

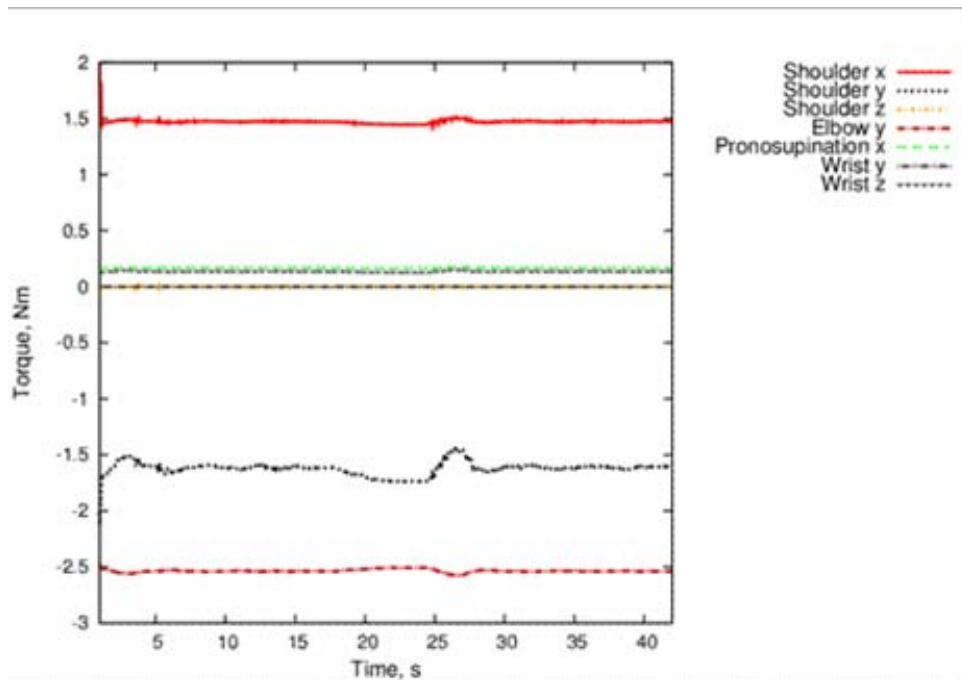


Figure 4.7. Helicopter vertical maneuver: joint torques.

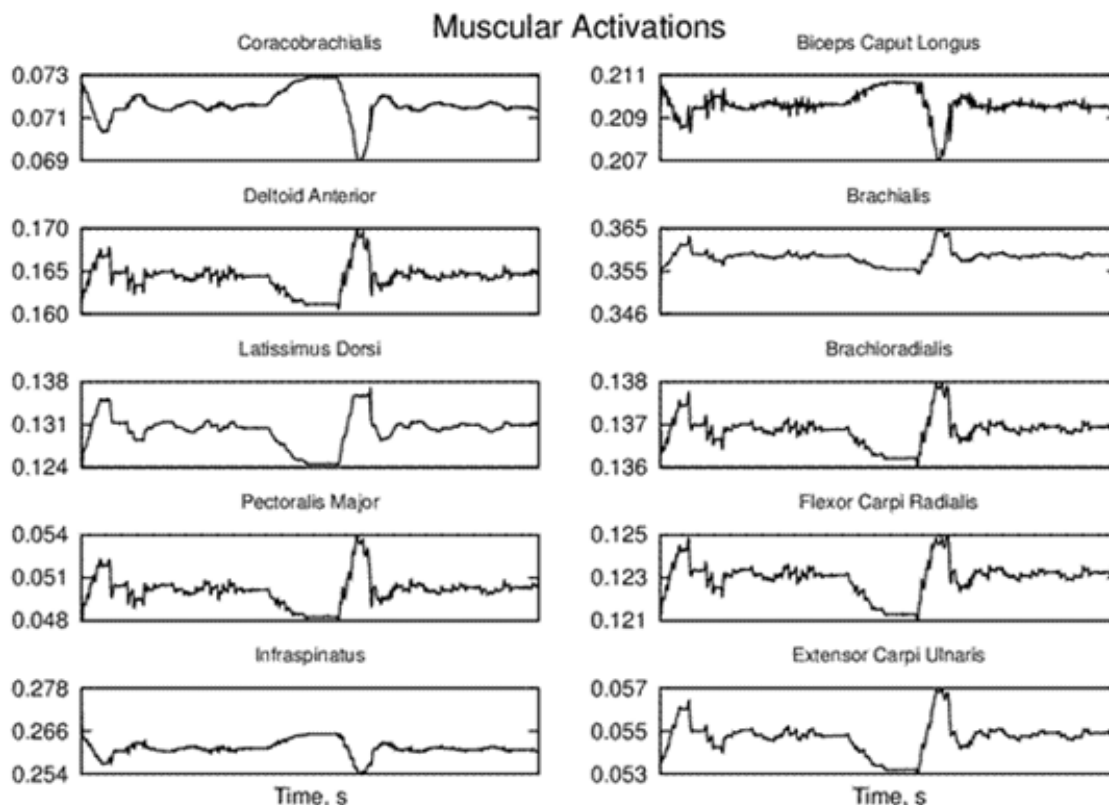


Figure 4.8. Helicopter vertical maneuver: muscular activation of selected muscles.

4.4. Equivalent Feedthrough

Rather simple empirical models of the biodynamic feedthrough related to collective control actuation caused by the vertical acceleration of the seat have been obtained by fitting experimental data [7,15,29]. These models are characterized by a pair of complex conjugated poles, or are at least dominated by such a pair of poles in the frequency band of interest. For example, the models proposed by Mayo [7] present two complex conjugated poles at about 3.5 Hz and about 30% of the critical damping.

Relevant equivalent feedthrough properties of the pilot, namely the frequency and damping of the dominant poles, can be estimated by performing a consistent reduction of equivalent stiffness, damping (provided by the muscles) and inertia (provided by the limbs) for a perturbation of the position of the control inceptor about a reference configuration. Details on the analytical formulas are reported in [16,18].

It is worth stressing that when the perturbation of the muscles' forces is considered at fixed activation level a , the so-called 'intrinsic' stiffness is obtained [30]. In fact, according to Stroeve this value is very small compared to the actual stiffness that may be obtained when the effect of the reflexive system is considered as well, resulting in a total stiffness that can be from 10 to 20 times larger, depending on the reference activation level [30]. To approximately account for this effect, the perturbation of the muscular forces can be expressed as

$$\delta f_m = f_{m/l} \delta l + f_{m/i} \delta i + f_{m/a} \delta a,$$

where the perturbation of activation δa , as a very preliminary approximation, is associated to the reflexive system by means of a simple proportionality relationship

$$\delta a = K_p \delta x + K_d \delta v$$

where K_p and K_d can be interpreted as proportional and derivative gains that essentially express how the activation changes as a consequence of a position or velocity 'error' in the form of a quasi-steady approximation.

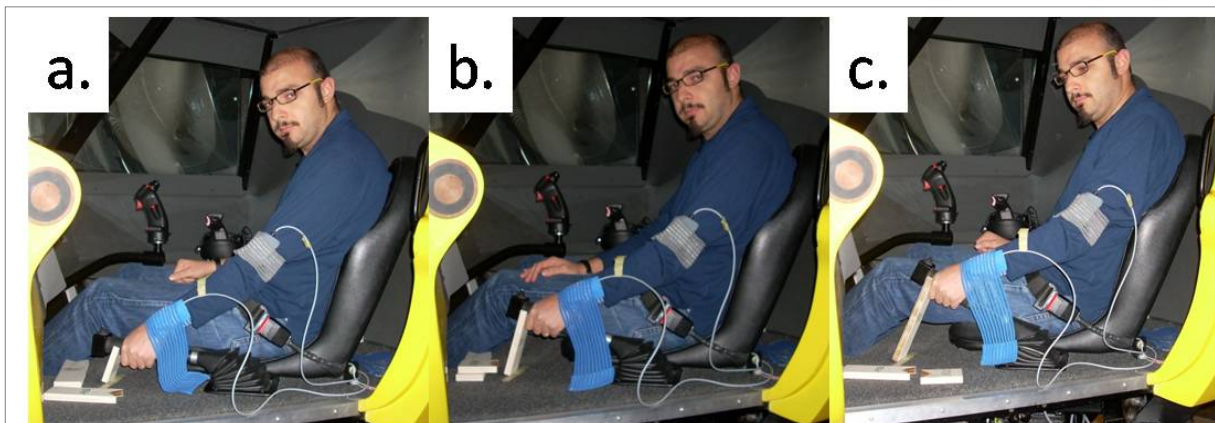


Figure 4.9: Experimental setup for pilot's left arm biomechanical characterization: 10% (a), 50% (b), and 90% (c) reference position of the collective control inceptor.

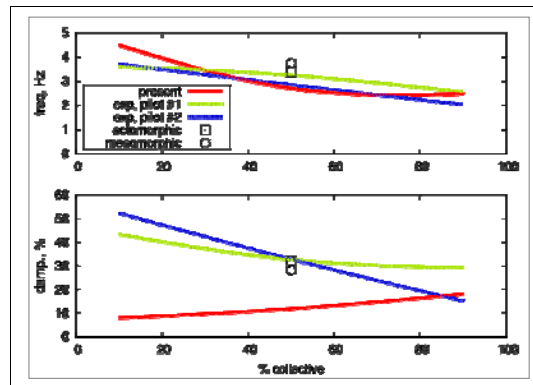


Figure 4.10. Frequency and damping of equivalent dynamic model vs. collective lever position.

Figure 4.9 shows the collective control inceptor of a helicopter flight simulator held at 10%, 50%, and 90% of the allowed amplitude. Figure 4.10 shows the modification of the equivalent stiffness, damping and inertia reduced to the rotation of the collective control inceptor in the above mentioned positions. The gains have been set to $K_p = 0.8$ and $K_d = 0.08$ to match the ratio between the total and the intrinsic stiffness and damping proposed by Stroeve [30]. The resulting frequency and damping are compared with the corresponding values obtained during the test campaign discussed in [15] (indicated as ‘exp, pilot #1’ and ‘exp, pilot #2’ in Figure 4.10), and with data from [7] (indicated as ‘ectomorphic’ and ‘mesomorphic’ in the figure to refer to pilots respectively of small and lean build or large bone structure and muscle build). Dependence of the poles on the rotation of the collective control is not discussed in [7]; for this reason, the corresponding values have been arbitrarily associated with the 50% position in the figure. The results in Figure 4.10 show some common trends; for example, the predicted frequency decreases with the increase of the collective lever position, as confirmed by the experiments. However, the trend on the damping factor is incorrect. In fact the predictions indicate an increase rather than a decrease with the increase of collective lever position.

The order of magnitude of the frequency was matched very well by choosing the gain K_p according to Stroeve’s results [30], although this correction may be considered overly simplified.

The name ‘Torque-Less Activation Modes’ has been coined to indicate perturbations of muscular activation that violate the ‘total activation’ paradigm but do not alter the joint torques. It is conjectured that under specific conditions the muscular activation is not optimal (usually, minimal for a given task) but rather excessive in some unconscious and often unpredictable manner. For example, it is reported that ‘The tendency to couple with structural modes in this fashion appears to increase when pilots tighten their grip on the stick, often in preparation for the flare as the aircraft nears the runway’ [19].

It is worth stressing that the combined optimal and torque-less activations have neither a physical justification or a specific interpretation in motor terms. Within this work, they are mainly intended as means to explore the possible boundaries of the equivalent stiffness and damping provided by the muscles. Moreover, it is understood that the model used in this analysis is only valid for relatively small activation levels; general validity of the model is not sought since it is unlikely that a real pilot uses significantly high activation levels during regular piloting tasks. For this reason, in practical analyses the maximum activation value has been kept well below the upper limit of 1.

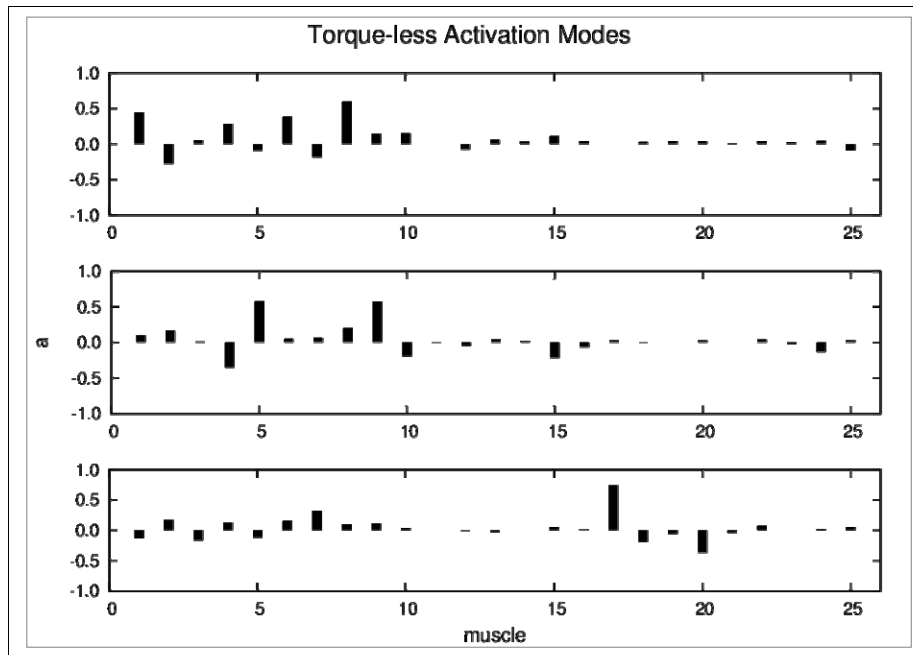


Figure 4.11. Three Torque-Less Activation Modes (TLAMs) computed at $t = 27.5$ s of the transient maneuver discussed earlier

Figure 4.11 shows the activations associated to three TLAMs computed in the configuration at time $t = 27.5$ s of the previously discussed vertical maneuver. It clearly shows that some muscles have a significant participation to TLAMs, while others are essentially unaffected. Moreover, the participation of some muscles implies a negative change of activation.

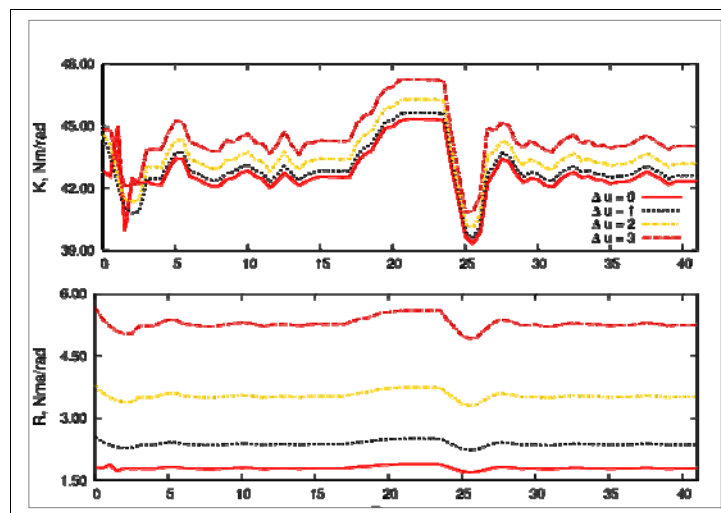


Figure 4.12. Equivalent stiffness and damping obtained for different levels of torque-less activation added to the minimal value ('k' indicates different levels of D_u).

Figure 4.12 shows the change in equivalent stiffness and damping of the pilot resulting from the addition of arbitrary activation levels computed according to the TLAM function of Eq. (39), for increasing value of TLAMs. A change in stiffness up to 10% can be observed, along with a change in damping up to 300%, clearly showing how TLAMs can alter the impedance of the pilot and thus impact the coupled behavior of the system. The values presented in Figure 4.12 consider the total stiffness and damping of the muscle.

4.5. Direct Simulation

The multibody model of the pilot's arm has been used in direct simulations. The model is assembled in the reference configuration resulting from the inverse kinematics analysis. The muscular activations are set to the reference values resulting from the inverse dynamics analysis, plus perturbation terms corresponding to TLAMs and to activations intended to cause torque perturbations about the joint degrees of freedom of the pilot's arms.

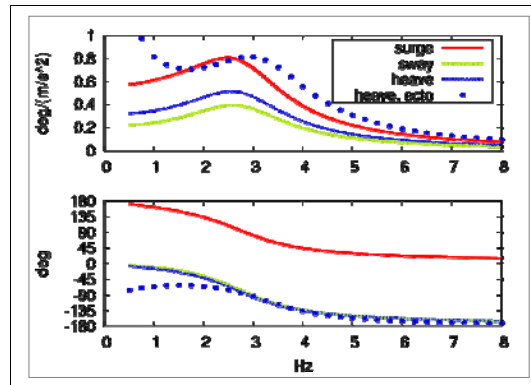


Figure 4.13. Collective control rotation induced by seat accelerations.

The plots in Figure 4.13 illustrate the frequency response of the collective control inceptor when the pilot's seat is excited by accelerations in the surge (longitudinal), sway (lateral) and heave (vertical) directions. The heave plot obtained with the ectomorphic model from [7] is also shown; the non-physical low-frequency behavior should not be considered. The qualitative correlation with the present curve is good; as anticipated, the frequency of the poles resulting from the present analysis is slightly lower; moreover, the amplitude is about half that of [7]. It is interesting to notice that a significant amount of collective control rotation occurs also in response to the surge and sway motions.

This cross-coupling between axes is often neglected in the literature, but it can be at least quantified using the proposed approach.

Three tasks representative of typical pilot activity are considered. They are derived from the experiments performed in [13]. In that experiment, pilots were asked to perform

- ⤴ PT: a position task, consisting in keeping the control inceptor in a prescribed position as accurately as possible, resisting forces;
- ⤴ RT: a relax task, consisting in loosely keeping the control inceptor about a prescribed position;
- ⤴ FT: a force task, consisting in yielding to forces without trying to keep the inceptor in a specific position.

Each task is conjectured to require human operators attain specific neuromuscular settings, consisting in different levels and combinations of muscular activation. The PT is expected to require a significant amount of reflexive activation on top of a minimal reference activation, essentially required to counteract the own weight of the arm. This behavior is produced in the model by using a high level of reflexive proportional gain K_p (the nominal value 0.8 mentioned earlier), on top of the baseline activation computed for each arm configuration. The FT is obtained by setting the reflexive activation gain to zero, while the RT is obtained by setting the reflexive activation gain to an intermediate level ($K_p = 0.2$ was used in the analysis).

Figure 4.14 contains the muscular activation levels for 10%, 50% and 90% collective control reference position.

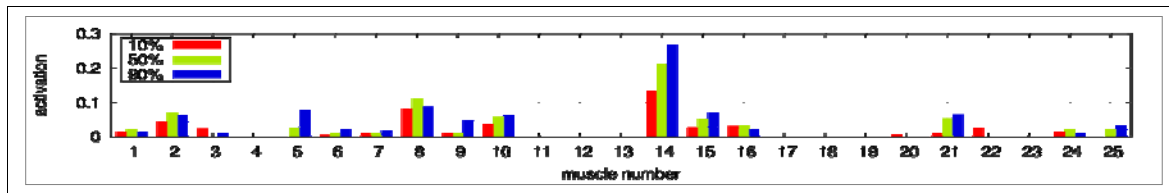


Figure 4.14. Muscular activation levels for 10%, 50% and 90% collective control device reference position.

As an additional source of perturbation, activation levels required to counteract a steady torque applied to the collective control inceptor have been considered, yielding a non-minimal reference activation condition.

4.6. Collective Control Biodynamic Feedthrough

The biodynamic feedthrough has been evaluated by exciting the pilot’s arm model with a prescribed motion of the seat in the surge, sway and heave directions. The bode plots of the BDFT related to the collective control for heave are shown in Figure 4.15. The plots on the left compare the BDFT resulting from the three tasks (PT, RT, FT) at 10%, 50%, and 90% reference collective position. Significant task dependence can be appreciated, in line with that experimentally determined in [13] although for a different layout of the control device. Specifically, higher reflexive gain tasks present the dominant biomechanical poles with a higher frequency. The plots on the right compare the BDFT at 10%, 50%, and 90% reference collective position for each of the three tasks (PT, RT, FT). A clear dependence on the reference control position can be appreciated as well, in line with the discussion in [7] and with the results of the experiments presented in [15], where tasks equivalent to the PT yielded a frequency of the dominant poles that decreased with increasing reference position of the control device.

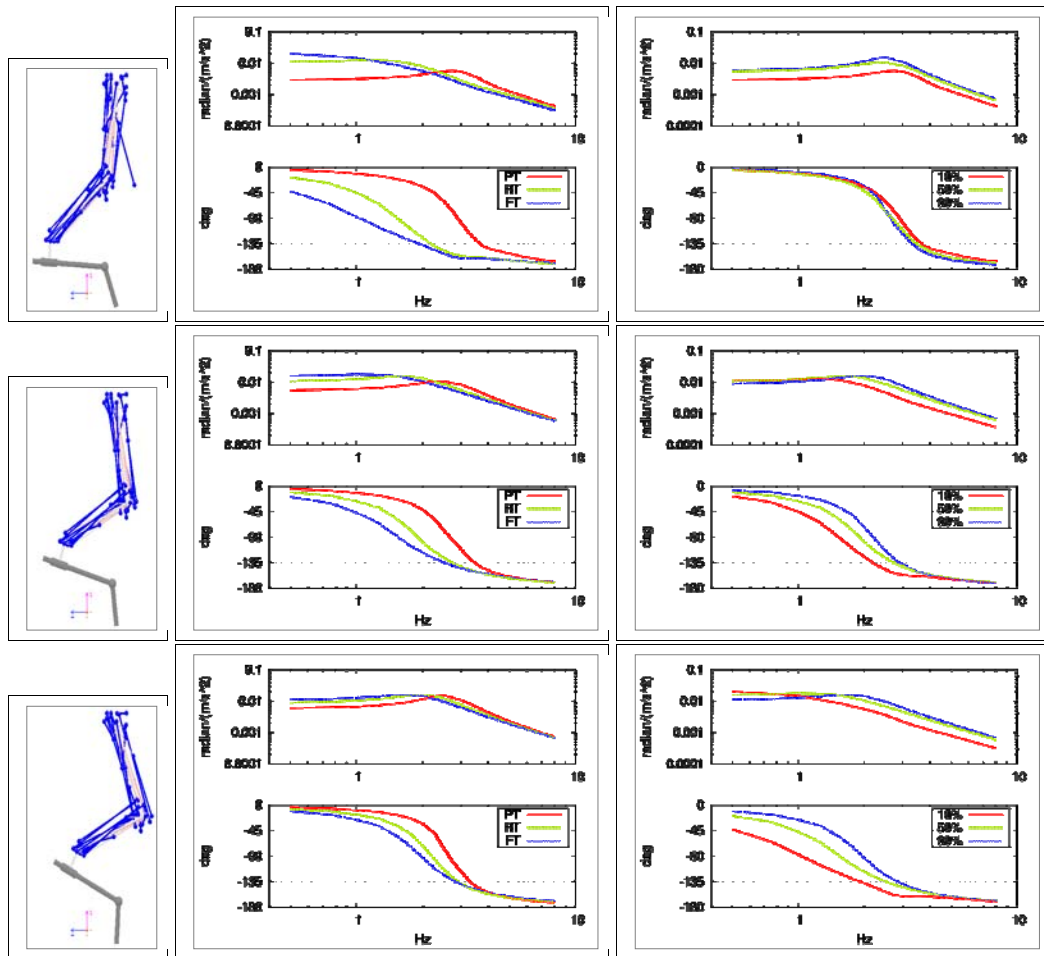


Figure 4.15. collective control biodynamic feedthrough at 10% (top left), 50% (mid left), and 90% (bottom left) reference collective control for position task (PT), relax task (RT), and force task (FT), and for PT (top right), RT (mid right), and FT (bottom right) at 10%, 50%, and 90% reference collective control

4.7. Collective Control Neuromuscular Admittance

The neuromuscular admittance associated with the collective control inceptor has been evaluated by prescribing the rotation of the collective control to excite the pilot's arm, and by analyzing the corresponding constraint reaction. The bode plots of the neuromuscular admittance related to the collective control for heave are shown in Figure 4.16. The plots on the left compare the neuromuscular admittance resulting from the three tasks (PT, RT, FT) at 10%, 50%, and 90% reference collective position. As already noted for the BDFT, significant task dependence can be appreciated, in line with that experimentally determined in [13]. Specifically, higher reflexive gain tasks present the dominant biomechanical poles with a higher frequency. The plots on the right compare the neuromuscular admittance at 10%, 50%, and 90% reference collective position for each of the three tasks (PT, RT, FT). A clear dependence on the reference control position can be appreciated as well.

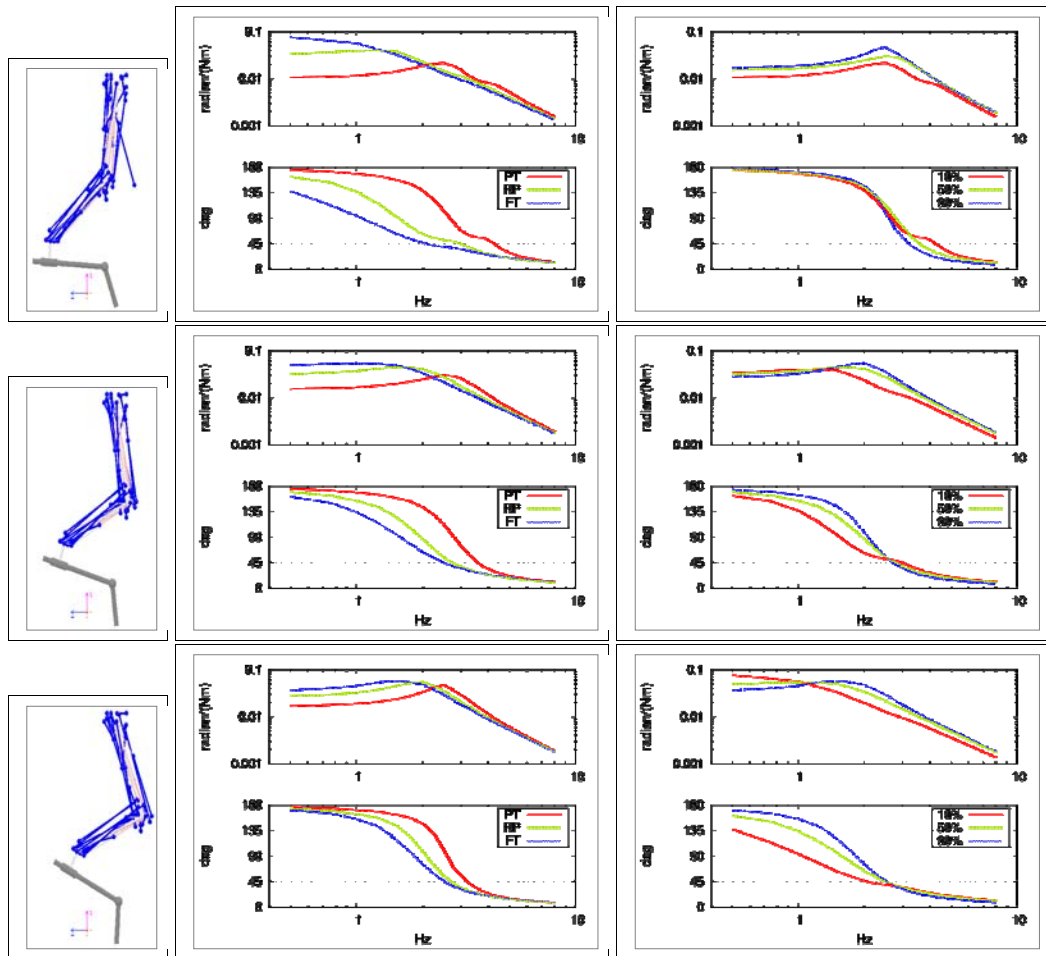


Figure 4.16. collective control neuromuscular admittance at 10% (top left), 50% (mid left), and 90% (bottom left) reference collective control for position task (PT), relax task (RT), and force task (FT), and for PT (top right), RT (mid right), and FT (bottom right) at 10%, 50%, and 90% reference collective control.

4.8. BDFT and Neuromuscular Admittance Under Load

The BDFT and the neuromuscular admittance of the pilot while requested to counteract a steady 100 N·m torque applied to the collective control are shown in Figure 4.17. The need to counteract the load causes additional muscular activation, which increases the equivalent stiffness of the muscles. As a consequence, BDFT and neuromuscular admittance are generally lower than in the reference condition, while the poles shift toward higher frequencies.

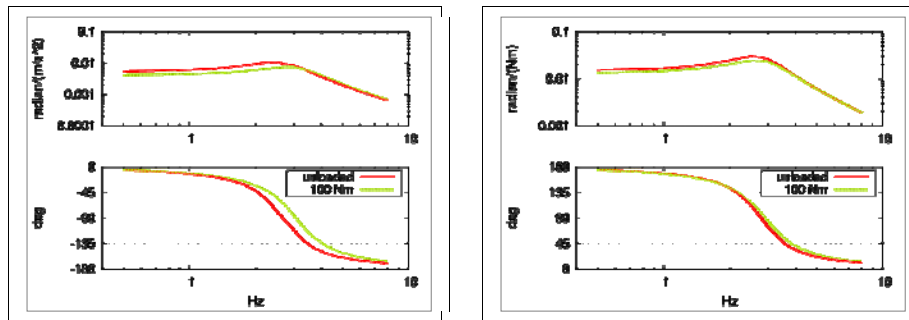


Figure 4.17. collective control BDFT (left) and NA (right) between an unloaded inceptor and one loaded with a steady 100 N-m torque (position task, 50% reference collective rotation).

4.9. Use of Neuromuscular Admittance and BDFT

The availability of the results presented in the previous sections is very important for practical applications. The Bode plots of the BDFT can be directly used to evaluate the robustness of the stability and of the performances of pilot-in-loop vehicle models, even in graphical form, as proposed in [27, 31]. Figure 4.18 present the envelope of BDFT and neuromuscular admittance.

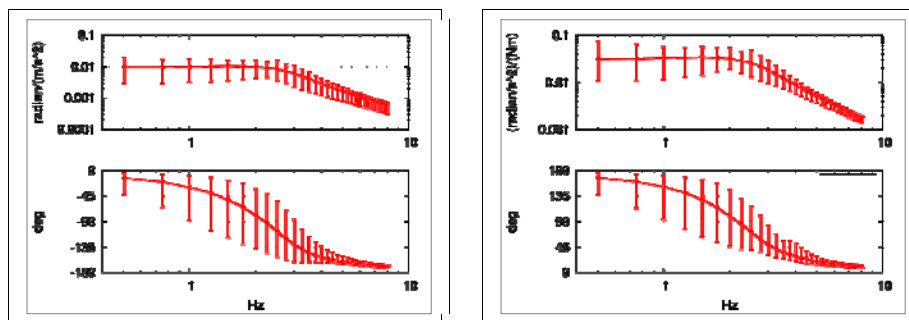


Figure 4.18. Envelope of collective control BDFT and NA.

Transfer functions can be identified from the numerical BDFT and neuromuscular admittance data, to be used in linear/linearized analysis [32,33]. Transfer functions identified from BDFT can be directly used in aeroservoelastic simulations by closing the vehicle control loop. Alternatively, the nonlinear multibody model of the pilot can be integrated in the aeroservoelastic analysis of the vehicle. In fact, the biomechanical model of the pilot's arm has also been incorporated in the detailed multibody rotorcraft models implemented within the project. This was made possible by the fact that the very same multibody dynamics solver, MBDyn, is used for both analyses, thanks to its versatility. The coupled analyses are outside the scope of this document. They are mentioned here because the viability of the coupled analysis was checked as part of the multibody pilot modeling effort.

Time and resources permitting, future activity will address the addition of models of the torso to improve the fidelity of the model in the bandwidth of interest and the capability to address feedthrough and admittance functions that involve the whole body, or at least of its upper part, to further refine and extend the outcome of this task.

5. Results and Conclusion

1. Several BDFT transfer functions for rotorcraft cockpit layout have been identified, both for the collective lever connection and the cyclic stick. A significant intersubject and intrasubject variability in the transfer function has been found. As a consequence amplitude and phase intervals for the BDFT at each frequency have been computed. These intervals may be used to analyse the RPC stability using a robust stability approach [31]. All transfer functions identified have been distributed and are collected to this deliverable.
2. The open-loop vehicle dynamics have been analysed considering the POLIMI complete aero-servo-elastic model and low order model with 42 states in hover and 80 kts flight conditions.
3. The transfer function between the collective, longitudinal cyclic pitch and lateral cyclic pitch controls and longitudinal and lateral attitude, vertical and lateral displacements have been considered in order to evaluate rotorcraft dynamic behaviour in the active pilot bandwidth. The band width phase delay criterion has been used to appreciate influence of effective delay on full ASE model.
4. The structural pilot model is suitable to estimate the pilot work measure and HQSF parameter. These are consistent with the bandwidth phase delay criteria and will be required in estimation of handling qualities level.
5. The validated idea of splitting the pilot activity into “active pilot” visually controlling the aircraft and “biodynamical pilot” describing involuntary inceptor displacements under high-frequency lateral accelerations, allowed thorough analysis of the experimental describing functions received in the course of biodynamical experiments. The analysis, in particular, showed that feel system characteristics do not affect active pilot model, but their deviation from the “optimum” values can cause handling qualities ratings deterioration. On the contrary, for biodynamic interaction the effect of feel system characteristics is evident. Biodynamical interaction (biodynamical pilot model) depends on inceptor type: the smallest BDI is observed for the wheel. Inceptor damping is the most effective method to suppress biodynamical interaction, since it considerably reduces the high-frequency inceptor oscillations, and, in the same time, does not cause pilot ratings deterioration in a wide range of its variation.
7. Transfer function identification is made for active and biodynamical pilot models. For the biodynamical pilot model, the rules of parameter adjustment are determined as a function of force gradient and damping.
8. The conducted analysis and the identified transfer functions will be used to develop criteria to assess the effect of aircraft structural elasticity with regard to inceptor feel system characteristics.
9. A detailed multibody model of a helicopter pilot's arm has been developed. The model can be either used to perform “virtual” experiments, to estimate frequency response functions of biodynamic feedthrough and neuromuscular admittance, or directly connected to detailed aeroservoelastic models of the vehicle, for direct integration in time. The main use of this model is dedicated to exploring the sensitivity of biodynamic feedthrough and neuromuscular admittance to various parameters that cannot be proficiently changed in experiments, especially in flight simulators. Possible envelopes of those functions can thus be determined to extract realistic boundaries that can be used, for example, in robust stability analysis.

6. Deviations

No deviations from the initial program occurred. On the contrary, the success in the development of the multibody model of the pilot overcame expectations in many aspects.

7. References

- [1] ARISTOTEL Deliverable No.D2.3 “State-of-the-art pilot model for RPC prediction report”, April 2011.
- [2] ARISTOTEL Deliverable No.D3.5. “Industrial Requirements for Pilot Models with Respect to Aero-servo-elastic A/RPC”, October 2012.
- [3] ARISTOTEL Deliverable No.D3.7 “Industrial Requirements for Vehicle-Pilot Coupling with Respect Aero-servo-elastic A/RPC”, May 2012.
- [4] ARISTOTEL 266073 Deliverable No. D4.1. Preliminary bio-dynamical test plan/matrix, March 2011
- [5] Lin, Yu-Kweng, and Guo-Qiang Cai. Probabilistic structural dynamics: advanced theory and applications. New York: McGraw-Hill, 1995.
- [6] Blackman, R. B., Tukey, J. W., Tukey, J. W., & Tukey, J. W. (1959). The measurement of power spectra: from the point of view of communications engineering (Vol. 1058). New York: Dover Publications.
- [7] John R. Mayo. The involuntary participation of a human pilot in a helicopter collective control loop. In 15th European Rotorcraft Forum, pages 81.1-12, Amsterdam, The Netherlands, 12-15 September 1989.
- [8] Raymond E. Magdaleno, Duane T. McRuer, and George P. Moore. Small perturbation dynamics of the neuromuscular system in tracking tasks. NASA CR-1212, 1968. TR-154-1.
- [9] Raymond E. Magdaleno and Duane T. McRuer. Experimental validation and analytical elaboration for models of the pilot’s neuromuscular subsystem in tracking tasks. NASA CR-1757, 1971.
- [10] Henry R. Jex and Raymond E. Magdaleno. Biomechanical models for vibration feedthrough to hands and head for a semisupine pilot. *Aviation, Space, and Environmental Medicine*, 49(1-2):304-316, 1978.
- [11] Gordon Höhne. A biomechanical pilot model for prediction of roll ratcheting. In AIAA Atmospheric Flight Mechanics Conference, Portland, OR, USA, August 9–11 1999. AIAA-1999-4092.
- [12] Höhne, G., Roll ratcheting - Cause and analysis, *Deutsches Zentrum fuer Luft und Raumfahrt. Forschungsberichte*. (2001)
- [13] J. Venrooij, D. A. Abbink, M. Mulder, M. M. van Paassen, and M. Mulder. Biodynamic feedthrough is task dependent. In 2010 IEEE International Conference on Systems Man and Cybernetics (SMC), pages 2571-2578, Istanbul, Turkey, October 10–13 2010. doi:10.1109/ICSMC.2010.5641915.
- [14] M. Jump, S. Hodge, B. DangVu, P. Masarati, G. Quaranta, M. Mataboni, M. D. Pavel, and O. Dieterich. Adverse rotorcraft-pilot coupling: Test campaign development at the university of Liverpool. In 34th European Rotorcraft Forum, Liverpool, UK, September 16–19 2008.
- [15] Pierangelo Masarati, Giuseppe Quaranta, and Michael Jump. Experimental and numerical helicopter pilot characterization for aeroelastic rotorcraft-pilot couplings analysis. *Proc. IMechE, Part G: J. Aerospace Engineering*, 227(1):124-140, January 2013. doi:10.1177/0954410011427662.
- [16] A. Zanoni, P. Masarati, G. Quaranta, “Rotorcraft Pilot Impedance from Biomechanical Model Based on Inverse Dynamics”, presented at IMECE 2012, Houston, Texas, November 9-15, 2012.

- [17] P. Masarati, G. Quaranta, “Coupled Bioaeroservoelastic Rotorcraft-Pilot Simulation”, submitted.
- [18] P. Masarati, G. Quaranta, A. Zanoni, “Dependence of Helicopter Pilots' Biodynamic Feedthrough on Upper Limbs' Muscular Activation Patterns”, submitted.
- [19] David L. Raney, E. Bruce Jackson, William M. Adams, and Carey S. Buttrill. The impact of structural vibration on flying qualities of a supersonic transport. In AIAA Atmospheric Flight Mechanics Conference, Montreal, Canada, August 6–9 2001. AIAA-2001-4006.
- [20] J. Cheverud, C. C. Gordon, R. A. Walker, C. Jacquish, L. Kohn, A. Moore, and N. Yamashita. 1988 anthropometric survey of US Army personnel: correlation coefficients and regression equations. part 1: Statistical techniques, landmark, and measurement definitions. TR 90/032, NATICK, 1990.
- [21] J. Cheverud, C. C. Gordon, R. A. Walker, C. Jacquish, L. Kohn, A. Moore, and N. Yamashita. 1988 anthropometric survey of US Army personnel: correlation coefficients and regression equations. part 4: Bivariate regression tables. TR 90/035, NATICK, 1990.
- [22] Pennestri, E., Stefanelli, R., Valentini, P. P., and Vita, L., 2007. “Virtual musculo-skeletal model for the biomechanical analysis of the upper limb”. *Journal of Biomechanics*, 40(6), pp. 1350–1361. doi:10.1016/j.jbiomech.2006.05.013.
- [23] K. R. S. Holzbaur, W. M. Murray, and S. L. Delp. A model of the upper extremity for simulating musculoskeletal surgery and analyzing neuromuscular control. *Annals of Biomechanical Engineering*, 33:829–840, 2005.
- [24] M. A. Lemay and P. E. Crago. A dynamic model for simulating movement of the elbow, forearm and wrist. *Journal of Biomechanics*, 29(10):1319–1330, 1996. doi:10.1016/0021-9290(96)00026-7.
- [25] R. L. Lieber and T. J. Burkholder. Musculoskeletal soft tissue mechanics. In Donald R. Peterson and Joseph D. Bronzino, editors, *Biomechanics: Principles and Applications*, pages 2.1–13. CRC Press, 2008.
- [26] Anonymous. Performance specification, handling qualities requirements for military rotorcraft. ADS 33-EPRF, US Army AMCOM, Redstone, Alabama, 2000.
- [27] P. Masarati, G. Quaranta, L. Lu, and M. Jump. Theoretical and experimental investigation of aeroelastic rotorcraft-pilot coupling. In American Helicopter Society 68th Annual Forum, Fort Worth, Texas, May 1–3 2012.
- [28] G. D. Padfield and M. D. White. Flight simulation in academia; HELIFLIGHT in its first year of operation. *The Aeronautical Journal of the Royal Aeronautical Society*, 107(1075):529–538, September 2003.
- [29] J. Venrooij, M. D. Pavel, M. Mulder, F. C. T. van der Helm, and H. H. B'ulthoff. A practical biodynamic feedthrough model for helicopters. In 38th European Rotorcraft Forum, Amsterdam, the Netherlands, September 3–7 2012. Paper no. 096.
- [30] Stroeve, S., 1999. “Impedance characteristics of a neuromusculoskeletal model of the human arm I. posture control”. *Biological Cybernetics*, 81(5–6), pp. 475–494. doi:10.1007/s004220050577.
- [31] Quaranta, G., Tamer, A., Muscarello, V., Masarati, P., Gennaretti, M., Serafini, J., and Colella, M. M., 2012. “Evaluation of rotorcraft aeroelastic stability using robust analysis”. In 38th European Rotorcraft Forum.
- [32] Dieterich, O., Götz, J., DangVu, B., Haverdings, H., Masarati, P., Pavel, M. D., Jump, M., and Gennaretti, M., 2008. “Adverse rotorcraft-pilot coupling: Recent research activities in Europe”. In 34th European Rotorcraft Forum.

- [33] Serafini, J., Gennaretti, M., Masarati, P., Quaranta, G., and Dieterich, O., 2008. "Aeroelastic and biodynamic modeling for stability analysis of rotorcraft-pilot coupling phenomena". In 34th European Rotorcraft Forum.
- [34] GARTEUR HC AG 16, "Rigid Body and Aeroelastic Rotorcraft-Pilot Coupling (RPC) – Prediction Tools and Means for Prevention", Technical Report, TP No.167, October 2008
- [35] Yamauchi, G.K., Young L.A. - A Status of NASA Rotorcraft Research, NASA/TP-2009-215369, Ames Research Center; Moffett Field, California, September 2009
- [36] ARISTOTEL – "Aircraft and Rotorcraft modelling for Aero-servo-elastic A/RPC", Deliverable No. D3.4, March 2012
- [37] R. Celli, - "Numerical calculation of multiloop transfer function with application to pilot-rotor interaction", ERF 30th, Marseilles, September 14-16, 2004
- [38] R. T. N. Chen, W. S. Hindson, - "Influence of High-Order Dynamics on Helicopter Flight Control System Bandwidth", Journal of Guidance, Control, and Dynamics, vol. 9, No. 2, March-April, 1986
- [39] Padfield G.D. – "Helicopter Flight Dynamics", The Theory and Application of Flying Qualities and Simulation Modeling, second edition, Blackwell Publishing, 2007
- [40] D.T. McRuer, E.S. Krendel, - "Mathematical Models of Human Pilot Behavior", AGARD-AG-188, January 1974
- [41] Mc. Ruer, D.T., - "Pilot-Induced Oscillations and Human Dynamic Behavior", NASA Contractor Report 4683, July 1995
- [42] K. B. Zaychick, M. Cardullo, - "Intelligent Systems Approach for Automated Identification of individual Control Behavior of a Human Operator", NASA/CR-2012-217555, March 2012
- [43] Mc Ruer, D.T., et al., - AVIATION SAFETY AND PILOT CONTROL. Understanding and Preventing Unfavorable Pilot – Vehicle Interactions, National Academic Press, Washington, D.C., 1997
- [44] Hess, R.A., R. M. Kalteis, - "Technique for Predicting Longitudinal Pilot-Induced Oscillations", Journal of Guidance, Control, and Dynamics, vol. 14, No. 1, Jan.-Feb., 1991
- [45] K. R. Heffley, - "A Compilation and Analysis of Helicopter Qualities Data", Volume Two: Data Analysis, August 1979, NASA CR 3145
- [46] G.C. Beerens, H.J. Damveld and others, - "Investigation into Crossover Regression in Compensatory Manual Tracking Tasks", Journal of Guidance, Control, and Dynamics, vol. 32, No. 5, Sept.-Oct., 2009
- [47] V. Muscarello, P. Masarati, G. Quaranta, - "Multibody Analysis of Rotorcraft-Pilot Coupling", 2nd International Conference on Multibody System Dynamics, May 29 – June 1, Stuttgart, Germany
- [48] "ADS 33E – PRF Performance Specification – Handling Qualities Requirements for Military Rotorcraft", 1996
- [49] Hess R. A. – "Theory for Aircraft Handling Qualities Based on Upon a Structural Pilot Model", Journal of Guidance and Control, vol.12, No. 6, November-December 1989
- [50] Hess, R.A., - "Unified Theory for Aircraft Handling Qualities and Adverse Aircraft-Pilot Coupling", Journal of Guidance, Control, and Dynamics, vol. 20, No. 6, Nov.-Dec., 1997
- [51] Hess, R.A., Malsbury, T., - "Closed-Loop Assessment of Flight Simulator Fidelity", Journal of Guidance, Control, and Dynamics, vol. 14, No. 1, Jan.-Feb, 1991
- [52] Hess, R.A., Marchesi, F., - "Analytical Assessment of Flight Simulator Fidelity Using Pilot Models", Journal of Guidance, Control, and Dynamics, vol. 32, No. 3, May-June 2009

- [53] Hess, R.A., - "Modeling Pilot Control Behavior with Sudden Changes in Vehicle Dynamics", *Journal of Aircraft*, vol. 46, No. 5, Sept.-Oct., 2009
- [54] M. Perhinschi, J.V.R. Prasad, - "Analytical investigation of helicopter handling qualities criterion using a structural pilot model", August 1995, AIAA-95-3456-CP
- [55] L.E.Zaichik, V.V.Rodchenko, Yu.P.Yashin, et.al. "Acceleration Perception", AIAA MST Conference, AIAA-99-4334, Portland OR, 1999.
- [56] V.V.Rodchenko, L.E.Zaichik, Y.P.Yashin, I.V.Rufov, A.D.White, "Theoretical Approach To Estimation of Aceleration Effects on Piloting", AIAA-2000-4292, AIAA MST Conference, Denver CO, 2000.
- [57] V.V.Rodchenko, L.E.Zaichik, Y.P.Yashin, et.al., "Investigation of Controllability Criteria of Class III Aircraft Equipped with a Sidestick", WL-TR-96-3079, Wright-Patterson Laboratory, Dec.1994.
- [58] ARISTOTEL Deliverable No.4.1 "Preliminary bio-dynamical test plan/matrix", March 2011.
- [59] ARISTOTEL Deliverable No.4.5 "Simulator Test Plan/Matrix of the 1st Test Campaign", May 2012.
- [60] ARISTOTEL Deliverable No.D4.2 "Preliminary bio-dynamical test data analysis and critical review", September 2011.
- [61] L.E.Zaichik, Y.P.Yashin, P.A.Desyatnik, K.N.Grinev, "Effect of Manipulator Type and Feel System Characteristics on High-Frequency Biodynamic Pilot-Aircraft Interaction", Paper 285, ICAS2012, Brisbane, Australia, 2012.
- [62] V.V.Rodchenko, L.E.Zaichik, Y.P.Yashin, "Similarity Criteria for Manipulator Loading and Control Sensitivity Characteristics", *Journal of Guidance, Control and Dynamics*, vol.21, No2, 1998, pp.307-314.
- [63] Anonymous. Rotorcraft Flying Handbook. FAA H-8083-21, Federal Aviation Administration, 2000.

8. List of Abbreviations

ARISTOTEL – Aircraft and Rotorcraft Pilot Couplings – Tools and Techniques for Alleviation and Detection

ASE – Aero-Servo-Elastic model

APM – Active Pilot Model

BDI – Biodynamic Interaction

FCS – Flight Control System

HOST – Helicopter Overall Simulation Tool

HQR – Handling Qualities Requirements

HQSF – Handling Qualities Sensitivity Function

MASST – Modern Aero-servo-elastic State Space Tools

M17 – Low order rigid body model

M42 – Low order ASE model

PAO – Pilot Assisted Oscillations

PF – Pilot Flying

PIO – Pilot Induced Oscillations

PPM – Passive Pilot Model

RB – Rigid Body model

RPC – Rotorcraft Pilot Coupling